Inaugural dissertation

for

obtaining a doctoral degree

of the

Combined Faculty of Mathematics, Engineering and Natural Sciences

of the

Ruprecht-Karls University

Heidelberg

presented by

M.Sc. Dimitri Kasakovski

born in: Bochum

Oral Examination:

17th of June 2024

Endothelial Smad6 and Smad7 harmonize
blood vessel development and tumor progression

Referees: Prof. Dr. Ursula Klingmüller
             Prof. Dr. Hellmut Augustin

Die vorliegende Arbeit wurde in der Abteilung für Vaskuläre Onkologie und Metastasierung am Deutschen Krebsforschungszentrum in Heidelberg, und dem European Center for Angioscience in der Abteilung für Vaskuläre Biologie & Angiogeneseforschung an der Universitätsmedizin in Mannheim durchgeführt

Acknowledgment - Danksagung

Mama und **Papa**, wer hätte euch damals zugetraut, irgendwann hier anzukommen. Ich bin mir sicher, wenn jemand überzeugt davon war, dann Mama. Aus einer alten Welt ausgebrochen, Abschlüsse nicht anerkannt, Deutsch gelernt, neu studiert, mit Putzen und Pizzen ausliefern das Studium finanziert, und das alles mit einem kleinen Kind. Am Ende hat Mama sogar noch promoviert. Ich möchte diese Dissertation deshalb euch beiden widmen. Es ist genauso eure wie meine Leistung. Denn wie hätte ich, der dank euch doch einen viel einfacheren Weg gehabt hat, nicht mein Bestes geben können.

Zuerst möchte ich mich bei allen Technischen Assistenten, Tierpflegern und -ärzten, Wissenschaftlern in den Core-Facilities, Mitarbeitern der Administration und Graduiertenschule bedanken. Ohne eure Arbeit läuft der Laden nicht: **Maria, Carleen, Claudine, Eva, Kerstin, Merle, Mattea, Sandra, Petra, Barbara, Flo, Steffen, Markus, Klaus, Felix, Damir, Manuela, Gaby, Doris, Nadine, Calvin, Sabine, Edi, Lindsay, Heike** und **alle Kollegen**!

Jeder möchte mit gut ausgebildeten Fachkräften zusammenarbeiten, aber die wenigsten wollen die Zeit investieren, diese auch auszubilden. **Kenneth, Lisa, Ioanna** und **Lilli,** ihr habt mir gezeigt wie anstrengend aber auch bereichernd diese Erfahrung sein kann. Ich hoffe, ihr habt etwas aus der Zeit in unserem Labor mitnehmen können.

Rob, ich bin dir für deine Unterstützung und Freundschaft in den letzten zwei Jahren unendlich dankbar. Unseren morgendlichen Kaffee und die interessanten Gespräche im Hotspot vermisse ich jetzt schon. ‚And as the years go by, our friendship will never die. You're gonna see, it's our destiny. You've got a friend in me!'

Cata and **Tim**, same goes for you, without your friendship Odysseus would not have been able to endure this Odyssey.

Amy, ich bin so froh dich während meiner Zeit in Heidelberg kennengelernt zu haben. Egal was die Zukunft bringt, bin ich überzeugt, dass es zusammen mit dir nur gut werden kann. Danke, dass du mich selbst in den schwierigsten Phasen immer unterstützt hast. ผมรักคุณ!

Hellmut: Ich bin dir für die Zeit in deinem Labor wirklich außerordentlich dankbar. Ich habe wissenschaftlich, und auch persönlich, sehr viel von dir gelernt. Ich war nicht immer der einfachste Doktorand, möchte aber, dass du weißt, dass ich den größten Respekt für deine Vision habe. Ich wünsche dir und deiner zukünftigen Crew Erfolg und Durchhaltevermögen. – D.

Acknowledgment

‚Life [as well as the doctoral journey] can only be understood backwards; but it must be lived forwards.'

-Søren Kierkegaard-

Table of Contents

Table of Contents

Table of Contents

Table of Contents

List of Figures

List of Tables

Zusammenfassung

Die gesunde Funktion des organ-spezifischen Blutgefäßsystems so wie die Aufrechterhaltung der Gefäßquieszenz über das Leben, sind Merkmale der Gesundheit und Langlebigkeit. Während der Gefäßentwicklung reagieren Endothelzellen (EZ) auf Stimuli und proliferieren. Sobald die Blutgefäße ausgereift sind, gehen die EZ in einen aktiv aufrechterhaltenen Ruhezustand über, der durch eine verringerte proliferative Aktivität gekennzeichnet ist. EZ-Quieszenz ist ein Zustand, der von komplexen Signalkaskaden aktiv gesteuert wird und unter pathologischen Bedingungen reversibel ist. Welche molekularen Programme für die Erlangung und langfristige Aufrechterhaltung entscheidend sind, ist noch nicht entschlüsselt. Um die Mechanismen zu untersuchen, durch die EZ ihren Ruhezustand erlangen und aktiv aufrechterhalten, führten Schlereth *et al.* genomweite epigenetische und transkriptomische Analysen am kontinuierlichen Lungenendothel in neugeborenen und erwachsenen Mäusen durch. Dabei wurde der TGFβ-Signalweg und dessen Inhibitoren Smad6 und Smad7 am stärksten reguliert. Die TGFβ-Signalfamilie ist für die Entwicklung der Gefäße und des funktionalen Endothels von entscheidender Bedeutung, jedoch ist ihre Rolle bei der Blutgefäßreifung und -homöostase im Erwachsenenalter erst seit kurzem bekannt. Vor allem die einzigartigen kontext-abhängigen Integrationsmechanismen von TGFβ- und BMP- Signalen durch die intrazellulären Inhibitoren Smad6 und Smad7 während der vaskulären Entwicklung, Reifung und Quieszenz sind weniger bekannt. Durch die Gendeletion von endothelialem Smad6 und Smad7 in verschiedenen Entwicklungsstadien bis zur adulten Homöostase konnte ich zeigen, dass die induzierbare endotheliale Deletion (IECKO) von Smad6 während der embryonalen Entwicklung zu umfassenden Blutungen und pränataler Letalität mit mäßiger Penetranz bis E18.5 führte. Die postnatale Deletion des endothelialen Smad6 hatte keinen Einfluss auf retinale Angiogenese, führte aber zu einer verstärkten pathologischen Neovaskularisation während der Sauerstoff-induzierten Retinopathie (OIR). Im Gegensatz dazu waren Smad7IECKO-Mäuse nach embryonaler Deletion lebensfähig, während der postnatale Verlust von endothelialem Smad7 die retinale Angiogenese beeinträchtigte. Die embryonale Deletion von endothelialem Smad6 und Smad7 führte zu pränataler Letalität mit hoher Penetranz bis E13.5, und die postnatale Deletion führte zu einer Beeinträchtigung der retinalen Angiogenese vergleichbar mit den Beobachtungen in Smad7IECKO-Mäusen. Mithilfe von zwei Tumormodellen (LLC und B16F10) in erwachsenen Smad6- und Smad7IECKO-Mäusen konnte ich festellen, dass endotheliales Smad6 und Smad7 die Tumorgröße und das Überleben unterschiedlich beeinflussen. Der Verlust von endothelialem Smad6 führte zu verstärktem Tumorwachstum und einem höheren Überleben während der Metastasierung. Der Verlust von Smad7 im Endothel führte zu einer Verringerung des Tumorwachstums und einem geringeren

Zusammenfassung

Überleben während der Metastasierung. Der Verlust von endothelialem Smad6 und Smad7 hob die Auswirkungen der einzelnen Deletion auf. Insgesamt habe ich somit gezeigt, dass Smad6 und Smad7 die physiologische und pathologische Angiogenese auf unterschiedliche Weise regulieren, aber nur eine marginale oder möglicherweise entbehrliche Rolle in der vaskulären Quieszenz spielen. Vorläufige Daten deuten auch darauf hin, dass Smad6 und Smad7 im Endothel das Wachstum von Primärtumoren und die Verbreitung von Metastasen auf unterschiedliche Weise regulieren.

Summary

Functional maturation of an organotypic blood vessel system and maintenance of vascular quiescence throughout life are features of health and longevity. During vascular development and angiogenesis, endothelial cells (EC) are responsive to stimuli and proliferate but once blood vessels mature, they transition into an actively maintained quiescent state characterized by diminished signaling response and proliferative activity. Moreover, EC quiescence is not a one-way street of cell fate but a transient state and it is still not deciphered what molecular programs are critical for its acquisition and long-term maintenance. To investigate the mechanisms by which EC acquire and actively maintain their quiescent resting state, Schlereth *et al.* performed genome-wide epigenetic and transcriptomic screens of continuous lung EC in newborn and adult mice. Here, TGFβ signaling, and the inhibitors Smad6 and Smad7, were most prominently regulated. The TGFβ superfamily is imperative for facilitating vascular development and endothelial cell fate but its role in maturation and adult homeostasis is only recently emerging. Notably, the unique integration of TGFβ and BMP-mediated signaling by the intracellular inhibitors Smad6 and Smad7 over vascular development, maturation and quiescence is less well established. By deleting endothelial Smad6 and Smad7 at different developmental stages up until adult homeostasis, I show that embryonic deletion in Smad6IECKO mice led to widespread hemorrhages and lethality with moderate penetrance by E18.5. Postnatal deletion of endothelial Smad6 did not affect retinal angiogenesis but led to increased pathological neovascularization during oxygen-induced retinopathy (OIR). In contrast, Smad7IECKO mice after embryonic deletion were viable and postnatal loss of endothelial Smad7 impaired retinal angiogenesis. Combined embryonic deletion of endothelial Smad6 and Smad7 led to lethality with high penetrance before E13.5 and postnatal deletion phenocopied impaired retinal angiogenesis in Smad7IECKO mice. By challenging adult Smad6- and Smad7IECKO mice with two tumor models (LLC and B16F10) I found endothelial Smad6 and Smad7 to differentially affect tumor size and survival. Loss of endothelial Smad6 led to increased tumor size and higher survival during metastasis. Loss of endothelial Smad7 led to decreased tumor size and lower survival in metastasis. Interestingly, loss of endothelial Smad6 and Smad7 negated the effects from single deletion. Taken together, I found that Smad6 and Smad7 differentially regulate physiological and pathological angiogenesis but only have a nuanced or perhaps dispensable role in vascular quiescence. Preliminary data also suggests endothelial Smad6 and Smad7 may discreetly regulate primary tumor growth and metastatic dissemination.

1 Introduction

The vascular system is made up of a highly hierarchical circulatory structure of blood vessels, which transport blood throughout the body supplying surrounding tissue with oxygen and nutrients, and blind-ended lymphatic vessels that facilitate drainage of lymph back from the tissue into the bloodstream. It plays a crucial role in the development, morphogenesis and maintenance of healthy organ homeostasis, and thus is one of the earliest organs to develop during embryogenesis. The cardiovascular system pumps oxygen- and nutrient-rich blood from the lung via the heart through arteries and arterioles into capillaries that then facilitate exchange with the surrounding tissue. After gas- and nutrient exchange, veins and venules transport deoxygenated blood enriched with CO_2 and remaining waste metabolites back to the lungs where it gets oxygenated and cleared by ventilation. Blood vessels of the vascular system consist of three main cell types: vascular endothelial cells (EC), which form the innermost layer and support surrounding cell through paracrine or angiocrine factors, smooth muscle cells (SMC), which regulate structural integrity, contractility and hemodynamics in the macrovascular network (arteries and veins) and pericytes (PC), which regulate structural integrity, contractility and hemodynamics in the microvascular network (capillaries). Moreover, capillaries can be continuous with tight EC junctions (nervous system, skin, lung and heart), discontinuous with diaphragm-like pores (intestine, kidneys, endo- and exocrine glands), sinusoidal with multiple open gaps (liver, spleen and bone marrow) or specialized (Schlemm's canal in the peripheral cornea and high endothelial venule). EC and mural cells (SMC and PC) communicate through complex juxta- and paracrine signaling to promote vascular development, maintenance and activation. In recent years, local tissue-specific angiocrine signaling was shown to establish unique vascular niches deploying morphogens and growth factors that guide organ regeneration, metabolism and homeostasis. Moreover, the endothelium communicates systemically through the angiocardio-axis, thereby modulating the nervous system, immune system and metabolic processes. Decoding the intricate mechanisms of endothelial response modulators will pave the way to bolster organ health over the individual's lifespan.

1.1 Development of the vascular system

1.1.1 Vasculogenesis

The vascular system develops as early as in the third week of embryogenesis from mesodermal precursors, termed hemangioblasts (1). Hemangioblasts are embryonic progenitors of the endothelial and hematopoietic stem cell lineages that cluster together to form blood islands in the yolk sac. During the primitive streak stage, angioblasts, precursors of endothelial cells are formed on the outside, and hemocytoblasts, precursors of blood cells are formed on the inside of blood islands. Mediated by FGF2, BMP4 and VEGF, the angioblast-hemocytoblast clusters either migrate or extend, interconnect and lumenize directly to form a primordial *de novo* vascular network (2, 3). The vascular network forming from the extraembryonic mesoderm constitutes the vitelline circulation, which transfers nutrients from the yolk sac to the embryo proper and the allantois, which is responsible for placental and umbilical vessel development. This process of *de novo* formation of the endothelium, driven by ETS transcription factors, such as ETV2, from the embryonic mesoderm, is termed vasculogenesis (4). Intraembryonic vasculogenesis occurs in two spatially and temporally distinct waves. The first wave of vasculogenesis is forming the dorsal aorta from angioblasts originating at the site of vessel formation, and the second wave of vasculogenesis is forming the endocarodium, ventral aortae and posterior cardinal veins from angioblasts that migrate to the lateral sides of the embryo (5). Thus, making the dorsal aorta, ventral aortae and posterior cardinal veins the first intraembryonic vessels formed. Vasculogenic EC of the intraembryonic vessels are crucial for organogenesis as they provide inducive signals even before vascular function.

1.1.2 Arterio-venous specification

The arterial or venous fate of vasculogenic EC is determined soon after formation of primitive vascular plexi. Rapid proliferation of EC during arteriogenesis forces blood vessels to enlarge, branch and assemble into vascular tubes creating arteries and veins (6). Activation of the VEGF signaling pathway is imperative for the propensity of EC towards arterial specification, whereas dampened activation of VEGF tilts the balance towards venous specification. VEGF inhibits the phosphoinositide 3-kinase (PI3K) pathway, which in turn leads to high activity of extracellular signal-regulated kinase (ERK) pathways promoting arteriogenesis (7). In contrast, high activity of PI3K-AKT favours venous specification (8). In addition, the arterial vasculature is established in response to the initiation of blood flow leading to induction of Notch signaling and inhibition of Myc. The mechanical stimulus triggers the upregulation of connexin 37 and subsequent endothelial cell cycle arrest through p27 (9). This mechanism enables the activation of arterial specification genes, thus orchestrating the

development of arterial identity in EC. Venous differentiation is mediated through the activation of cell cycle genes via COUP-TFII. COUP-TFII induces gene expression patterns specific to the venous vasculature while suppressing gene patterns associated with arterial specification, thus establishing venous identity in EC (10). Moreover, careful regulation through TGFβ superfamily signaling was shown to balance arterial and venous fates. The endoglin (Eng)-ALK1/5 axis inhibits COUP-TFII, thus enabling arterial specification while the BMP2/4-ALK3 axis activates Ephb4 and COUP-TFII, thus enabling venous specification (11-13) (Figure 1A). Here, the common TGFβ/BMP transducer Smad4 has been shown to maintain the fluid shear stress (FSS) set point thereby consolidating arterial identity (14). Recently, a new model for arterial expansion through EC recruitment from veins and capillaries during development was proposed (15-17). Considering that arterial specification is, i. a., triggered by cell cycle inhibition and venous specification by cell cycle activation, arteries cannot enlarge through endothelial cell division (15). In this context, BMP signaling was shown to be an important transducer of endothelial flow response and instruct EC to migrate against the direction of flow and towards arteries (18).

1.1.3 Angiogenesis, anastomosis and vascular remodeling

Expansion of the primitive vascular plexus into a hierarchically-ordered mature capillary structure is driven by angiogenesis. Nutrient-deficiency and hypoxia promote the release of pro-angiogenic factors, such as VEGFs, FGFs, PDGFs and BMPs that initiate endothelial sprouting from preexisting vessels to establish blood flow and support growth and function of organ tissues. Hypoxia-inducible factor 1α (HIF1α) stabilization induces a VEGF gradient that attracts EC and leads to metabolic specialization due to the oxygen gradient along their migratory path (19). During sprouting angiogenesis, activated EC split into two dynamic and competing designations: tip and stalk cells. Tip cells are located at the leading edge of the sprout and are highly polarized, invasive cells that extend filo- and lamellipodia to migrate against the angiogenic gradient. Stalk cells are second-in-line building blocks within the angiogenic sprout. They are luminized, highly proliferative cells that follow the leading tip and constantly compete for the leading position. Tip/stalk cell specification is governed by VEGF, Notch and BMP signaling (20). VEGF binds VEGFR2 on EC which upregulates Dll4 ligand on tip cells. Dll4 from tip cells binds Notch receptors leading to lateral inhibition of the tip cell phenotype. The Dll4 antagonist Jagged1 blocks Notch signaling, thus promoting the tip cell phenotype. Notch also sets responsiveness of endothelial cells to BMP signaling (21). BMPs were shown to balance tip and stalk cell specification during sprouting angiogenesis. BMP2 induces expression of tip-cell associated genes through Dll4 and Kdr. Whereas BMP6 induced SMAD1/5, and expression of stalk cell genes (22). Neuropillin-1 (Nrp1) suppresses the stalk cell phenotype by

restricting Smad2/3 activation and in turn is down-regulated by Notch to drive stalk cell differentiation (23) (Figure 1B). When tip-tip contact is established, tip cells connect, synthesize basement membrane and form the vessel lumen by inverse membrane blebbing. Filopodia between two sprouts (head-to-head) or one sprout and a functional vessel (head-to-side) assemble and disassemble connections several times before stabilizing and depositing junctional proteins such as VE-Cadherin. At the point of contact, apical membrane initiation sites (AMIS) containing adherens junctions are formed that either through blood pressure or coalescence of isolated luminal pockets become interconnected perfused luminal space (17).

Following sprouting angiogenesis, vascular networks undergo remodeling leading to pruning and/or regression of unperfused or transient vessels. The ability of EC to sense flow through mechanosensors such as VEGFR2/CD31/VE-cadherin complexes, sphingosine-1-phosphate receptor (S1pr2) and the piezo-type mechanosensitive ion channel component 1 (Piezo1) plays a key role in vessel pruning as EC tend to migrate from low to high shear stress (24). Thus, unfavorable hemodynamic environments promote retraction of EC, and PC detachment leaving remnant basement membrane-containing 'empty sleeves' (25, 26). Subsequently, empty sleeves are degraded. Perfused but redundant or inefficient vessels are remodeled by intussusceptive angiogenesis under relatively low energy expenditure. EC on opposing vessel walls fold inward, migrate towards each other and connect. As such, the capillary vessels split longitudinally, forming intussuceptive pillars that are invaded by pericytes and myofibroblasts. Neighboring pillars merge and as a result modify the microcirculatory structure or duplicate existing vessels (27, 28).

In specialized organs, such as the corpus luteum in the ovaries, entire vascular networks undergo involution. Upon decreased metabolic demand in a vascular bed, individual EC recruit macrophages that secrete Wnt-7b, thus regulating Myc expression in EC which become apoptotic (29). In response to decreased VEGF signaling, stenosis is induced and vessel segments narrow and stretch. Reacting to hemodynamic alterations and blood flow cessation, EC and PC massively induce apoptosis in synchronized waves. Macrophages then clear cell debris by phagocytosis, again leaving 'empty sleeves' for degradation (25).

1.2 Vascular maturation and homeostasis

1.2.1 Vessel stabilization, vasomotion and pericyte recruitment

Extensive remodeling of the vasculature is a hallmark of blood vessel maturation. To restrict excessive remodeling, the vasculature has to stabilize and establish optimal perfusion of local organ tissues. To do so, vessels need to set their caliber and ensure functional vasomotion. Hemodynamic forces are crucial for caliber setting and regulation (30). Higher flow correlates with larger arteries, while immature vessels under low flow conditions prime stabilization through primary intraluminal cilia, sensitizing EC to BMP signaling (31). Indeed, the Bmp-Alk1/Eng axis, in a flow-dependent manner, stabilizes vascular caliber through regulating EC number, size, elongation and alignment (32-34). By dilating and constricting, blood vessel dynamically adapt their function to the multitude of physiological challenge (35). In response to heightened flow rates and stimulation of endothelin-1 (ET-1)-mediated nitric oxide (NO) production by EC, mural cells undergo a state of relaxation, leading to the dilation of blood vessels (36, 37). Conversely, diminished flow rates coupled with the expression of protein kinase C (PKC) and Rho kinase (ROCK) prompt mural cell contraction, resulting in vasoconstriction. This process supports the redistribution of blood flow in response to exercise and physiological processes such as uptake of nutrients in the gut or the 'fight-or-flight' response.

PC support EC in vascular stabilization by depositing extracellular matrix (ECM) components into the maturing BM and reinforcing the vessel wall. PC also induce vascular quiescence through several signaling cues (38). They activate Ang/Tie signaling through Ang-1 that binds the Tie2 receptor on EC, limiting permeability and facilitating cell quiescence. Moreover, PC can limit VEGF and Notch signaling by binding Notch ligands (DLL4, Jag1) and producing Flt-1. Cell-cell contacts directly affect polarity of EC through junctional proteins. Connexin43 (Cx43) and Connexin45 (Cx45)-containing gap junctions and N-cadherin adherens junctions provide luminal and abluminal cues to EC thereby defining apical-basal and basolateral polarity (39).

1.2.2 Mechanotransduction, endothelial quiescence and organotypic normalcy

As the vascular system matures into a fully functional and hierarchical network, the endothelium becomes quiescent. EC in the quiescent state are dormant, halt proliferation and migration, and loose expression of leukocyte adhesion molecules. Contrary to popular belief, endothelial

quiescence is not an inactive or passive state but rather is regulated by intricate mechanical and biochemical inputs into an active molecular machinery.

Blood-flow-mediated biophysical forces, or 'fluid shear stress' (FSS), is converted into several signaling and transcriptional pathways that are involved in safeguarding tissue-specific normalcy and artheroprotection. Blood pressure applies a compressive force to the surface of the cells, while friction from flowing blood creates tangential force known as shear. Stretching of blood vessel due to pressure pulses also transmits a pulling force to the vessel wall through their connections with the ECM. EC that experience FSS undergo passive deformation, measured in strain, and active deformation through cytoskeletal reorganization in response to flow. The internal tension produced by mechanical forces in connection with the dynamic metabolism of EC is necessary to exhibit their specialized characteristics. Through mechanotransducers such as receptor tyrosine kinases, ion channels, integrins and junctional proteins, EC convert mechanical stimuli into biochemical signals (40-42). Quantitative differences in mechanotransducers tilt the balance of activation or inhibition. For example in coronary arteries, mechanotransduction can be either artheroprotective or artheroprone depending on the magnitude and type of flow (43). In response to high laminar shear stress (LSS) in straight arterial segments over longer periods of time, EC align, suppress NF-kB and increase KLF2 and anti-inflammatory gene expression. Under low and turbulent shear stress (DSS) conditions in bend of bifurcate arteries, EC exert pro-inflammatory properties through PECAM1, PLXND1 and PIEZO1 (41). Similarly, thickness of the glycolyx is flow-dependent and implicated to confer atheroprotective or atheroprone properties, but whether proteoglycans such as syndecans, glypican and hyaluronic acid act as mechanotransducers is still under question (41, 44). Calveole form clusters when subjected to low tension and flatten when exposed to high tension as a protective mechanism to prevent cell rupture under high hemodynamic forces. Calveolin 1 is directly implicated as a mechanosensor during high membrane tension (41, 45). Other pathways mediating and safeguarding the EC phenotype include PI3K/AKT and MAP/ERK signaling through KLF2, integrin dependent inhibition of YAP/TAZ-JNK signaling and Notch/VE-cadherin interaction. Intriguingly, TGF-β/BMP signaling holds a dual role in mechanosensing. Signaling through BMP10/ALK2, Endoglin and the downstream Smad1/5 complex is highest in physiological FSS and supports vessel stabilization (46). Upregulation of KLF2 in response to laminar flow suppresses pro-angiogenic, artheroprone BMP4-SMAD1/5 signaling (47). In contrast, TGFβ-ALK5-SMAD2/SMAD3 signaling is a known promoter of EndMT and arterial remodeling at low and oscillatory FSS (48) (Figure 1C). The intracellular inhibitors of the TGFβ and BMP signaling pathway, Smad6 and Smad7, are implied to be regulators maintaining vascular stability (49).
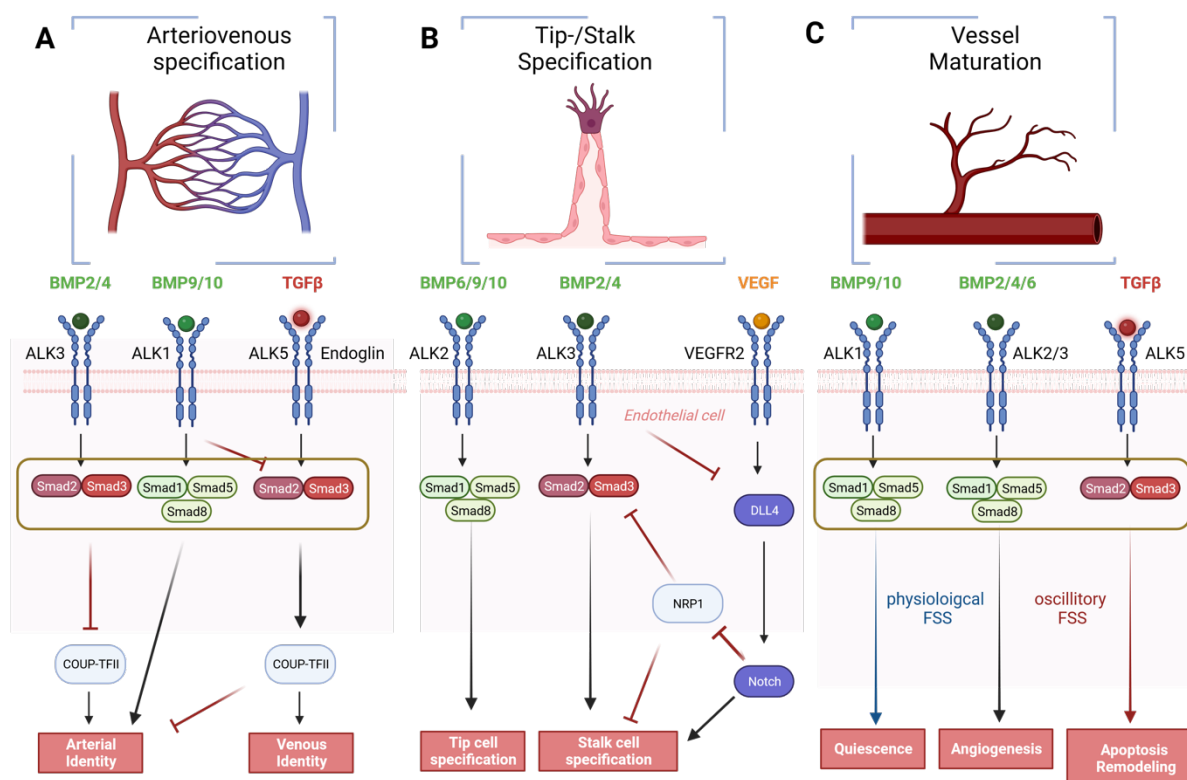
Figure 1: TGFβ/BMP signaling in vascular development and maturation.
(A) BMP2/4/ALK3 and BMP9/10/Alk1 cooperate in inducing arterial identity. BMP9/10 induces arterial identity in EC through Smad1/5/8 and BMP2/4/ALK3 supports arterial identity through Smad2/3 and inhibition of COUP-TFII. TGFβ/ALK5/Eng induces COUP-TFII expression and thus promotes venous identity. BMP9/10 supports arterial identity through Smad1/5/8 by inhibiting venous identity and blocking TGFβ/ALK5/Eng signaling through Smad2/3. (B) VEGF gradient induces Tip-/Stalk cell specification through Notch and BMP signaling. Dll4 in tip cells binds Notch receptors in stalk cells leading to lateral inhibition of tip cell phenotype. Notch relieves neuropillin-1 mediated BMP2/4/ALK3 inhibition thus favoring stalk cell phenotype over BMP6/9/10-driven tip cell specification. (C) During vascular maturation, endocrine BMP9/10 signaling maintains vascular quiescence while para- and autocrine BMP2/4/6 activates pro-angiogenic cascades. TGFβ/ALK5 regulates EC apoptosis, ECM deposition and vascular remodeling.

EC also adapt their metabolite production to preserve the quiescent state. Recently, the transcription factor FOXO1, a repressor of MYC and inducer of EC quiescence, was shown to mediate release of 2-hydroxyglutarate (2-SHG) and 3-methyl-2-oxovalerate to inhibit mitochondrial α-ketoglutarate dehydrogenase in the citric acid cycle (TCA) and induce reversible cell cycle arrest (50) (51). Moreover, constitutive cooperative expression of ETS transcription factors, ERG and FLI1, was shown to preserve physiological functions and maintain cell fate of EC. Loss of either ERG or FLI1 in EC lead to no or minor vascular abnormalities, while loss of both caused rapid death in adult mice (52).

Introduction

There is a plethora of well-studied pathways controlling vascular development, angiogenesis and maturation. The most prominent pathways include FGF, VEGF, WNT, ANG/TIE, TGFβ and BMP signaling. Increasing evidence points towards their para-, endo-, and autocrine roles in active maintenance of organotypic endothelial normalcy. Paracrine non-endothelial VEGF from podocytes in the kidney, β-cells from the pancreas or hepatocytes in the liver maintain fenestration and sinusoidal vessel structure. Continuous autocrine endothelial VEGF supports blood vessel homeostasis in several organ tissues. FGF and VEGF integrate Erk1/2 signaling thereby inhibiting TGFβ signaling thus maintaining endothelial identity systemically and fenestration in kidney and endocrine glands (53). Besides age-related cardiovascular disease, accumulating evidence also suggests age-related dysfunction of the endothelium to take, in the truest sense, the 'center' stage in limiting lifespan (54). More recently, in a landmark study, it was shown that low-levels of continuous angiocrine VEGF prevented capillary loss, improved organ function and promoted overall healthy aging and longevity (55). A classic example of a paracrine system facilitating vascular quiescence is Ang/Tie signaling. Mural cells covering mature blood vessel secrete ANG1 that binds Tie2 on EC which initiates downstream signaling through AKT and suppression of Foxo1. In pathology, such as inflammation, autocrine endothelial expression of the Tie2 antagonist Ang2 competes with Ang1 thus destabilizing and reactivating the quiescent endothelium. Deletion of Tie2 on pericytes causes pro-angiogenic effects, indicating that Ang/Tie signaling acts bi-directionally and reciprocal on EC and PC (56).

The Wnt/ β-catenin signaling maintains tight junction formation during development of the central nervous system (CNS) and blood-brain barrier (BBB) (57). Vascular differentiation in the CNS is mediated by WNT7A, WNT7B and norrin (58). In the BBB, EC differentiation and stabilization is mediated by Glut-1 and junctional proteins Claudin-3 and Claudin-5 (59, 60). PLVAP, which is responsible for size-selective entry of antigens into the blood stream and vascular permeability is down-regulated in response to WNT pathway activation (61). Wnt activation was also shown to increase Zeb1 expression forcing endothelial progenitors into quiescence (62).

1.3 Tumor Angiogenesis

Numerous pathologies, including cancer, atherosclerosis, arthritis, psoriasis, endometriosis, obesity, age-related macular disease and recently SARS-CoV-2 (COVID-19) infection, recapitulate processes occurring during developmental angiogenesis (63-66). In pathology, angiogenesis often transpires without functional homeostatic feedback mechanisms leading to an abnormal vasculature. Abnormal or dysfunctional blood vessels often times lack proper pericyte coverage, have increased permeability and exert a pro-fibrotic phenotype. Identifying inducer of endothelial homeostasis, and blood vessel normalization, thus has the potential to open therapeutic options in a variety of diseases associated with pathological neovascularization.

Cancer was firstly associated with aberant angiogenesis when Judah Folkman in 1971 postulated that tumors require blood vessel to grow (67, 68). Natural diffusion limits the spatial distribution of cells to the next source of nutrients and oxygen. Thus tumors typically cannot exceed a distance of 100-150um to the nearest blood vessel before becoming necrotic and hypoxic. To circumvent this limitation, tumor cells in response to hypoxia and oncogene activation exploit both angiogenesis-dependent and independent strategies to secure nutrition. Upon reaching its avascular growth potential, tumors undergo an 'angiogenic switch' hijacking the endogenous endothelium through increased production of pro-angiogenic factors and force neovascularization by sprouting angiogenesis. The angiogenic switch initiates the transition of avascular tumor cell clusters into large, vascularized tumors (69). In an angiogenesis-independent manner, tumor cells can force blood vessel to elongate and co-opt along the vessel wall securing their nutrition and oxygenation from the perivascular space. A much rarer phenomenon in highly aggressive tumors associated with drug resistance is vasculogenic mimicry by which tumor cells themselves acquire EC features causing tubular structure formation (70). Unlike in controlled blood vessel growth during development, oversaturation of pro-angiogenic factors in the tumor microenvironment results in malformed, unorganized vascular networks with disrupted endothelial junction, pericyte detachment and increased fluid pressure within the tumor vessel.

1.3.1 Vascular normalization in cancer

Anti-angiogenic therapy emerged with the primary objective of targeting tumor growth through the inhibition of angiogenesis, thereby aiming to deprive tumors of their blood supply. Main targets for anti-angiogenic therapy in cancer include VEGF (Bevacizumab, Aflicercept), VEGFR2 (Ramucirumab), PDGFRα (Olaratumab) and tyrosine kinases (TKIs: tyrosine kinase inhibitors) (71).

Introduction

Apart from classical pro-angiogenic factors, tumor-derived exosomes containing soluble proteins and non-coding RNAs were shown to promote angiogenesis and to be potential targets for anti-angiogenic therapy (72-75). In ovarian cancer, soluble E-cadherin induced β-catenin and NFkB signaling in EC (74). In hepatocellular carcinoma (HCC), miR-210 enhanced angiogenesis through inhibition of SMAD4 and STAT6 (75).

With the approval of bevacizumab, some progress was achieved in terms of modest improvements in progression-free survival (PFS). However, this therapy also brought forth certain challenges, such as toxicity causing hypertension, organ failure, impaired drug delivery and enhanced cancer metastasis (71, 76). In light of the somewhat disappointing outcomes observed in clinical trials, in 2005, Rakesh Jain proposed to facilitate drug delivery through a process called vascular normalization (77, 78). This approach aims to restore the abnormal tumor vasculature to a more normalized state, potentially enhancing drug accessibility and delivery into the tumor microenvironment (TME). In the pre-clinical setting, treatment of several primary tumors with Tie2-activating and Ang2-inhibiting antibodies lead to vascular normalization, including tightening of EC-junctions, increased pericyte and BM coverage and enhanced drug delivery to the tumor (79). In refractory metastatic colorectal cancer patients, treatment with Fruquinitinib, a potent oral inhibitor of VEGFRs, resulted in a clinically meaningful benefit of OS compared to the placebo group (80). Anti-angiogenic therapy also emerged as a promising approach to enable cancer immunity by priming the TME for immune checkpoint inhibitor (ICI) therapy (81). Efficacy of ICI therapy directly correlated with the enhancement in vessel perfusion, supporting the rational for combinatorial therapies (82). Tumor vessel normalization caused by dual Ang2 and VEGF inhibition synergized with PD-1 checkpoint blockade and led to increased extravasation and perivascular accumulation of CD8+ cytotoxic T lymphocytes (CTLs) (Schmittnaegel et al., 2017). Targeting the stimulator of interferon genes (STING) pathway is a novel immunotherapeutic approach that promotes vascular normalization and enhances antitumor response to ICI (83). Combination of STING agonists with VEGFR2 blockade overcame monotherapy resistance and led to complete tumor regression showcasing the importance of vascular normalization as an enabler of cancer immunotherapy (84). The IMbrave150 and ORIENT-32 landmark phase 3 clinical studies in HCC showed remarkable improvement of objective response rate (ORR, 30%) and 5.8 year improvement in OS in patients treated with combination therapy of anti-VEGF (Bevacizumab)/anti-PDL1 (Atezozilumab), or Bevacizumab/PD1 (Sintilimab) compared to the standard of care sorafenib (85, 86).

1.4   Angiocrine signaling in organ regeneration and tumorigenesis

Even during quiescence, EC retain responsiveness to pathological reactivation cues and actively maintain a tissue-specific microenvironment through a diverse array of membrane-bound or secreted para-, juxta- and endocrine, or 'angiocrine' factors. Angiocrine factors from healthy EC in specialized capillaries maintain organ homeostasis and regulate the response to inflammation and injury while angiocrine factors from tumor EC can modulate immune invasion, induce the metabolic changes and prime the TME or pre-metastatic niche.

These include growth factors, tophogens, chemokines, cytokines, ECM components and morphogens that shape tissue morphology during regeneration. By relaying intra- and extravascular cues to tissue-specific stem and progenitor cells in the parenchyme through its basolateral surface, and to stem and immune cells in the circulation through its luminal surface, the endothelium orchestrates processes involved in organ regeneration and tumorigenesis.

1.4.1   Angiocrine maintenance of the cardiovascular system

As EC transition from fetal to the adult stage ETS transcription factors enforce endothelial cell fate by programming the epigenetic enhancer landscape priming homeostatic angiocrine signaling (52, 87). Age-related changes in homeostatic angiocrine cascades, such as increase in Sema3A, can directly affect the neurovascular interface and function of the aging heart (88). Contrary to the adult or aged heart, the neonatal heart regenerates with little to no scar formation. Several angiocrine factors were implied in favoring healing without fibrosis during cardiac repair in the neonatal heart (89-93). EC- driven ECM modulation shapes a microenvironment that allows plastic repair by cardiac progenitor cells. Follistatin 1 has been shown to exert pro-regenerative properties when secreted from the epicardium, and insufficiency in EC leads to atrial and venous wall fibrosis (92, 93). ECM components, such as argin, improve heart function and reduce ischaemia-reperfusion injury while different periostin isoforms either induce proliferation of differentiated cardiomyocytes or prevent cardiac rupture in the infarcted heart (89, 94, 95) (Figure 2A). As to what modulators might shift the balance of response to injury from pro-fibrotic 'scar formation' to a regenerative matrix profile in the adult heart remains to be seen.

1.4.2   Angiocrine maintenance of the liver

The adult liver has the unique capability to regenerate up to ¾ of its mass after surgical removal or chemical injury to sustain physiological homeostasis. Due to diverse metabolic functions of the liver parenchyme such as bile acid and cholesterol production, glucose storage, metabolic waste

clearance, regulation of blood clotting, detoxification and immunesurveillance of pathogens, the liver is continuously exposed to environmental stressors. To retain functionality, hepatocytes, Kupffer cells, sinusoidal liver EC (LSEC) and cholangiocytes have to maintain their proliferative capacity. The vascular endothelium supports tissue regeneration in the liver by tightly communicating with hepatocytes in a spatiotemporal manner. Down-regulation of Ang2 in LSEC reduces angiocrine TGFβ-1 in turn mediating hepatocyte proliferation in the inductive phase of regeneration followed by upregulation of Ang2 enabling regenerative angiogenesis of LSEC (96). Spatial sorting revealed transcriptomic and metabolic zonation of hepatocytes and LSEC from the portal to central vein (97, 98). Metabolic zonation is crucial for homeostatic liver function and is tightly controlled by integrin-mediated mechanotransduction as well as VEGFR-, WNT-, RSPO3-, BMP- and Stabillin–mediated angiocrine signaling (99-104) (Figure 2B). Based on the identified zonation profiles, region-specific tyrosine kinase phosphorylation was found to selectively regulate Tie receptor-dependent vascular Wnt activation of angiocrine signaling during liver regeneration (105).

Depending on their spatial location, LSEC have varying proliferative capacity and hepatic stellate cells either proliferate or strongly induce matrix remodeling in response to acute injury (106). Following long-time exposure to injury, efficiency of liver regeneration decreases and regenerative processes gradually shift to pro-fibrotic programs which in advanced stages can lead to cirrhosis and hepatocellular carcinoma (HCC). It is key to determine how the endothelium communicates with the parenchyme to drive functional regeneration as opposed to scar formation and dysfunction. Recently, transcriptional activation of GATA4 induced by BMP9 was identified as a major determinant of sinusoidal EC fate in the postnatal liver and protector from MYC and PDGFb-mediated excessive liver fibrosis (107, 108). In aging, LSEC senescence due to age-related inactivation of endothelial C-kit caused capillarization and steatosis implicating defective angiocrine communication to be a driver of metabolic disorders (109).

1.4.3   Angiocrine maintenance of the lung

The alveolar-capillary environment in the lung requires a specialized continuous endothelium that controls vascular permeability, protects against oxidative stress and retains plasticity in response to injury and disease. Pulmonary capillaries surround the alveolar sac and consists of EC subpopulations, termed gCap and aCap. Aerocytes, or aCap, are morphologically complex, large cells that span multiple alveoli, rarely proliferate and are mainly responsible for gas exchange. gCap are capillary stem cells that retain distinctive reparative capacities and replenish the pulmonary endothelium in response to injury (110, 111). Moreover, angiocrine signaling can directly instruct

and support lung repair. Endothelial Rspo3 was shown to prime macrophages for metabolic-epigenetic reprogramming and resolve lung inflammation (112). Other angiocrine factors supporting alveolar regeneration include secretion of MMP14, EGF and apelin and recruitment of Cxcl12-producing platelets (113-115) (Figure 2C). In pulmonary fibrosis, the regenerative capabilities of the endothelium are impaired, and fibrotic tissue accumulates and replaces functional alveolar structures. Here, knockout of angiocrine Flt1 was shown to act anti-fibrotic and promote alveolar regeneration through epithelial transdifferentiation (116).

1.4.4 Angiocrine signaling during tumorigenesis

Following the acquisition of an angiogenic phenotype and the abnormal vascularization of the tumor, the tumor-specific endothelium remains in an active state that contributes to a pro-tumorigenic microenvironment. Tumor EC are active and have distinct genetic profiles from healthy EC which translates in differential surface receptor composition and activation of angiocrine cytokine release. This 'angiocrine switch' also establishes increased sensitivity of EC to cancer-derived factors that trigger context-dependent local and systemic angiocrine cascades affecting tumorigenesis and the metastatic niche (117-119). Angiocrine signaling in the bone was shown to affect pericyte composition, lead to blood vessel remodeling and confer therapy resistance in bone metastasis (120). In a landmark study, the endothelium systemically amplified primary tumor signals by increasing expression of the TGFβ modulator LRG1 thus priming the metastatic niche (121). This systemic crosstalk can be either beneficial or detrimental for health. In case of ANGPTL4, systemically circulating N-terminal fragment was shown to reduce vascularity and metastasis in preclinical models of melanoma and lung cancer while the primary-tumor derived C-terminal fragment had the opposite effect facilitating metastatic dissemination (122) (Figure 2D).
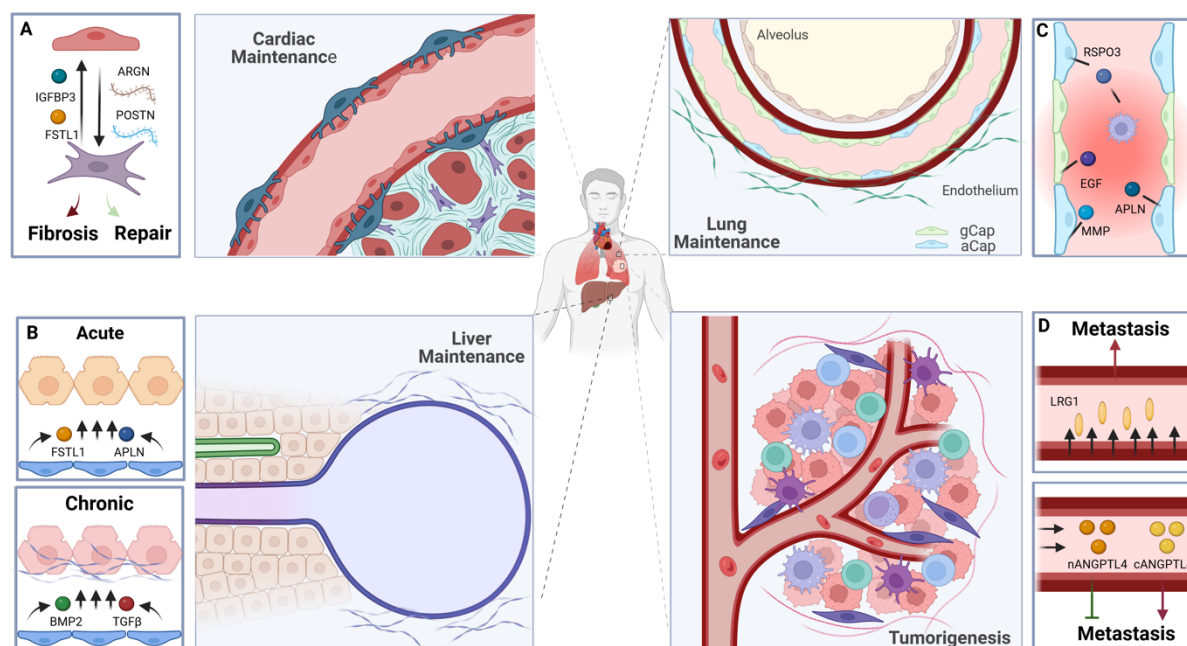
Figure 2: Angiocrine maintenance of organ regeneration and tumorigenesis.
(A) Angiocrine factors such as IGFBP3 and FSTL1 and ECM components such as ARGN and POSTN favor cardiac repair over cardiac fibrosis by establishing a regenerative microenvironment. (B) In acute liver injury, angiocrine FSTL1 and APLN facilitate healing without fibrosis while upregulation of angiocrine TGFβ and BMP2 causes healing with fibrosis. (C) Angiocrine signals such as RSPO3, EGF, APLN and MMPs direct macrophages and platelets to resolve inflammation and enable regenerative capacity of capillary stem cells (gCap). (D) Systemic upregulation of LRG1 by the endothelium promotes metastasis in a STAT3-dependent manner. Systemically circulating nANGPTL4 acts on the endothelium reducing vascularity and metastasis while primary tumor-derived cANGPTL4 promotes metastasis.

1.5 The TGFβ superfamily

1.5.1 TGFs

In 1972 Tadaro and Huebner revolutionized our understanding of the malignant transformation of healthy cells by postulating that the vertebrate genome contains dormant viro- and oncogenes and that expression can be reactivated by carcinogens, mutagens and radiation driving neoplastic transformation (123). Todaro, Sporn and Holley could show that transformation is not only driven by oncogenes but also by secretion of autocrine growth factors and increased sensitivity by malignant cells (124-127). These growth factors were termed transforming growth factors (TGFs) due to their ability to induce anchorage independent growth in fibroblasts associated with malignant transformation (128, 129). It was later found that TGFs were not restricted to inducing transformation in malignant cells, or solely autocrine function, but could compete for epidermal growth factor (EGF) receptors in a variety of cell lines and types enabling critical cell- and context-dependent processes in development, differentiation, homeostasis and disease (130-132). TGFβ

signaling initiation is mediated by two TGFs, TGFβ-1 and TGFβ-2. Upon stimulation, the type I serine threonine kinase receptor, TGFβrI (ALK5), forms a heterotetrameric complex with the dimerized type II receptor TGFβrII transducing downstream signaling by SMAD phosphorylation (133). TGFβrIII receptors, such as endoglin expressed exclusively on EC and betaglycan expressed on a variety of cell type with little to no expression on EC, are accessory receptors regulating access of ligands to receptor heterotetramers (134, 135).

The groundbreaking discovery of all of its highly conserved 33 members, and the extensive characterization of TGFs, bone morphogenetic proteins (BMPs/GDFs), Activins and Nodals acted as a pivotal catalyst, igniting extensive scientific and therapeutic exploration into the pleiotropic cell- and context-specific role of the TGFβ superfamily (136, 137).

1.5.2 BMPs

Initial observations of the regeneration of aseptic bone cavities through decalcified bone transplantation by Senn in 1889 and bone formation through autoinduction by Urist in 1965 laid the foundation for the discovery of BMPs as bioactive factors involved in bone morphogenesis (138, 139). BMPs share their highly conserved structure with members of the TGFβ family and contrary to initial assumptions exert a vast variety of biological functions outside bone morphogenesis (140-142). BMP ligands are generally classified into subgroups with varying type I receptor binding affinities (BMP2/4; BMP5/6/7/8; BMP9/10 and BMP12/13/14) based on structural and functional homology (140). However, ligands with high affinity for specific type I receptors can outcompete low affinity ligands of the same family (143). Thus, more recently, classification by contextual ligand equivalence based on combinatorial signaling logic across cellular contexts was proposed (144). Signaling is mediated through seven type I (ALK1-7) and three type II (BMPRII, ActRII and ActRIIB) serine-threonine kinase receptors (133). In the vascular endothelium, the most important type I BMP receptors include the EC-specific ALK1 (ACVRL1) and the more broadly expressed ALK2 (ACVR1) and ALK3 (BMPR1A) (34). The signaling outcomes of both TGFβ- and BMP-mediated signaling in EC is determined by ligand availability (BMP2, 4, 6, 9, 10; TGF- β1 and 2) and type I receptor heterogeneity (ALK1, ALK2, ALK3, ALK5). Most prominent canonical transducer of downstream signaling are SMAD Proteins.

1.5.3 SMADs

To initiate signaling, TGFβ and BMP type II receptors phosphorylate the glycine-serine (GS) enriched domain of the type I receptors that in turn phosphorylate the carboxyl termini of downstream receptor SMADs (R-SMAD). TGFβrI preferentially phosphorylates R-SMAD2 and 3 while BMPRI

phosphorylates R-SMAD1/5 and 8. Phosphorylated SMAD2 and 3 or SMAD1, 5 and 8 form homo- and heteromeric complexes with SMAD4 (Co-SMAD) and get translocated into the nucleus where they cooperate with other transcription factors to bind DNA and either activate or repress transcription (145). Moreover, they are subject to extensive posttranscriptional modification and recruit chromatin modifiers that can remodel histones and the chromatin structure and (Hill, 2016). Although seemingly simple, these complexes can regulate hundreds of targets genes at the same time, in the same cell and under tightly controlled conditions (146). To resolve combinatorial complexity of SMAD proteins and understand their functional outcomes, modeling approaches have been developed that link SMAD complex formation to gene expression (147). Another group of SMAD protein comprise the inhibitory SMAD (iSMADs), intracellular regulators of TGFβ and BMP signaling. By recruiting ubiquitin ligases Smurf1/2 or protein phosphatases, interfering with R-SMAD/Co-SMAD complex formation or inhibiting SMAD-DNA binding, Smad6 and Smad7 negatively regulate TGFβ and BMP-mediated signal transduction (148-151).

1.5.4 Vascular MADs – intracellular inhibitors of the TGFβ superfamily

Initially identified as vascular MADs with a selective expression pattern in atherosclerotic human carotid arteries, iSMADs play a crucial role as intracellular negative feedback inhibitors of the TGFβ superfamily in the vasculature (152). The expression of iSMADs in the vascular endothelium is triggered by stimulation of the TGFβ/BMP pathway, as well as through physiological fluid mechanical forces (Kulikauskas, X, & Bautch, 2022; Ricard et al., 2019; Topper et al., 1997).

A plethora of studies has shown the involvement of TGFβ/BMP signaling as key cascades in vascular development, maturation, and malformations (see Figure 1 and 3) but mechanistic integration of iSMADs remains sparse (H. W. Lee et al., 2017; Ola et al., 2018; Yan, Zhang, Miyazawa, & ten Dijke, 2022). Global deletion of either Smad6 or Smad7 results in predominant embryonic lethality *in utero* with few mice surviving after birth. Lethality associated with loss of Smad6 is characterized by widespread hemorrhages and disrupted endothelial cell junctions (18). In patient-resected brain arteriovenous malformations (bAVMs), Smad6 downregulation correlates with microhemorrhages and cell-cell junction deficiencies (153). In contrast, lethality associated with global deletion of Smad7 results in edema and defects of cardiac development, while misexpression in the developing chick head and limb induces dilated and merged arteries (154, 155). Intriguingly, signaling through TGFβRI/TGFβRII upstream of Smad7 was shown to drive a pro-inflammatory vascular phenotype and act as a major player in atherosclerosis and endothelial-mesenchymal transition (53, 156). Overall,

iSMADs were shown to be important regulators of vascular stabilization and cardiogenesis during embryonic development with potential clinical implications.

1.5.5 Endothelial TGFβ/BMP signaling maintains vascular normalcy

Vascular normalcy is actively maintained by continuous signaling inputs. Several pathologies including angiogenic ocular conditions, pulmonary arterial hypertension (PAH), hereditary hemorrhagic telangiectasia (HHT) and juvenile polyposis are caused by genetic and functional disruption of endothelial TGFβ- and BMP- signaling that balances endothelial quiescence and activation.

Ocular conditions driven by pathological angiogenesis and fibrosis are the leading cause of irreversible blindness in developed countries. Retinopathy of prematurity (ROP), diabetic retinopathy (DR) and age-related macular degeneration (AMD) are characterized by pathological neovascularization and hemorrhages driven by excessive VEGF signaling in response to inflammation, hypoxia and oxidative stress (157). While anti-angiogenic monotherapy, with few exceptions, has only shown limited success in impacting overall survival (OS) during cancer treatment, treatment of angiogenic ocular disease by inhibition of VEGF or receptor tyrosine kinase has proven to be highly effective in preventing irreversible blindness (158). Nevertheless, treatment resistance, limited efficacy in patient subpopulations, burden of treatment and relapse of pathological angiogenesis requires novel targets to restore and fine-tune functional endothelial homeostasis (159). During neovascularization, VEGF, Notch and TGFβ/BMP signals are entangled and can converge into common downstream outputs. BMPs vary in spatial and temporal regulation that balances both pro- and anti-angiogenic downstream signals, making them relevant targets for vascular normalization (160, 161). BMP 2/4/6 are endothelium-specific pro-angiogenic targets of VEGF that act through TAZ-Hippo signaling (162). Activation of the TGFβ switch through LRG1 contributes to the pathogenesis of retinopathies and antibody treatment targeting the VEGF-independent angiogenic axis led to retinal vessel normalization (157, 163) (Figure 3A).

Approximately 29% of PAH patients carry a mutation in the BMPR2 gene and carriers often show early onset of disease (164). Rare variants also include mutations in ALK1, GDF2/BMP9 and Smad8/9 (165). Disruption of BMP signaling in PAH results in a TGFβ switch that favors TGFβ1-mediated signaling leading to apoptosis, vascular remodeling, narrowing of the arterial lumen and formation of plexiform lesions (166) (Figure 3B). Signaling by BMP9/10, the only known endocrine ALK1 ligands, strongly correlates with BMPRII expression and is implied in supporting vascular quiescence (167). BMP10 is mainly produced in the heart and released into the circulation where it was shown to

establish and maintain the arteriovenous network. BMP9 is mainly produced in the liver and therapeutic administration was shown to enhance BMPRII function and reverse PAH in a BMPRII-mutated PAH mouse model (168). TGFβ and BMP signaling in PAH also appears to be highly sex-dependent, with estrogens and androgens affecting expression of BMP receptors and disease prevalence (169).

HHT is an autosomal dominant disorder firstly observed by Barbington in 1865 and characterized as a syndrome by Rendu, Osler and Weber in 1896 (170, 171). It includes several disease types (HHT type I – V and JPHT) diagnosed by the Curaçao criteria with varying clinical manifestations including epistaxis, mucocutaneous telangiectasia and visceral AVMs in the central nervous system (including retinal vasculature), gastrointestinal tract, lung, liver and brain (172). HHT type characteristics depend highly on mutations of specific BMP pathway members. HHT type I is characterized by mutations in the surface co-receptor ENG (Endoglin) (Figure 3C), HHT type II by mutations in the type I receptor ACVRL1 (ALK1) (Figure 3D), HHT type V by mutation in the BMP-ligand GDF2/BMP9 (Figure 3D) and JPHT by mutations in intracellular signaling transducer SMAD4 (Co-Smad) (Figure 3E). The molecular basis of HHT type III and HHT type IV remains unresolved with studies suggesting genetic mutations originating in unidentified genes of chromosome 5 and 7, respectively (173, 174). Recently, exome sequencing of patients with HHT of unknown origin revealed new genetic drivers including INHA, HIF1A, JAK2, DNM2, POSTN, ANGPTL4, FOXO1 and SMAD6 (175). Overall, the majority (>97%) of HHT cases diagnosed by the Curaçao criteria can be traced back to mutations in endothelial BMP signaling placing the intricate TGFβ/BMP signaling balance at the epicenter of actively maintained endothelial quiescence (176). Contrary to PAH, BMP9 is only supporting BMP10 function with limited compensatory capabilities and therapeutic potential in HHT (177). Reinstating BMP10 signaling in AVMs of HHT proves to be a superior therapeutic target to reestablish vascular normalcy, as therapeutic administration of BMP10 but not BMP9 rescued retinal AVM formation in a BMP9/10-dKO and EngIECKO HHT mouse model (177).
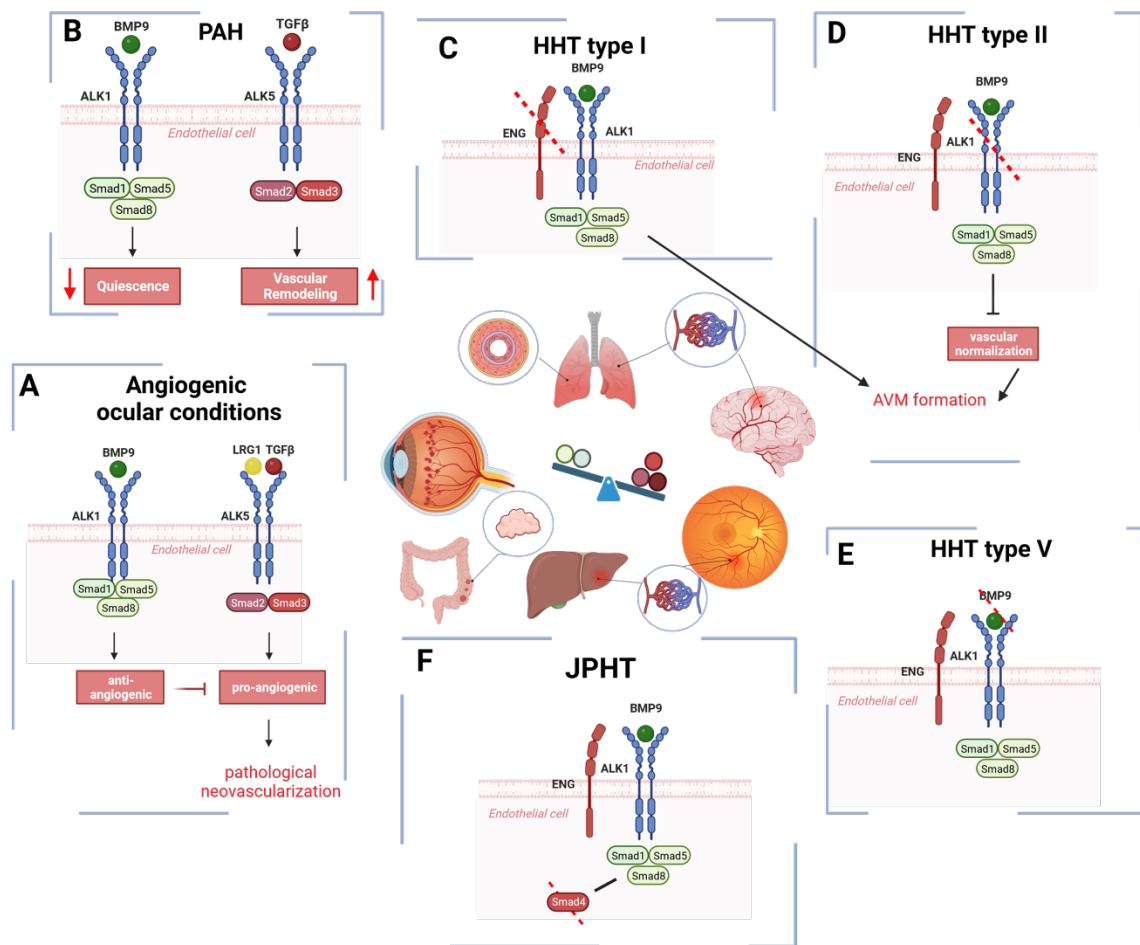
Figure 3: Vascular malformations associated with TGF-β/BMP signaling dysfunction.
(A) BMP9/ALK1 signaling maintains homeostatic function of EC by counteracting TGFβ-mediated pathological activation and neovascularization. Defunct balancing or over-stimulation of the pro-angiogenic branch leads to pathological neovascularization associated with angiogenic ocular conditions. (B) In pulmonary arterial hypertension (PAH) both endothelial BMP9/ALK1 signaling and TGFβ/ALK5 signaling were shown to contribute to PAH pathogenesis causing vascular constriction and subsequent vascular remodeling. (C) Mutations in the ENG gene account for 25%- 65% cases of Morbus Olser, or hereditary hemorrhagic telangiectasia (HHT Type I). (D) Mutations in ACVRL1 (ALK1) account for 40-60% of HHT cases (HHT Type II). (E) Mutations in the GDF5/BMP9 gene account for >1% of HHT cases (HHT type V). (F) Mutations in the SMAD4 causes a combination of HHT and juvenile polyposis (JP) in 1-2% cases (JPHT). Overall, homeostatic balancing of the TGFβ / BMP pathway is crucial to maintain vascular quiescence and mutations in the TGFβ/BMP signaling pathway account for >75% of HHT cases.

2 Aim of the thesis

Resolving the epigenetic and transcriptomic programs that drive vascular quiescence and maturation, Schlereth *et al.* identified endothelial TGF-β signaling as one of the most significantly regulated pathways during transition to vascular quiescence. The iSMADs ranked among the most hypomethylated genes correlating with transcriptional upregulation in the quiescent adult lung endothelium (49). The importance of the TGF-β/BMP signaling balance in vascular malformation, the selective induction of iSMADs under steady laminar flow and the observed early embryonic lethality upon global deletion indicate an intricate role of endothelial iSMADs in the regulation of TGFβ/BMP signaling during vessel development and maturation that has yet to be understood.

The aim of this doctoral thesis was to study how iSMADs regulate and incorporate endothelial TGFβ and BMP signaling during vascular development, maturation, and tumor pathology. In particular, I aimed:

1) to observe whether inhibition of TGF-β and BMP signaling is required to establish and maintain endothelial quiescence

2) to study how iSMAD harmonize TGF-β and BMP-mediated endothelial activation in vascular development and maturation

3) to determine whether iSMADs are a potential target to modulate endothelial cell behavior in tumor angiogenesis and metastatic dissemination

3 Results

3.1 Endothelial iSMAD in embryonic development

3.1.1 iSMAD expression over the lifespan

Smad6 and Smad7 have previously been implied in the regulation of embryonic development and endothelial polarization, but the role of endothelial iSMAD over the lifespan remains elusive (18, 154). To investigate how endothelial *Smad6* and *Smad7* are expressed throughout development, maturation and quiescence over the lifespan, I isolated embryonic and lung EC from different stages of mouse development by FACS and analyzed *Smad6* and *Smad7* gene expression by RT-qPCR. Lung tissue was used for gene expression analysis since it has been previously described to highly express iSMAD in the vasculature (49). E13.5 was the earliest observed time point as it allowed for efficient FACS sorting of EC for RT-qPCR. EC from 6-8 day old mice are in the active postnatal angiogenic state whereas EC from adult 6-8 week old mice are quiescent. EC from 8-, 12- and 18-month-old mice are in a mature or aged state. *Smad6* and *Smad7* expression gradually increased throughout development reaching a plateau at 8 weeks (Figure 4A, B).
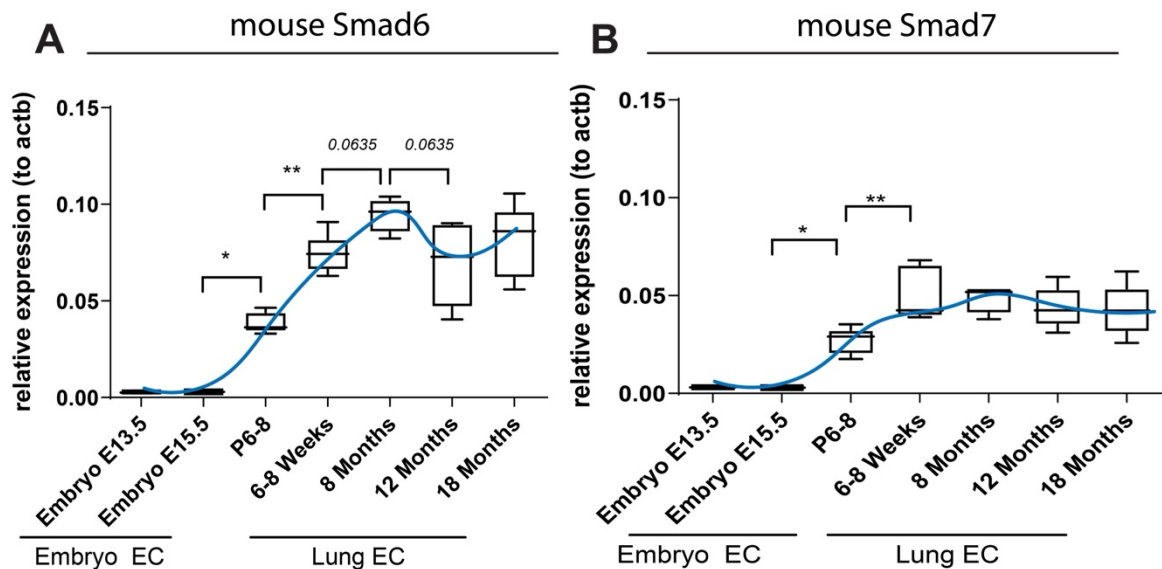
Figure 4: Endothelial iSMAD expression increases during development reaching a plateau in adults. (A-B) Gene expression analysis of mouse Smad6 (A) and Smad7 (B) in EC sorted from embryos and lungs over lifespan. Data are shown as boxplots with Q1/Q3 quartiles and min to max. *P<0.05, **P<0.01, n = 5-6. Data are not significant if not indicated otherwise. Mann-Whitney *U* test.

3.1.2   Generation of inducible endothelial-specific iSMAD KO mice

To study the role of endothelial iSMADs in vascular development and quiescence, I generated Smad6$^{fl/fl}$ mice from Smad6^{tm1a} embryonic stem (ES) with the support of the DKFZ Transgene Service (Figure 5A) and acquired Smad7$^{fl/fl}$ mice from the Jackson Laboratory (178). Cdh5^{CreERT2} mice were provided by Prof. Ralf Adams (179). Smad6$^{fl/fl}$ and Smad7$^{fl/fl}$ mice were either crossed directly with Cdh5^{CreERT2} mice (from here on Smad6WT, Smad6IECKO; Smad7WT, Smad7IECKO) or to each other (Smad6$^{fl/fl}$ x Smad7$^{fl/fl}$) and then with Cdh5^{CreErt2} mice (from here on Smad6/7WT, Smad6/7IECKO) (Figure 5B). The generated mouse models allowed for efficient temporal single and double deletion of the intracellular inhibitors of TGFβ- and BMP-mediated signaling upon tamoxifen administration. This allowed to study functions of endothelial iSMADs throughout vascular development, quiescence, and pathology. To confirm the functionality of the mouse model and analyze the effect of endothelial iSMAD deletion on survival after embryonic deletion, I deleted iSMADs in the endothelium by administration of three doses of 50ug Tamoxifen via oral gavage at E8.5, E9.5 and E10.5 into cre-mothers ensuring deletion only in the embryos (Figure 5C). I confirmed *in vivo* deletion efficacy in placentas of Smad6IECKO and Smad7IECKO mice via RT-qPCR, which showed a mean downregulation of *Smad6* of 72% and of *Smad7* of 67% (Figure 5D).
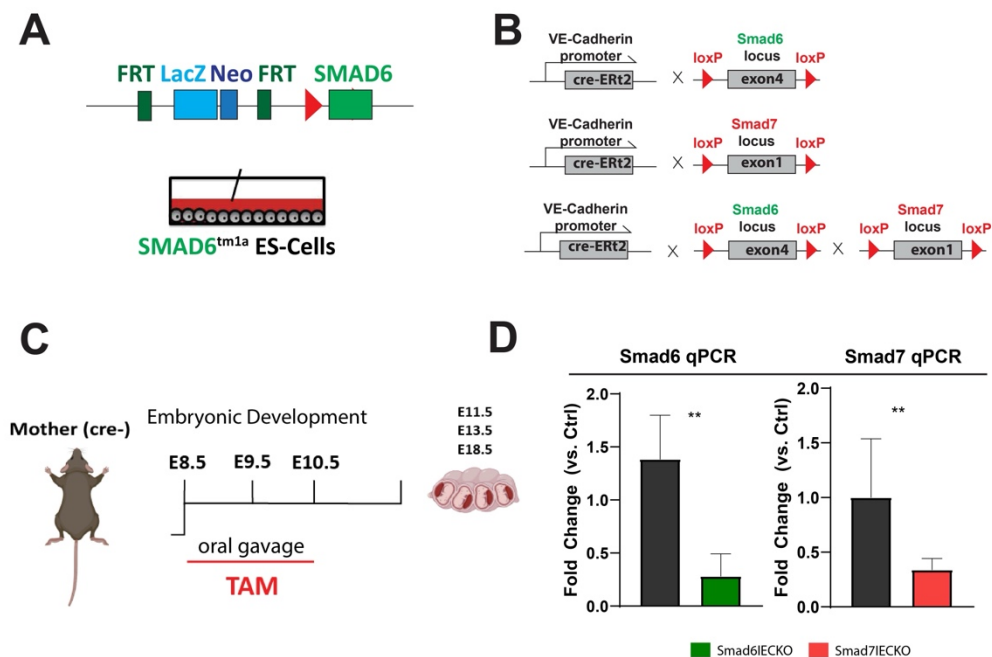
Figure 5: Embryonic deletion of Smad6 and Smad7 in mouse EC
(A) Embryonic Stem cells (ES) cell with Smad6tm1a mutation cassette flanking the Smad6 gene for recombination (B) Crossing strategy for generation of inducible endothelial-specific iSMAD-KO mice (IECKO) (C) Schematic representation of knockout induction. Endothelial iSMAD were deleted by treating cre-negative mothers with three doses of 50µg Tamoxifen according to the depicted treatment schedule. Embryos were collected at E11.5, E13.5 and E18.5. (D) Gene expression analysis of mouse *Smad6* and *Smad7* in the placenta after knockout induction. Data are shown as mean ± SD. **P<0.01, n=6. Mann-Whitney *U* test.

3.1.3 Embryonic deletion of endothelial Smad6 leads to lethality with moderate penetrance due to hemorrhages

I collected embryos after the deletion of endothelial Smad6 in Smad6IECKO mice at E11.5 (Figure 6A) E13.5 (Figure 3B) and E18.5 (Figure 6C) as described in section 2.1.2. Smad6-deficient embryos displayed pronounced hemorrhages in all three embryonic stages. Hemorrhages at E11.5 were mainly localized in the head and neck as well as lower body regions (Figure 6A). Mutant embryos displayed severe jugular and abdominal hemorrhages at E13.5 and widespread hemorrhages all over the body surface at E18.5 (Figure 6B-C). Out of 29 collected embryos, 22 were viable, 4 survived until E11.5 and 3 until E18.5 during collection indicating lethality with moderate penetrance (~25%) of Smad6IECKO embryos (Figure 6D).

D	Total [n]		
	29		
	Alive [n]	Dead [n]	WT/KO ratio
	22	7	1.75/1
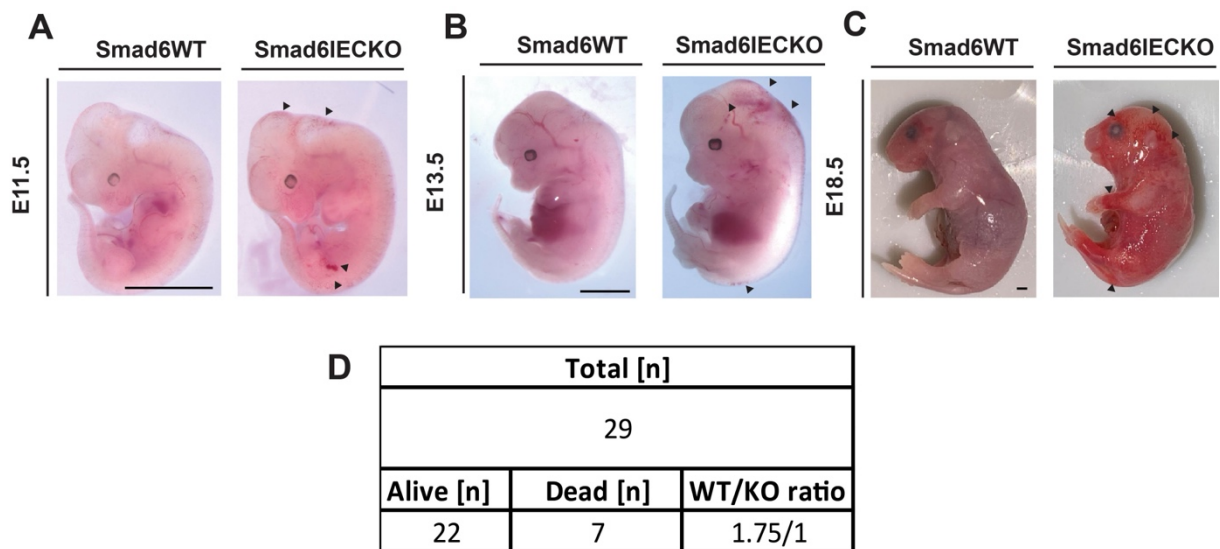
Figure 6: Embryonic deletion of endothelial Smad6 leads to widespread hemorrhages.
Representative images of E11.5 (A), E13.5 (B) and E18.5 (C) WT and Smad6IECKO embryos. (D) Table depicting lethality and WT/KO ratio of surviving mice after Tamoxifen administration. n=29 independent samples were used per experiment. Scale Bar: 1mm.

3.1.4 Embryonic deletion of endothelial Smad7 is not lethal

I further collected embryos after endothelial Smad7 deletion in Smad7IECKO mice at E11.5 (Figure 7A) E13.5 (Figure 7B) and E18.5 (Figure 7C). Smad7-deficient embryos appeared normal in all three embryonic stages. Out of 21 collected embryos, all were viable during collection showing no lethality in Smad7IECKO embryos (Figure 7D).
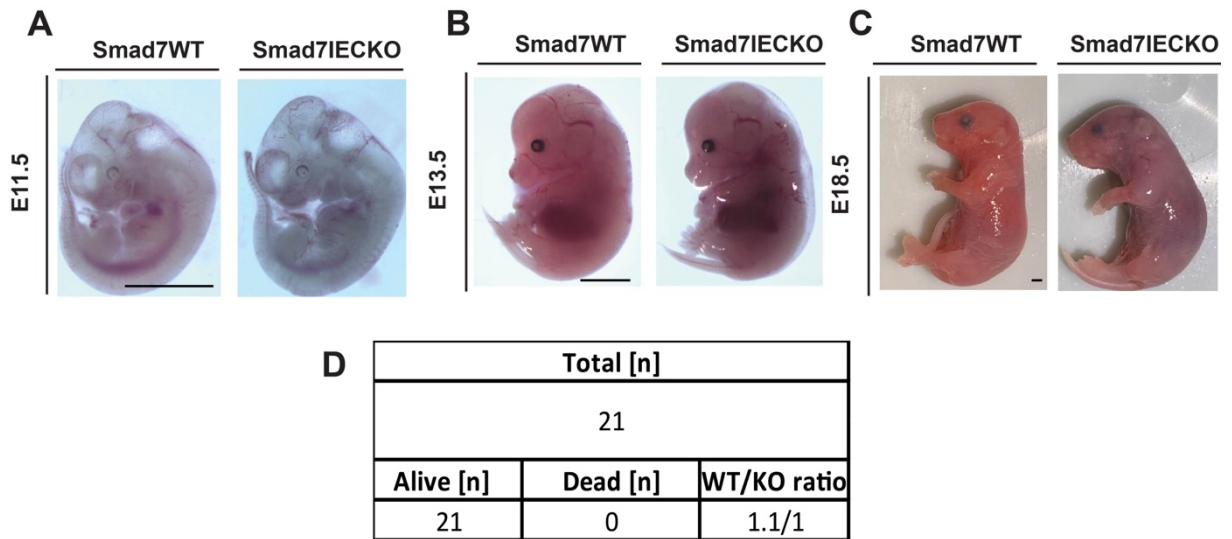
Figure 7: Embryonic deletion of endothelial Smad7 does not exhibit a macroscopic phenotype.
Representative images of E11.5 (A), E13.5 (B) and E18.5 (C) WT and Smad7IECKO embryos. (D) Table depicting lethality and WT/KO ratio of surviving mice after Tamoxifen administration. n=21 independent samples were used per experiment. Scale Bar: 1mm.

3.1.5 Embryonic deletion of Smad6 and Smad7 leads to lethality with high penetrance due to hemorrhages and uterine inflammation

Lastly, I collected embryos after endothelial deletion of Smad6 and Smad7 in Smad6/7IECKO mice at E11.5 (Figure 8A) E13.5 (Figure 8B) and E18.5 (Figure 8C). At each stage nearly all embryos appeared to be fully reabsorbed within the uterine horns. Only 2 mutant embryos survived until E13.5 but appeared to be developmentally delayed with widespread hemorrhages in the neck and lower body region. Mothers displayed pronounced uterine inflammation (data not shown) and no embryos survived past E13.5 due to complete abortion of pregnancy (Figure 8B). Out of 21 collected embryos, only 4 survived until E11.5 and 2 until E13.5 with severe developmental delay and 15 non-viable during collection indicating lethality with high penetrance (>70%) of Smad6/7IECKO embryos (Figure 8D).
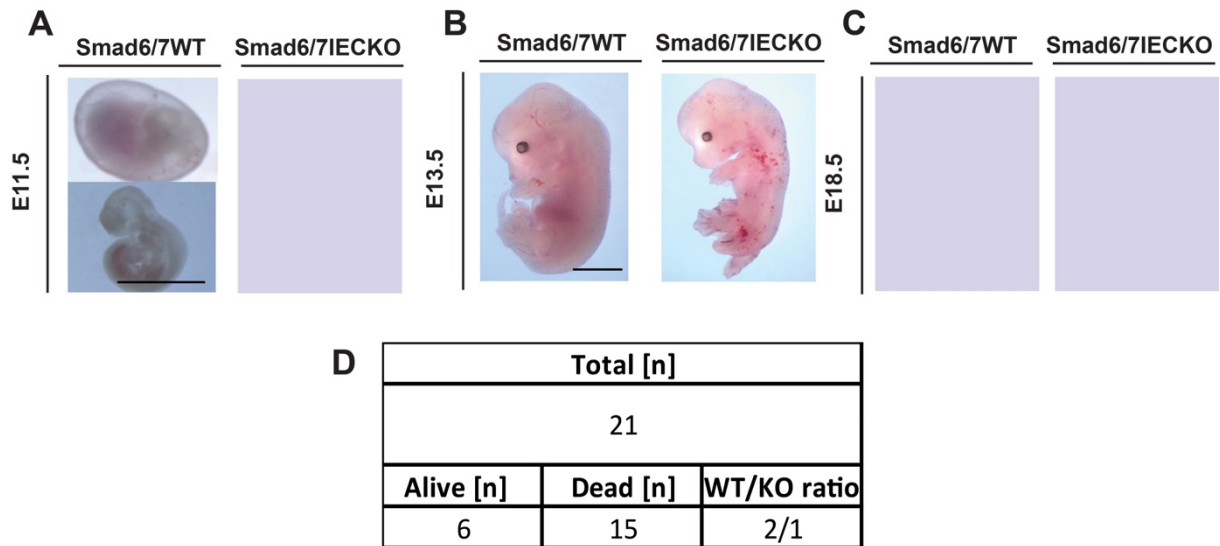
Figure 8: Embryonic deletion of endothelial Smad6 and 7.
Representative images of E11.5 (A), E13.5 (B) and E18.5 (C) WT and Smad6/7IECKO embryos. (D) Table depicting lethality and WT/KO ratio of surviving mice after Tamoxifen administration. n=21 independent samples were used per experiment. Scale Bar: 1mm.

3.2 Endothelial iSMAD in postnatal development

Developmental Smad6 was previously shown to play a role in sprouting angiogenesis in the developing retinal vasculature. In a Smad6 global deletion model, Smad6-/- mutant pups showed increased vessel sprouting and branching indicating an anti-angiogenic effect of Smad6 in the mouse retina (180). To test whether postnatal deletion of endothelial-specific Smad6 would recapitulate the reported effect of global Smad6 deletion, and to analyze the role of iSMADs in retinal vascularization, I treated Smad6IECKO, Smad7IECKO and Smad6/7IECKO mice with three doses of 50ug 4-Hydroxytamoxifen at P2, P3 and P5 to induce deletion and collected retinas at P6-8 (Figure 9A). Eyes were harvested, and retinas were isolated by removing the cornea and peeling of the sclera followed by removal of the lens and choroid vessels. Retinas were then cut at four opposite sides and mounted in a leaf-shaped flat mount (Figure 9B). Deletion efficiency of iSMAD were confirmed in FACS sorted lung EC of iSMAD IECKO mice (Figure 9C).

To observe if postnatal deletion of endothelial iSMAD would lead to a delay in postnatal development of mutant mice, I analyzed body weight (BW) and organ-to-body weight ratio at P6-8. With exception of a slight decrease in Smad6IECKO liver weight, no changes in BW or organ-to-body weight ratio were observed (data not shown).
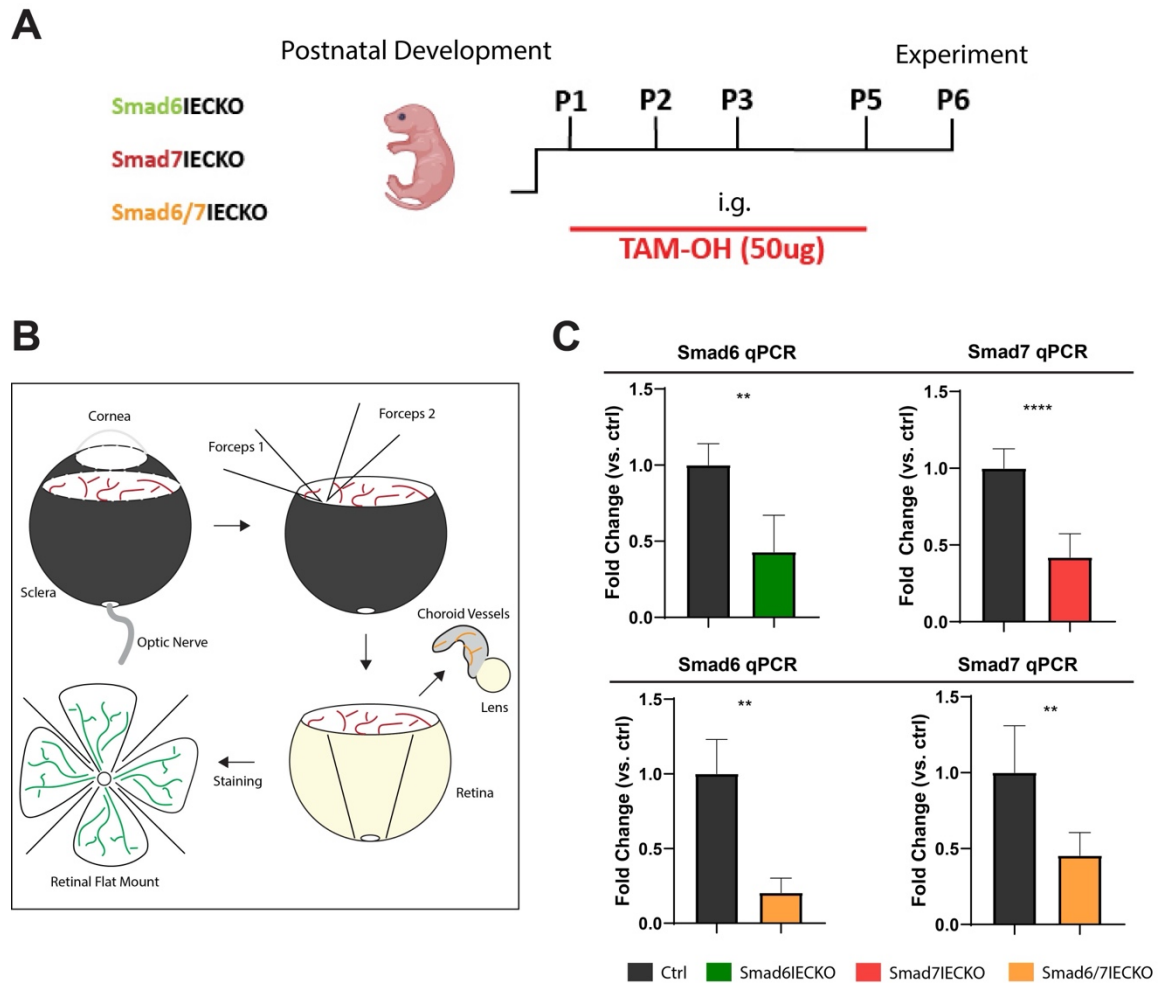
Figure 9: Postnatal induction of iSMAD KO and retina isolation.
(A) Schematic representation of knockout induction. Endothelial iSMAD were deleted by treating newborn pups with 4 doses of 50ug Hydroxytamoxifen according to the depicted treatment schedule. (B) Schematic depiction of retina isolation. (C) Gene expression analysis of *Smad6* and *Smad7* in sorted Smad6IECKO (green, n=6), Smad7IECKO (red, n=12) and Smad6/7IECKO (yellow, n=5-6) Lung EC. Data are shown as mean ± SD. **P<0.01, ***P<0.001, ****P<0.0001. Mann-Whitney *U* test.

3.2.1 Postnatal loss of Smad7 but not Smad6 affects retinal vascularization

The isolated retinas were stained with isolectin (Figure 10A) and analyzed for vessel area, density, outgrowth and branching (Figure 10B-E). Smad6IECKO retinas appeared normal with radial expansion, vascular density or branching not compromised. When analyzing Smad7IECKO retinal vascularization after postnatal deletion of endothelial Smad7, I found a reduction in vessel- and vascularized area compared to WT littermate controls (Figure 11A-B). Radial expansion from the optic nerve to the periphery was decreased as indicated by vessel outgrowth (Figure 11C). In-depth analysis revealed unaffected vessel branching with a trend towards reduced density (Figure 11D-E). Double deletion of endothelial Smad6 and Smad7 similarly led to a reduction in vessel- and

vascularized area in Smad6/7IECKO mice compared to WT littermate controls (Figure 12A-B) with reduced vessel outgrowth (Figure 12C). Vascular density and branching appeared unaffected (Figure 12D-E).
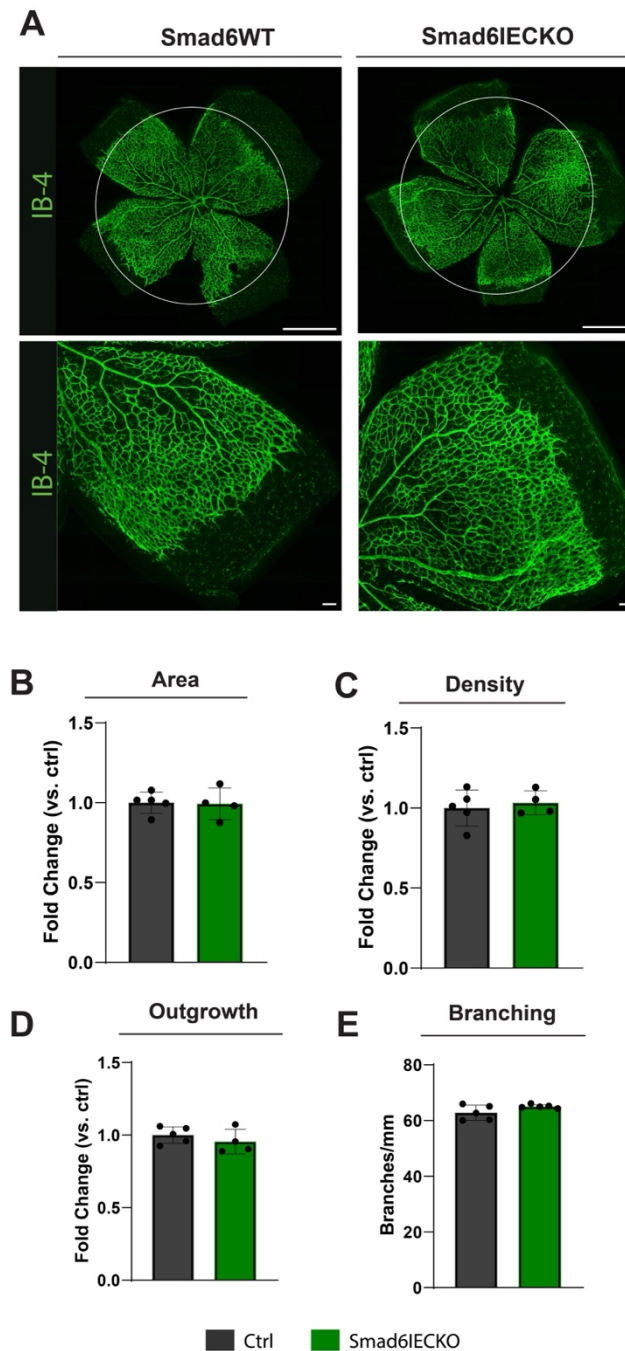
Figure 10: Deletion of endothelial Smad6 does not affect retinal angiogenesis.
(A) Representative images of the total retinal vasculature and the sprouting front stained with IB-4 in WT and Smad6IECKO retinas. (B) Quantifications of retinal vessel area (C), density vessel outgrowth (D), branching (E). Scale bar: 500µm and 50µm. Data are shown as mean ± SD. n = 4-5. Data are not significant if not indicated otherwise. Mann-Whitney *U* test.
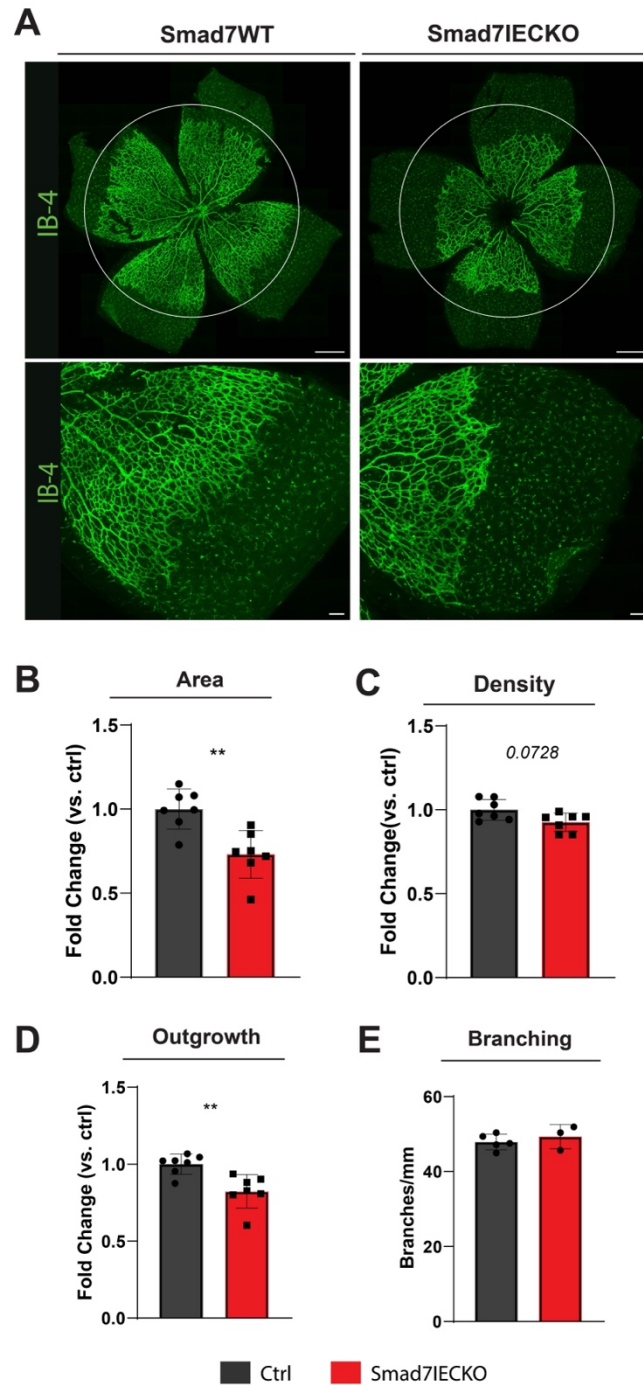
Figure 11: Deletion of endothelial Smad7 inhibits retinal angiogenesis.
(A) Representative images of the total retinal vasculature and the sprouting front stained with IB-4 in WT and Smad7IECKO retinas. (B) Quantifications of retinal vessel area (C), density vessel outgrowth (D), branching (E). Scale bar: 500µm and 50µm. Data are shown as mean ± SD. n = 7. **P<0.01. Data are not significant if not indicated otherwise. Mann-Whitney *U* test.
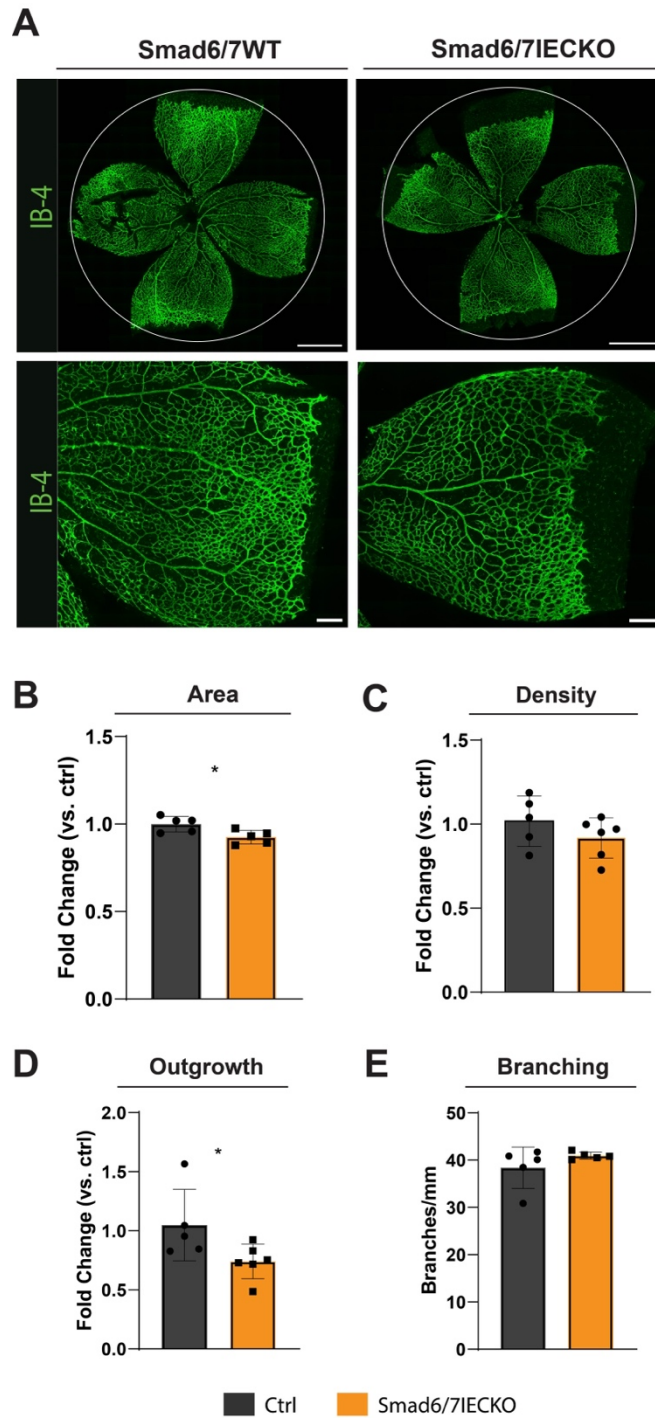
Figure 12: Deletion of endothelial Smad6/7 phenocopies deletion of endothelial Smad7.
(A) Representative images of the total retinal vasculature and the sprouting front stained with IB-4 in WT and Smad7IECKO retinas. (B) Quantifications of retinal vessel area (C), density vessel outgrowth (D), branching (E). Scale bar: 500µm and 50µm. Data are shown as mean ± SD. n = 5. *P<0.05. Data are not significant if not indicated otherwise. Mann-Whitney *U* test.

3.2.2 Increased neovascularization during OIR in Smad6IECKO mice

Smad6 has been previously reported to regulate retinal angiogenesis with loss of global Smad6 leading to hyperproliferation in retinal vessels (180). Since these results could not be reproduced in Smad6IECKO mice, I tested jointly with Ioanna Michou whether pathological neovascularization during OIR would be affected by loss of endothelial Smad6 (Figure 13A, B). Avascular area (Figure 13B, C) and neovascular area (Figure 13B, D) appeared similar between Smad6WT and Smad6IECKO pups, but the extent of neovascularization appeared more severe in Smad6IECKO than Smad6WT pups (Figure 13E). Smad6IECKO showed NV tuft formation in all pups with a higher proportion of extensive tufts invading into the deeper retinal layers (Figure 13B, E).
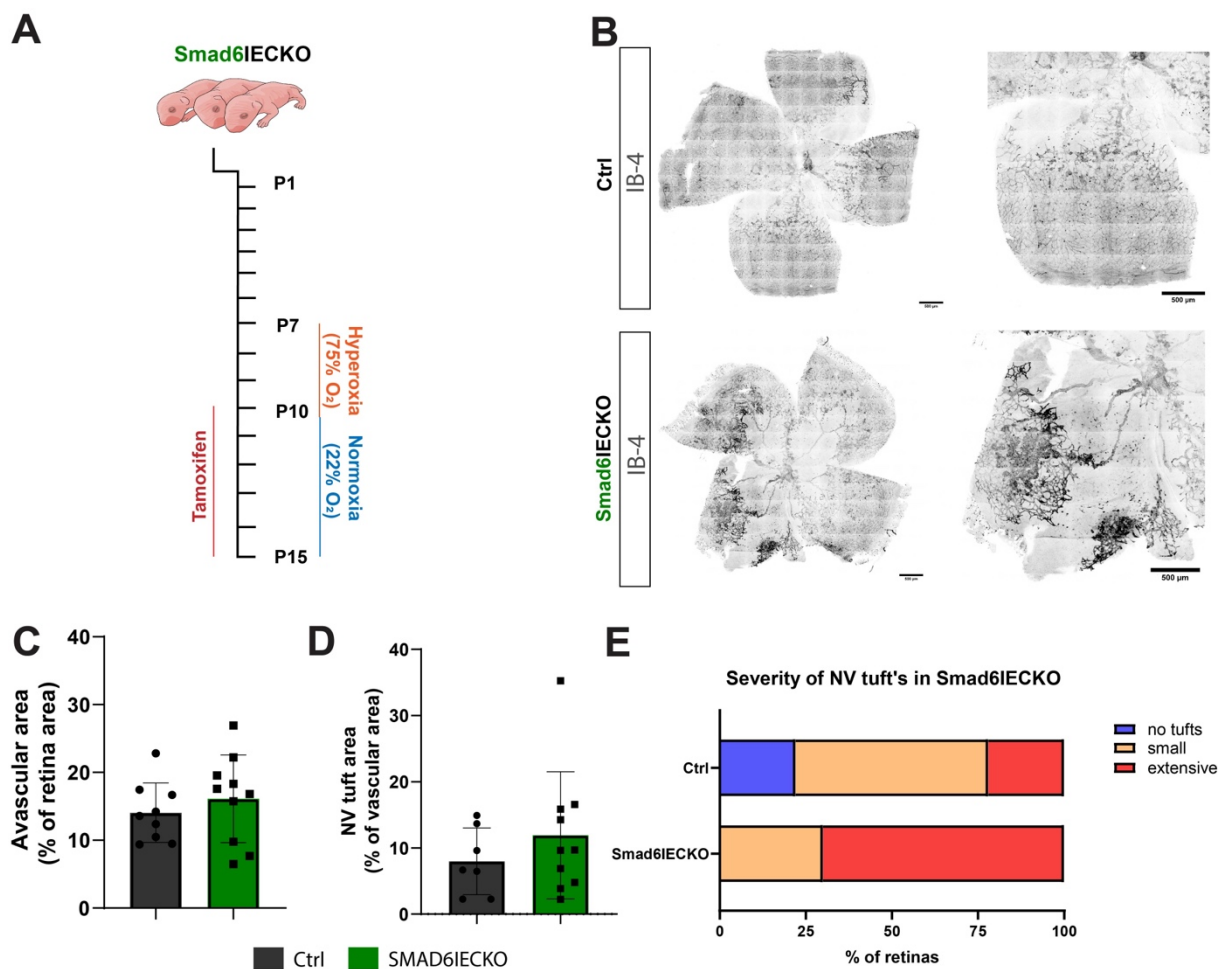
Figure 13: Deletion of Smad6 during pathological neovascularization leads to severe tuft formation.
(A) Schematic representation for induction of endothelial cell specific knockout of Smad6 during pathological neovascularization in OIR model. (B) Representative images of Ctrl (upper) and Smad6IECKO (lower) P15 retinas, after three days hyperoxia and five days of normoxia stained by IB-4. Avascular area marked in blue. Areas marked within a red circle indicate the formation of tufts. (C) Quantification of avascular area in respect to the total retinal area of Ctrl and Smad6IECKO pups. (D) Quantification of NV tuft area in respect to total vascular area in retinas of Ctrl and Smad6IECKO pups. (E) Stacked bar graph depicting the severity of tufts in retinas of Ctrl and Smad6IECKO pups. Scale bar: 500µ. Data are shown as mean ± SD. n=9. Data are not significant if not indicated otherwise. Mann-Whitney *U* test. Data produced jointly with Ioanna Michou.

3.2.3 Knockdown of endothelial SMAD7 but not SMAD6 decreases endothelial sprouting of HUVEC

Radial expansion of blood vessels in the postnatal retina was reduced after endothelial deletion of Smad7 but not Smad6. To test whether the observed effect is caused by impaired endothelial cell sprouting, I performed a sprouting assay using HUVEC. Before performing the assay, *SMAD6*, *SMAD7* and *SMAD6* and *7* were downregulated in EC using two independent shRNA prior to spheroid formation and embedded the KD-spheroids into collagen gels which were fixed 24h after stimulation (Figure 14A-C). I determined the number of sprouts per spheroid and average sprout length (Figure 14D-I). SMAD7KD spheroids showed a decrease in sprout number and sprout length (Figure 14E and H) and SMAD6/7KD spheroids showed a decrease in sprout length (Figure 14I).
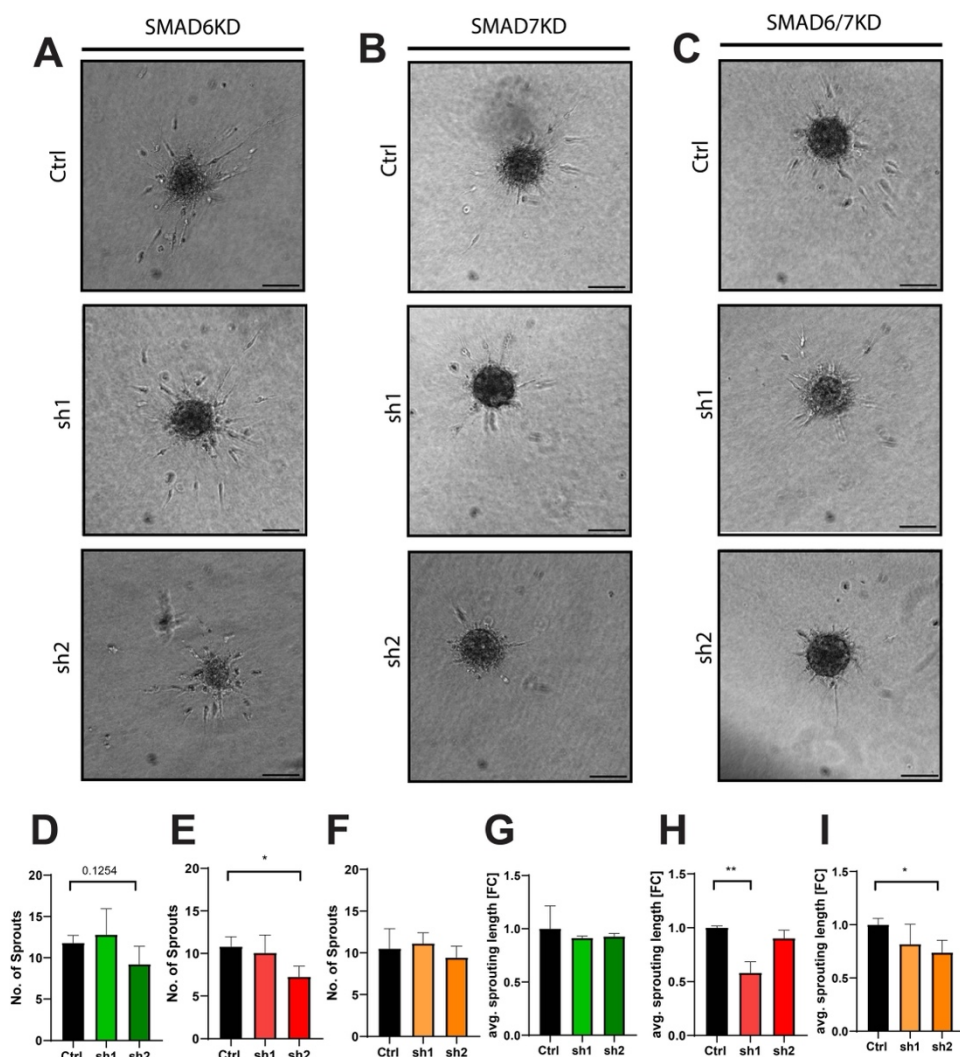
Figure 14: SMAD7KD limits endothelial cell sprouting.
(A-C) Representative bright field (BF) images of in vitro sprouting assay using HUVEC shCtrl or HUVEC and shSMAD6, shSMAD7 and shSMAD6 + shSMAD7, respectively. (D-F) Quantification of average sprout length (G-I) Quantification of No. of sprouts. Data are shown as mean ± SD. n = 3. *P<0.05. **P<0.01. Scale Bar: 200µm. Data are not significant if not indicated otherwise. Student's *t*-test.

3.3   Endothelial iSmad in acquisition of vascular quiescence

3.3.1   Disruption of SMAD6 but not SMAD7 leads to increased EC proliferation in a vascular spheroid model

To study how loss of iSMAD expression affects endothelial quiescence *in vitro*, I performed jointly with Niklas Buckwalter an in vitro spheroid co-culture model. Single-cell sequencing of WT vascular spheroids by Niklas Buckwalter previously confirmed increased iSMAD expression in 3D vs. 2D co-culture (Buckwalter *et al.*, unpublished). SMAD6-, SMAD7- and SMAD6/7KD HUVEC and brain pericytes (B-PC) were co-cultured in a hanging drop leading to the formation of EC-PC vascular spheroids with an inside-out organization (Figure 15A). HUVEC form a monolayer on the outside of the spheroids and B-PC assemble in the core of the spheroid. KD efficiency was determined by qRT-PCR (Figure 15B). To determine the extent of EC proliferation after iSMAD KD, EdU was added to a final concentration of 0.01mM to the medium prior to spheroid assembly. The EdU incorporation assay yielded increased EC proliferation in SMAD6KD and SMAD6/7KD spheroids but not SMAD7KD spheroids (Figure 15C).
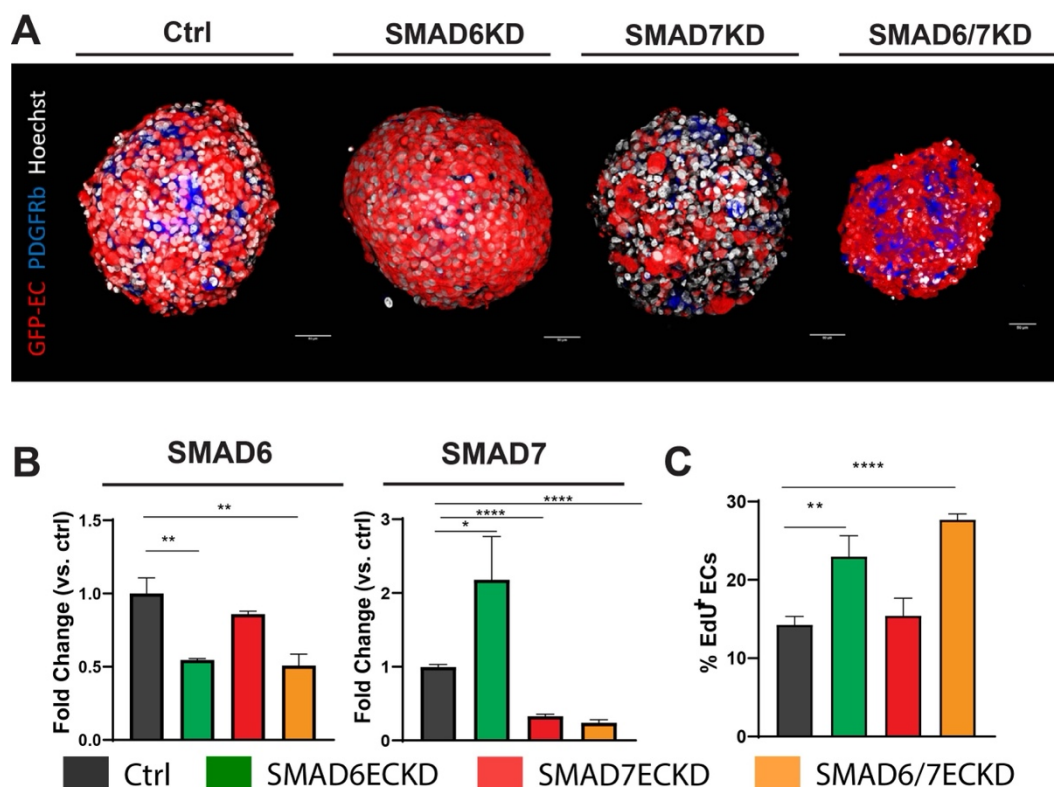
Figure 15: iSMAD KD in 3D vascular co-culture spheroids differentially affect spheroid formation
(A) Representative confocal images of iSMAD KD-HUVEC (GFP, green) and B-PC (PDGFRb, blue) vascular co-culture spheroids. Nuclei stained for Hoechst (white). (B) Expression of iSMAD in SMAD6ECKD (green), SMAD7ECKD (red) and SMAD6/7ECKD (yellow). (C) FACS analysis of BrdU

treated EC in vascular co-culture spheroids. Scale Bar: 50um. Data are shown as mean ± SD. n=3. *P<0.05. **P<0.01, ***P<0.001, ****P<0.001. Student's *t*-test. Data produced jointly with Niklas Buckwalter.

3.3.2   Proteomic profiling of *in vitro* endothelial quiescence

To determine proteomic changes associated with endothelial identity and behavior after loss of iSMADs during endothelial quiescence, *in vitro* proteomic profiling of EC after transition from a proliferating to a quiescent EC state was performed in collaboration with the Department of Systems Biology and Signaltransduction of the DKFZ. I downregulated *SMAD6*, *SMAD7* or *SMAD6* and *7* in HUVEC using shRNA prior to endothelial monolayer formation and collected the protein after monolayer formation. Mass spectrometry (MS) was performed in the Department of Systems Biology and Signaltransduction. Sample preparation for MS was performed jointly with Simone Clas and Yannik Dieter. In total 4598 proteins were measured by Dr. Barbara Helm and 4203 proteins with at least 70% quantification rate in two or more conditions were retained (Figure 16A). Plotting the most significantly expressed proteins from SMAD6KD vs. WT (Figure 16B), SMAD7KD vs. WT (Figure 16C) and SMAD6/7KD vs. WT (Figure 16D) revealed distinct proteomic signatures of HUVEC in all three mutant conditions. The top 100 proteins were used as input for further protein enrichment and ontology analysis (Figure 17). SMAD6KD HUVEC displayed elevated metabolic stress as shown by the depletion of proteins related to oxidative phosphorylation (Figure 17A) and the enrichment of terms related to mitochondrial dysfunction (Figure 17B). SMAD7KD HUVEC acquire a mesenchymal proteomic profile with increased deposition of extracellular matrix components as depicted by enrichment of proteins in the epithelial-to-mesenchymal transition term (Figure 17C), extracellular matrix components (Figure 17D) and cytoskeleton (data not shown). SMAD6/7KD lead to the effects observed in SMAD6KD and SMAD7KD, respectively. SMAD6/7KD HUVEC display elevated metabolic stress (Figure 17E) as well as increased deposition of extracellular matrix components (Figure 17F).
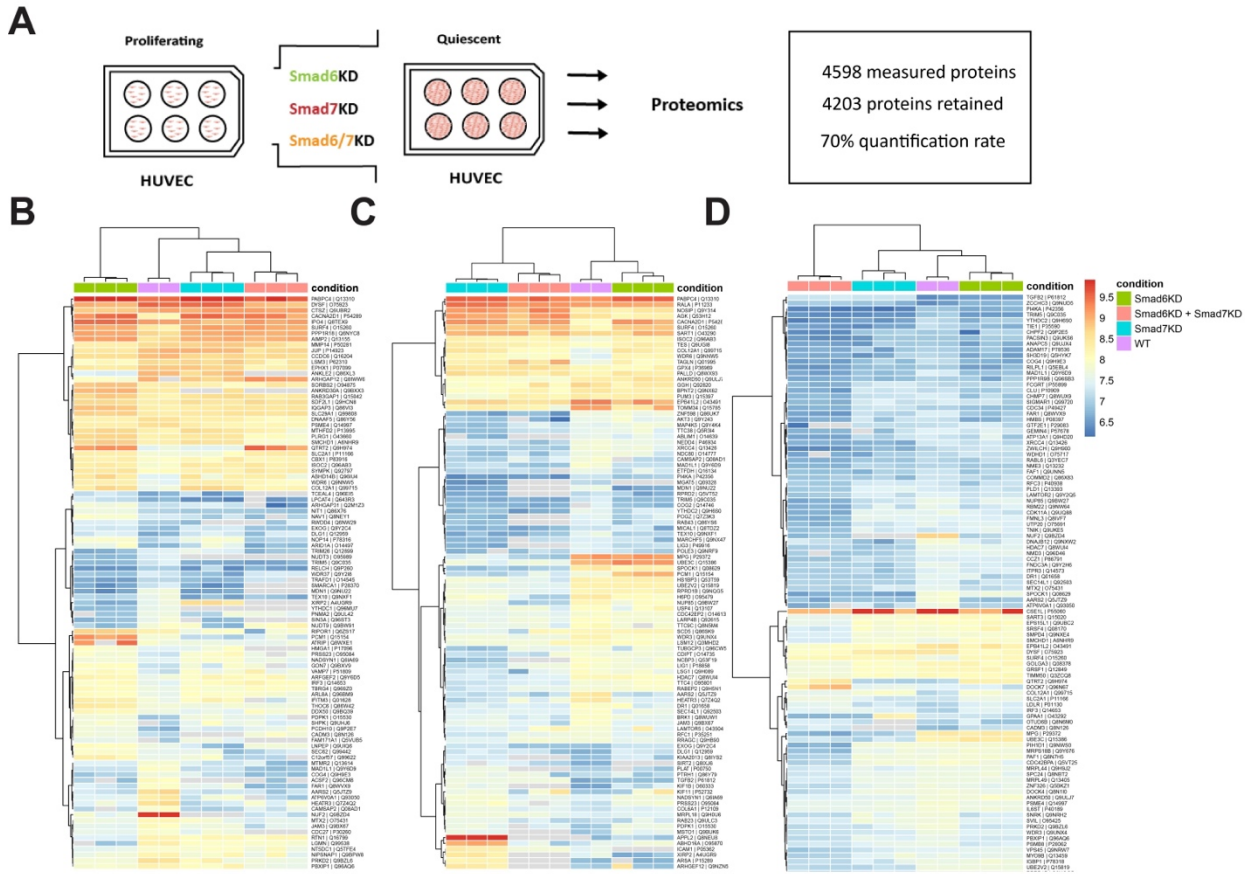
Figure 16: Proteomic profiling of WT and SMAD6-, SMAD7- and SMAD6/7KD HUVEC.
(A) Schematic depiction of experimental setup. (B-D) Heatmap of top 100 most significantly expressed proteins from SMAD6KD vs. WT (B), SMAD7KD vs. WT (C) and SMAD6/7KD vs. WT (D). n=3. Data produced jointly with Dr. Barbara Helm, Simone Clas and Yannik Dieter. Cell culture, lentiviral transfection and protein isolation was performed by myself. Sample preparation for mass spectrometry was performed by Simone Clas, Yannik Dieter and me. LC-MS/MS measurements performed by Dr. Barbara Helm. Computational work performed by Genevia Technologies.

Smad6KD vs. WT
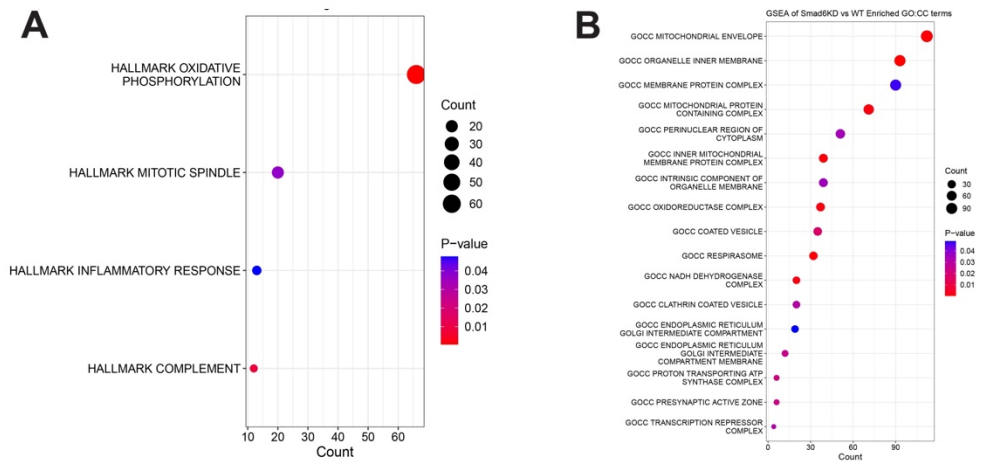
Smad7KD vs. WT
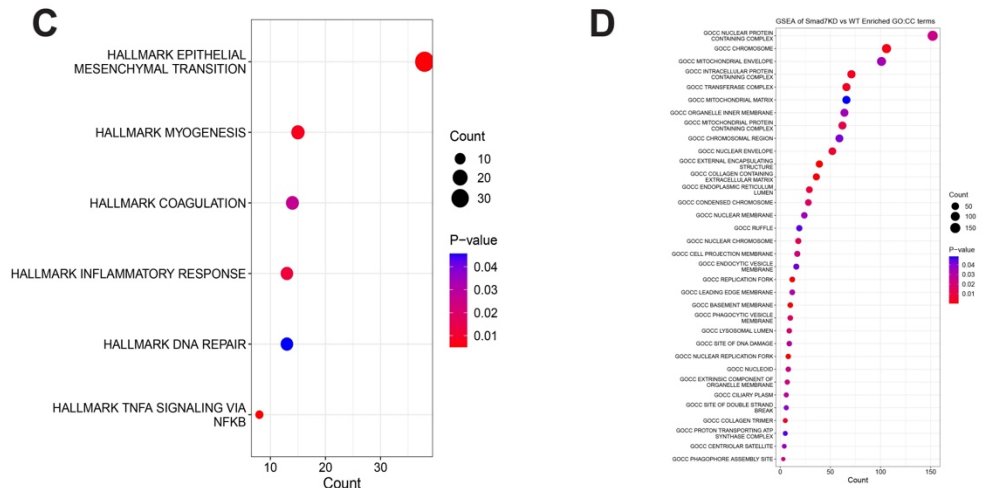
Smad6/7KD vs. WT
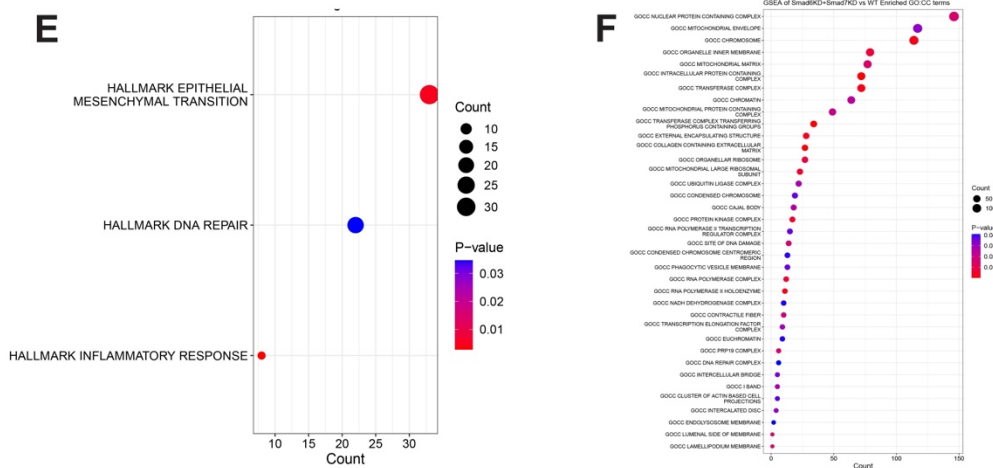
Figure 17: Enrichment and ontology analysis of top 100 most significantly expressed proteins.
(A) Dotplot of HALLMARK_TERMS in SMAD6KD vs. WT. (B) Dotplot of GO: Cellular component analysis in SMAD6KD vs. WT. (C) Dotplot of HALLMARK_TERMS in SMAD7KD vs. WT. (D) Dotplot of GO: Cellular omponent analysis in SMAD7KD vs. WT. (E) Dotplot of HALLMARK_TERMS in SMAD6/7KD vs. WT. (F) Dotplot of GO: Cellular component analysis in SMAD6/7KD vs. WT. Data produced jointly with Dr. Barbara Helm, Simone Clas and Yannik Dieter. Cell culture, lentiviral

transfection and protein isolation was performed by myself. Sample preparation was performed by Simone Clas, Yannik Dieter and me. LC-MS/MS measurements performed by Dr. Barbara Helm. Computational work performed by Genevia Technologies.

3.3.3 Transcriptomic profiling of *in vivo* vascular quiescence

Next, the transcriptomic outcome of iSMAD deletion during establishment of *in vivo* vascular quiescence was assessed. I deleted endothelial Smad6, Smad7 and Smad6/7 postnatally according to the previously established protocol (Figure 9A). Mutant mice were kept until adult age (8-12 weeks) at which organs have fully developed and vascular quiescence is established. I isolated lung and liver EC by FACS, prototypically representing continuous and sinusoidal endothelium, from all mutant mice (Figure 18A). I gated cells according to FCS-A and SSC-A to exclude cell debris, and to SSC-W and SSC-A to remove doublets. To exclude dead cells, FxCycle was used. Lung EC were sorted for CD45-TER119-LYVE1-PDPN-CD31+ and liver EC for CD45-TER119-PDPN-CD31+CD146+ (Figure 18B). Deletion efficiency of iSMAD was confirmed by RT-qPCR in mutant mice (Figure 18C). RNA-sequencing was performed by the Genomics and Proteomics Core Faciltiy (GPCF) of the DKFZ. Single deletion of Smad6 and Smad7 lead to few differentially expressed genes (DEG) in Lung EC (<100 DEG) and Liver EC (<200 DEG) whilst double deletion of iSMAD presented in 5-10-fold higher numbers of significantly up- and downregulated genes compared to WT (Figure 18D). Overlap analysis of DEG in sorted lung EC (Figure 19A) and liver EC (Figure 19B) unveiled single commonly regulated genes in Smad6IECKO and Smad7IECKO mice and no commonly regulated genes between all three mutant mouse lines.
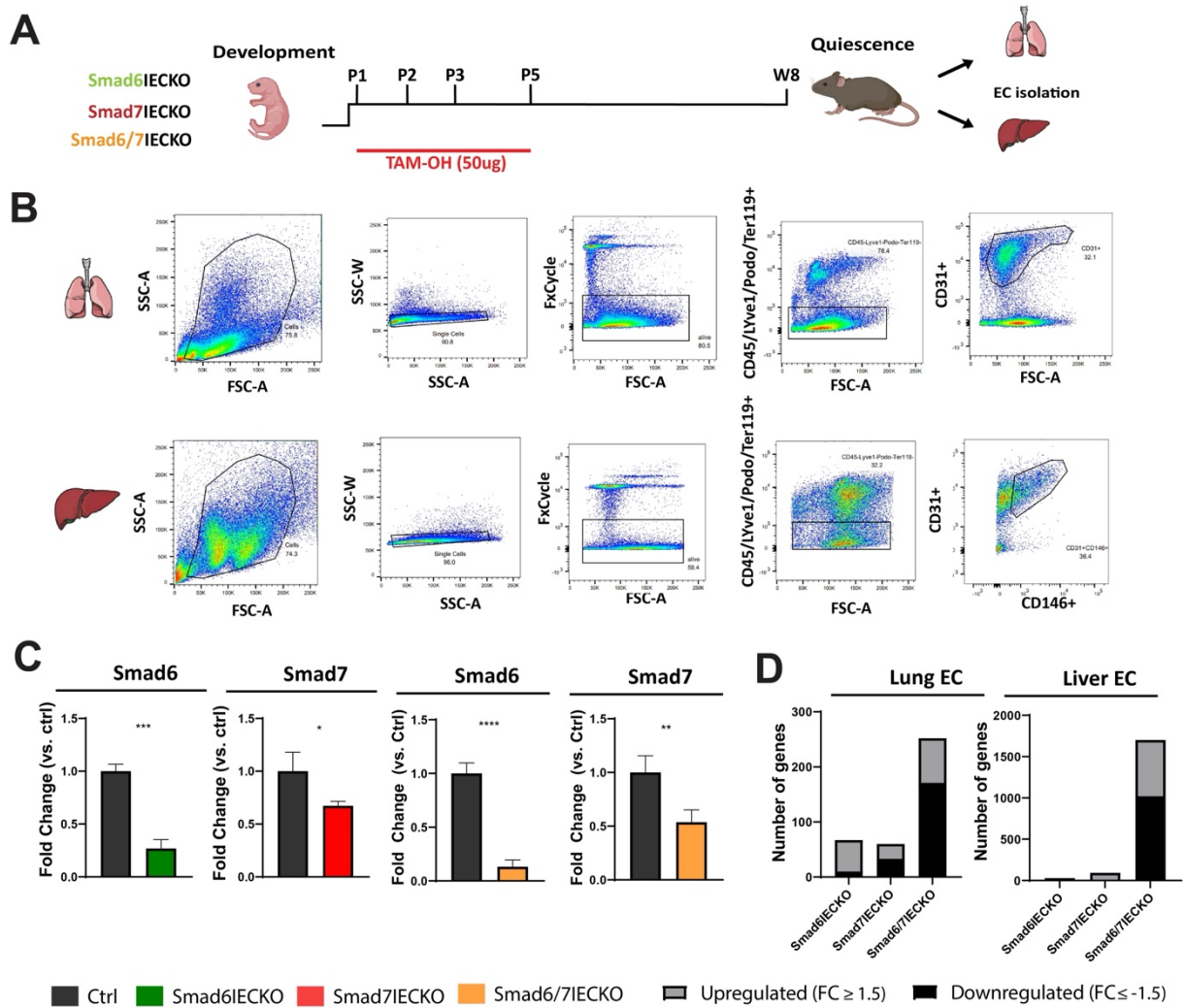
Figure 18: Transcriptomic profiling strategy of iSMAD loss in lung and liver EC during transition into quiescence.

(A) Schematic representation of knockout induction. Endothelial iSMAD were deleted by treating newborn pups with 4 doses of 50ug Hydroxytamoxifen and kept until 8-weeks. (B) FACS strategy for EC isolation from Lung and Liver. (C) Gene expression analysis of Smad6 and Smad7 in sorted Smad6IECKO (green), Smad7IECKO (red) and Smad6/7IECKO (yellow) Lung EC. (D) Bar graph illustrating the number of significantly upregulated (↑) and downregulated (↓) genes in Lung EC (LEC) and Liver EC (LSEC) Smad6IECKO (LEC: 57 ↑, 10 ↓; LSEC: 26 ↑, 3 ↓), Smad7IECKO (LEC: 27 ↑, 33 ↓; LSEC: 84 ↑, 9 ↓), and Smad6/7IECKO (LEC: 81 ↑, 171 ↓; LSEC: 681 ↑, 1020 ↓) as compared with WT. Data are shown as mean ± SD. n=3. *P<0.05. **P<0.01, ***P<0.001. Mann-Whitney *U* test.

A

Lung WT vs KO

DE genes at abs. L2FC > 0.58 & padj < 0.05

B

Liver WT vs KO

DE genes at abs. L2FC > 0.58 & padj < 0.05
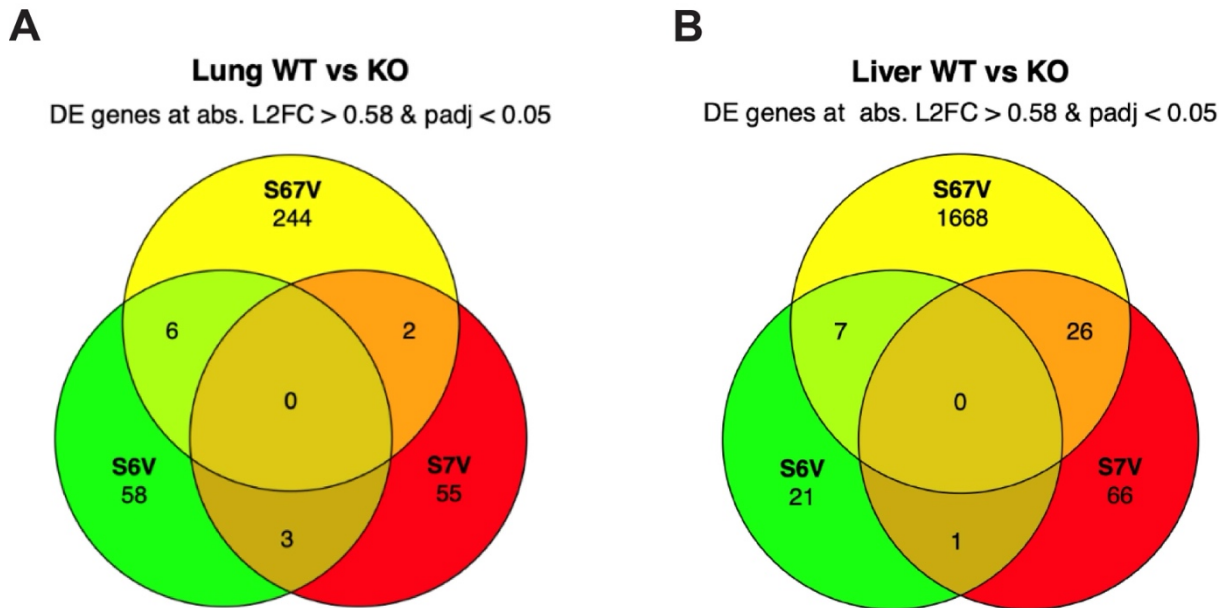
Figure 19: Venn diagram of Smad6-, Smad7- and Smad6/7-deficient lung and liver EC.
(A) Overlap analysis of Lung EC sorted from Smad6-, Smad7- and Smad6/7IECKO mice. (B) Overlap analysis of Liver EC sorted from Smad6-, Smad7- and Smad6/7IECKO mice. Computational work performed by Genevia Technologies.

3.3.3.1   Smad6- and Smad7- deletion has opposite effects on lung EC activation

Endothelial deletion of Smad6 yielded few differentially regulated genes with overall transcriptional activation of pro-angiogenic factors including *ACVR1*, *ID1*, *ID2*, *ID3*, *Junb* and compensatory activation of TGFβ response repressors including *Smad7*, *Nog*, *Ski*, and *Smurf2* in lung EC (Figure 20A). Gene set enrichment analysis (GSEA) of differently expressed genes (DEG) showed a significant enrichment of members and downstream targets of the TGF beta superfamily (Figure 20B). Gene Ontology (GO) analysis of biological processes yielded an increase in frequency, rate and extent of general system processes as well as kinase signaling within lung EC indicating increased cell activity (Figure 20C). In contrast endothelial deletion of Smad7 led to a down-regulation of genes related to endothelial cell activation (*Pfkfb3*, *Nfkbia*, *Icam1*, *Icam2*, *Vegfa*, *Bmp2* and *Klf4*) (Figure 21A) with a depletion of gene sets related to inflammatory response (Figure 21B) and an increase in negative regulation of cell proliferation, activity and adhesion according to GO analysis (Figure 21C). The transcriptomic profile of EC deleted for Smad6 and Smad7 displayed characteristics of single endothelial Smad6 and single endothelial Smad7 deletion. In particular, double iSMAD deletion led to a down-regulation of genes related to inflammatory activation (*Nfkbiz*, *Cxcl2*, *Klf4*, *Pfkfb3* and *Jag1*), down-regulation of angiogenic repressors (*Sema3e* and *Ptgs2*) and up-regulation of pro-angiogenic genes (*Acvr1*, *Sirt1*

and *Akt1*) (Figure 22A). Smad6/7-deficient lung EC showed a depletion of gene sets related to inflammatory response similar to Smad7-deficient lung EC (Figure 22B) and enrichment of biological processes including response to growth factors, growth stimulus and angiogenesis in line with Smad6-deficient lung EC (Figure 22C). Overall, double deletion of Smad6 and Smad7 in lung EC led to additive transcriptomic changes.
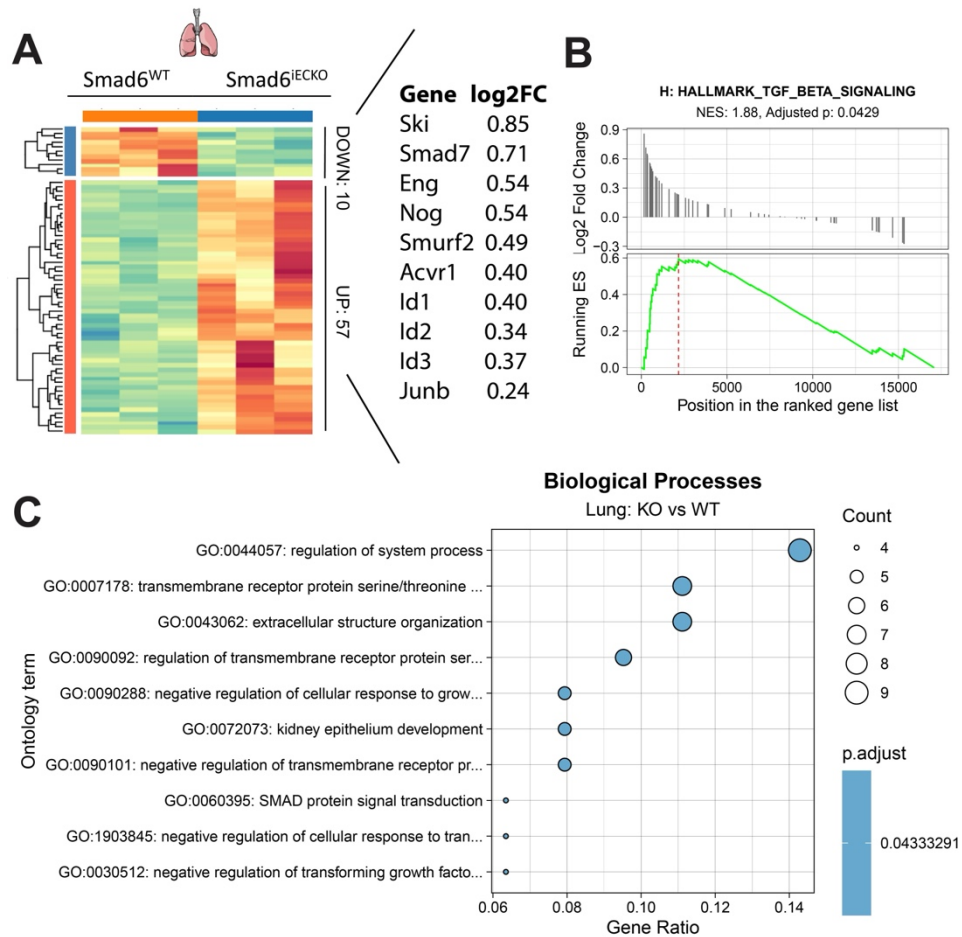
Figure 20: Gene expression analysis of WT vs. Smad6IECKO lung EC.
(A) Heat map of the gene expression profiling of FACS sorted Lung EC of WT and Smad6IECKO mice. List of upregulated genes (Smad6IECKO vs. WT) is shown on the right. (B) GSEA Plot for HALLMARK_TGF_BETA_SIGNALING (C) GO analysis of biological processes in Smad6-deficient Lung EC. Computational work performed by Genevia Technologies.
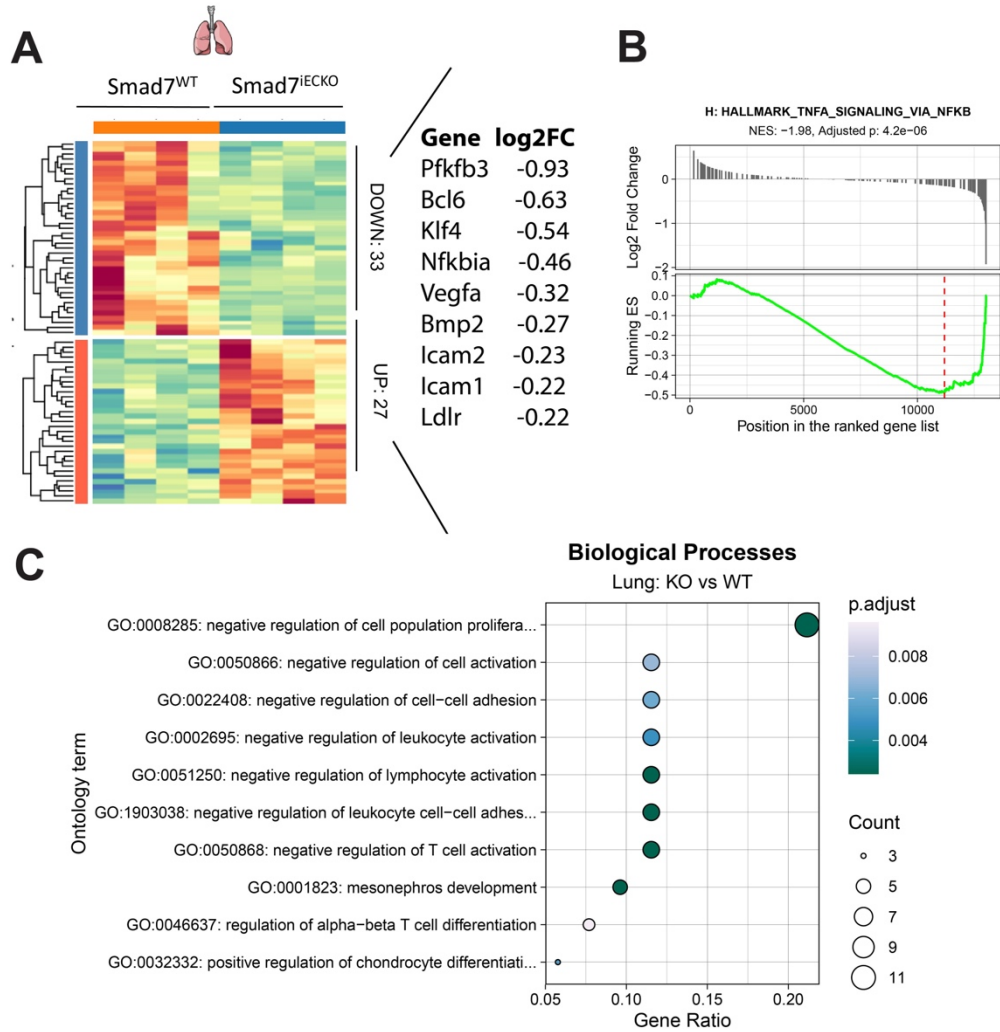
Figure 21: Gene expression analysis of WT vs. Smad7IECKO lung EC.
(A) Heat map of the gene expression profiling of FACS sorted Lung EC of WT and Smad7IECKO mice. List of down-regulated genes (Smad6IECKO vs. WT) is shown on the right. (B) GSEA Plot for for HALLMARK_TNFA_SIGNALLING, HALLMARK_E2F_TARGETS and HALLMARK_G2M_CHECKPOINTS. (C) GO analysis of biological processes in Smad7-deficient Lung EC. Computational work performed by Genevia Technologies.
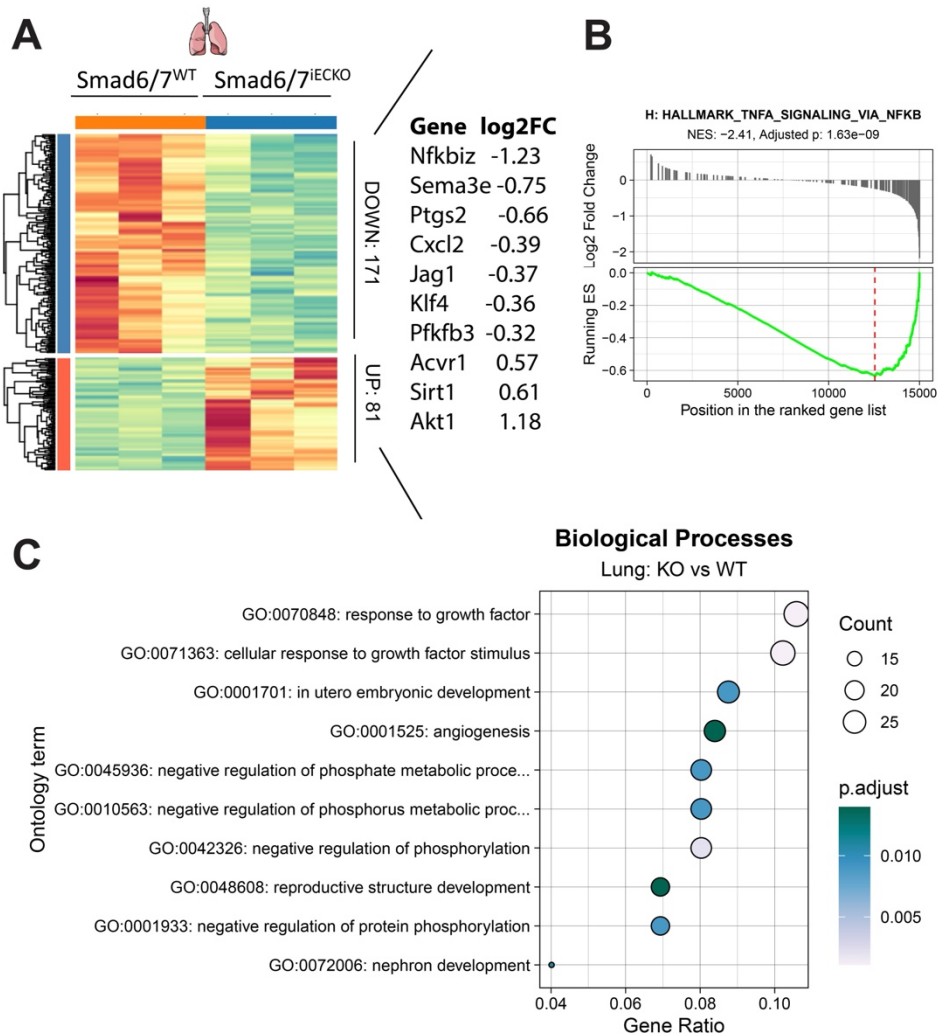
Figure 22: Gene expression analysis of WT vs. Smad6/7IECKO lung EC.
(A) Heat map of the gene expression profiling of FACS sorted Lung EC of WT and Smad6/7IECKO mice. List of up-regulated genes (Smad6/7IECKO vs. WT) is shown on the right. (B) GSEA Plot for HALLMARK_TNFA_SIGNALLING, HALLMARK_E2F_TARGETS and HALLMARK_G2M_CHECKPOINT (C) GO analysis of biological processes in Smad6/7-deficient Lung EC. Computational work performed by Genevia Technologies.

3.3.3.2 Smad6- and Smad7-deficient liver EC enrich mesenchymal transition genes whereas Smad6/7-deficient liver EC deplete mesenchymal genes

In line with the transcriptomic profiling of quiescent lung EC of adult mice after iSMAD deletion during postnatal development, transcriptomic changes due to single deletion of Smad6 and Smad7 in the sinusoidal liver endothelium were marginal. Smad6-deficient LSEC showed transcriptomic upregulation of genes related to collagen deposition (*Col3a1*, *Col4a4*, *Col4a5*, *Col6a1*, *Col6a2*, *Col6a3*, *Col6a5* and *Col18a1*) and basement membrane (*Lamb1*, *Lamc3* and *Fn1*) (Figure 23A). GSEA yielded an enrichment in hallmark gene sets related to mesenchymal transition (Figure 23B). Coinciding with

these findings, GO analysis of most significantly altered genes showed an enrichment in extracellular matrix components and collagen-containing extracellular matrix (Figure 23C). Similarly, Smad7-deficient LSEC showed transcriptomic upregulation of genes related to collagen deposition (*Col4a5*, *Col4a6*, *Col12a1*, *Col6a6*, *Col15a1*), basement membrane (*Postn*, *Lamb1*, *Fn1*) and activation of canonical TGFβ signaling (*Serpine1*) (Figure 24A). GSEA also yielded enrichment in hallmark gene sets related to mesenchymal transition (Figure 24B) and most significantly altered gene expression belonged to extracellular matrix components and the collagen-containing extracellular matrix (Figure 24C). In contrast, the inverse was true for LSEC deficient for both Smad6 and Smad7. Smad6/7-deficient LSEC showed overall transcriptomic downregulation of genes related to collagen deposition (Col4a5, Col6a3, Col8a1, Col10a1, Col14a1, Col10a1, Col16a1, Col28a1), basement membrane (Postn and Lamb3), mesenchymal marker (Tagln) and TGFβ signaling activation (Serpine1) (Figure 25A). GSEA showed significant depletion of hallmark gene sets related to mesenchymal transition (Figure 25B) and GO analysis of cellular components showed that downregulated genes belonged to the changes in external encapsulating structure organization, extracellular matrix components, cell-cell junctions and the collagen containing extracellular matrix (Figure 25C).
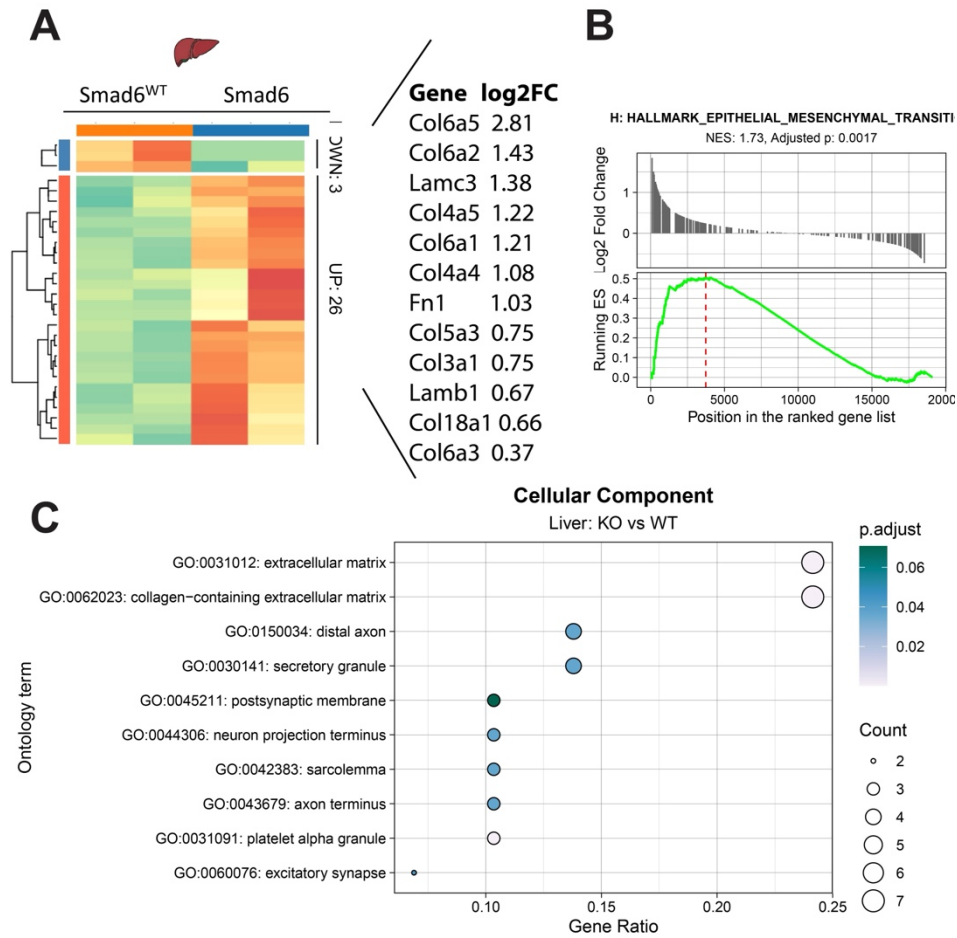
Figure 23: Gene expression analysis of WT vs. Smad6IECKO liver EC.
(A) Heat map of the gene expression profiling of FACS sorted Liver EC of WT and Smad6IECKO mice. List of upregulated genes (Smad6IECKO vs. WT) is shown on the right. (B) GSEA Plot for HALLMARK_EPITHELIAL_MESENCHYMAL_TRANSITION (C) GO analysis of cellular components in Smad6-deficient Liver EC. Computational work performed by Genevia Technologies.
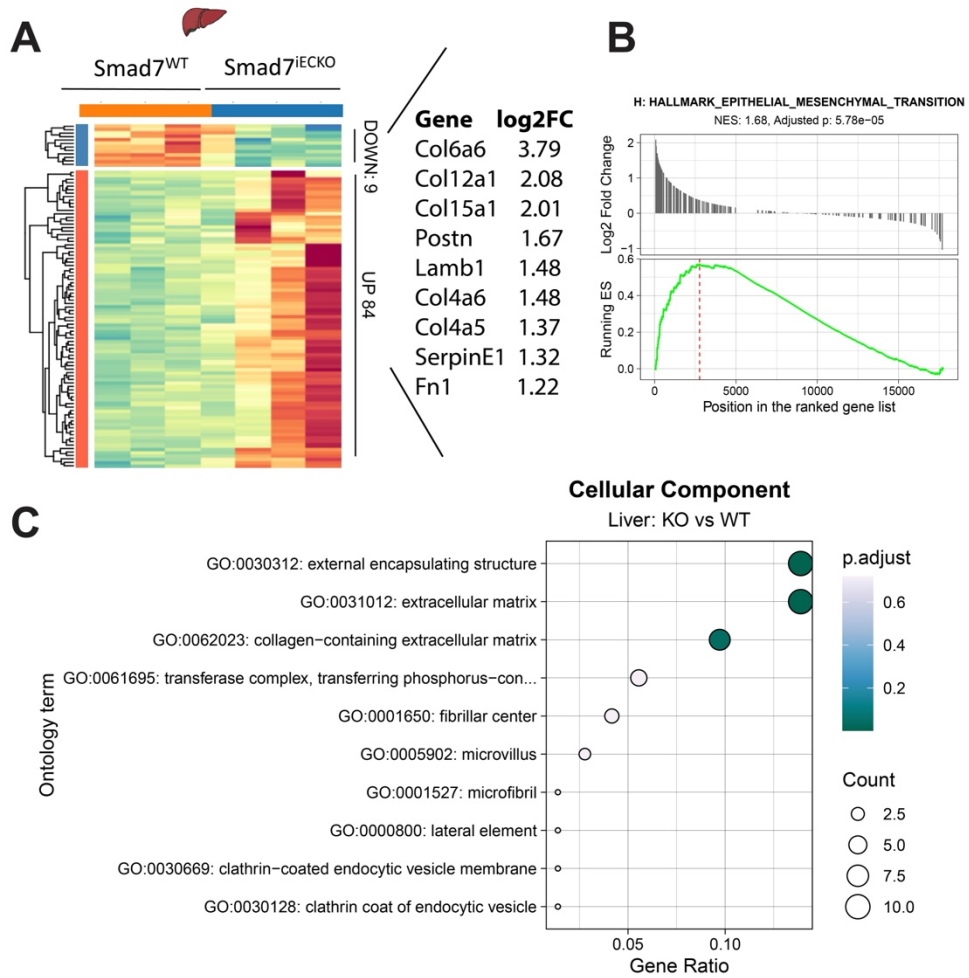
Figure 24: Gene expression analysis of WT vs. Smad7IECKO liver EC.
(A) Heat map of the gene expression profiling of FACS sorted Liver EC of WT and Smad7IECKO mice. List of upregulated genes (Smad7IECKO vs. WT) is shown on the right. (B) GSEA Plot for HALLMARK_EPITHELIAL_MESENCHYMAL_TRANSITION. (C) GO analysis of cellular components in Smad7-deficient Liver EC. Computational work performed by Genevia Technologies.
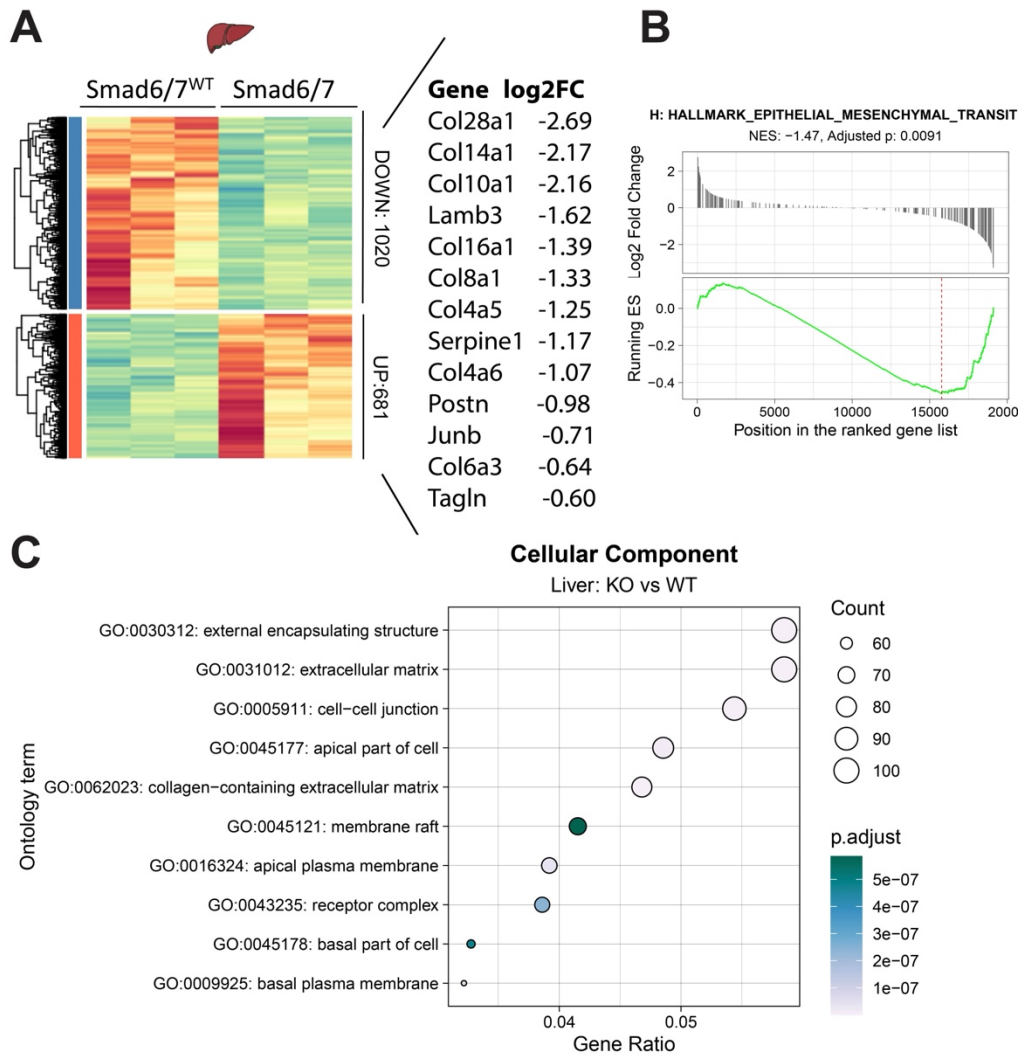
Figure 25: Gene expression analysis of WT vs. Smad6/7IECKO liver EC.
(A) Heat map of the gene expression profiling of FACS sorted Liver EC of WT and Smad7IECKO mice. List of upregulated down-regulated genes (Smad6/7IECKO vs. WT) is shown on the right. (B) GSEA Plot for HALLMARK_EPITHELIAL_MESENCHYMAL_TRANSITION. (C) GO analysis of cellular components in Smad6/7-deficient Liver EC. Computational work performed by Genevia Technologies.

3.3.4 No pathophysiological consequence of iSMAD deletion during acquisition of *in vivo* endothelial quiescence

Body weight of Smad6IECKO, and Smad7IECKO and Smad6/7IECKO mice was assessed 8 weeks post endothelial-specific gene deletion. Body weight of Smad6IECKO and Smad6/7IECKO mice remained similar to the control group (Figure 26A). Smad7IECKO mice appeared smaller at 8-10 weeks post deletion but the difference in body weight recovered when the KO was traced over a period of 52 weeks post deletion (Figure 26B). I analyzed organ-to-body weight ratio of liver, brain, kidneys, heart, and lung at 8 weeks post deletion and I found that it resembled the control group (Figure 26C). Organ

pathology was assessed by HE staining and organs appeared to be normal (data not shown). I further observed normal vascularization and pericyte coverage in mutant and control mouse lines (Figure 26D). Similarly, metabolic zonation of the liver and endothelial BM appeared unchanged (Figure 26E).
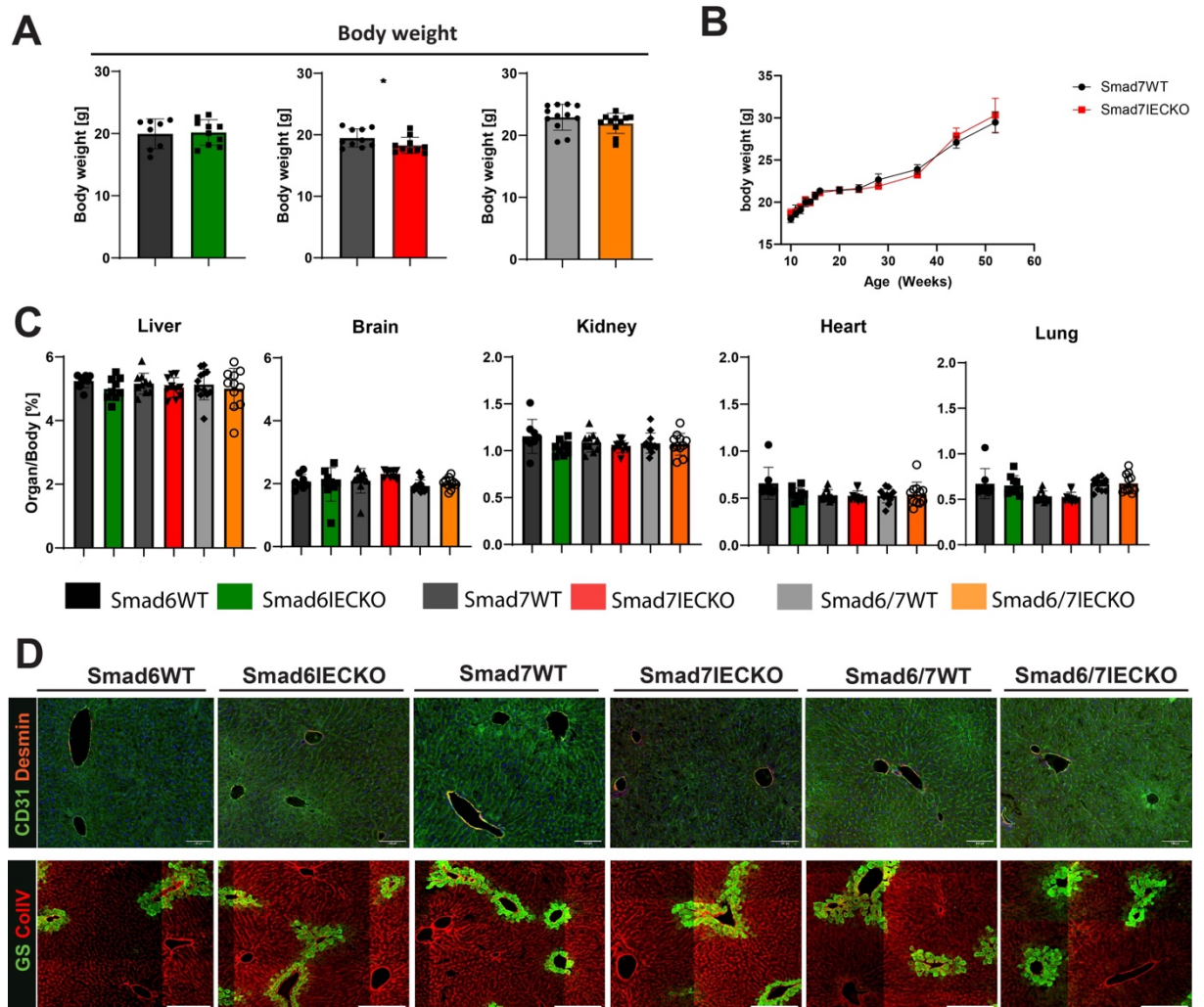
Figure 26: Loss of endothelial iSMAD during transition into quiescence does not affect mouse development or metabolic liver zonation.
(A) Body weight in Smad6IECKO (green), Smad7IECKO (red) and Smad6/7IEKO (yellow) mice at 8 weeks after postnatal deletion. (B) Body weight curve of an independent Smad7WT vs. Smad7IECKO mice group over 52 weeks starting from 10 weeks (C) Organ-to-body weight ration of liver, brain, kidney, heart and lung in mutant mice. (D) Representative images of the vasculature in liver stained for CD31 (green) and Desmin (red) in WT and Smad6IECKO, Smad7IECKO and Smad6/7IECKO mice. (E) Representative images of metabolic zonation in liver stained for GS (green) and collagen deposition stained for ColIV (orange) in WT and Smad6IECKO, Smad7IECKO and Smad6/7IECKO mice. Scale bar: 100um. Data are shown as mean ± SD. *P<0.05. Data are not significant if not indicated otherwise. Mann-Whitney *U* test.

Transcriptomic analysis of EC isolated from Smad6- and Smad7IECKO livers revealed increase in collagen production and ECM deposition. To assess the physiological significance of changes in the transcriptomic program of Smad6-, Smad7-, Smad6/7-IECKO EC, Massons Trichrome staining on liver sections of adult mice after postnatal deletion was performed by Margaret Tulessin at the Institute of General and Surgical Pathology at Technische Universität München (TUM) (Figure 27A-C). Suprisingly, transcriptomic changes did not correlate with increased collagen deposition and fibrosis (Figure 26D, Figure 27A-F).
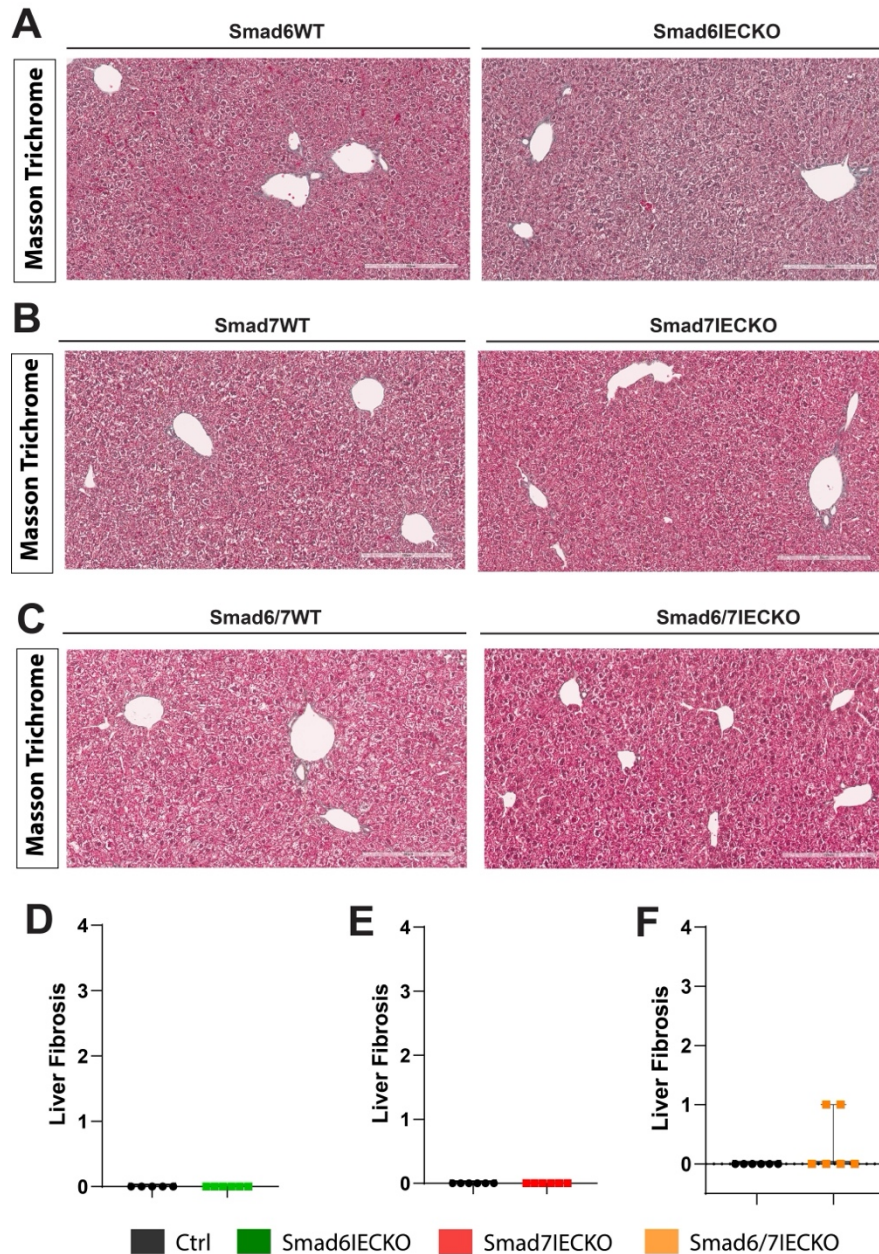
Figure 27: Transcriptional state of iSMAD-deficient EC does not predict liver fibrosis in adult.
Representative images of livers from Smad6WT and Smad6IECKO (A), Smad7WT and Smad7IECKO (B), and Smad6/7WT and Smad6/7IECKO (C) mice. Scale bar: 200 μm. (D-F) Fibrotic scoring of WT and Smad6IECKO (D) Smad7IECKO and Smad6/7IECKO (E) livers (*n* = 12 mice). Data expressed as median

with range. Data are not significant if not indicated otherwise. Mann-Whitney *U* test. Data produced jointly with Dr. Carolin Mogler and Margaret Tulessin. Animal experimentation was performed by myself. Staining and scoring was performed by Dr. Carolin Mogler and Margaret Tullesin.

3.4 Endothelial iSMAD in *in vivo* vessel permeability

3.4.1 Endothelial iSMAD in basal vascular permeability

Mutations in the TGFβ/BMP pathway are drivers of vascular disease associated with enlarged blood vessels, hemorrhages and arteriovenous malformations (141, 175, 181). To evaluate the effect of acute loss of endothelial iSMAD on vessel function, a miles assay analyzing basal vessel permeability was performed. The Miles assay is a well-established functional assay that is used to evaluate baseline vascular permeability and cytokine-induced hyperpermeability (182). I treated adult mice (6 weeks) with tamoxifen-containing food pellets over a period of 2 weeks followed by 2 weeks of washout to induce acute endothelial Smad6-, Smad7- and Smad6/7 deletion. The Miles assay allowed me to study vascular permeability by measuring extravasation of Evans Blue, a low molecular weight dye, from skin vessels into the surrounding tissue (Figure 28A). I assessed basal permeability after injecting PBS intradermally into the footpad of Smad6IECKO (Figure 28B), Smad7IECKO (Figure 28C), Smad6/7IECKO (Figure 28D) and corresponding WT mice. Female and male Smad6IECKO, Smad7IECKO and Smad6/7IECKO did not show altered basal vessel permeability compared to WT littermate controls after acute iSMAD deletion (Figure 28B-D).
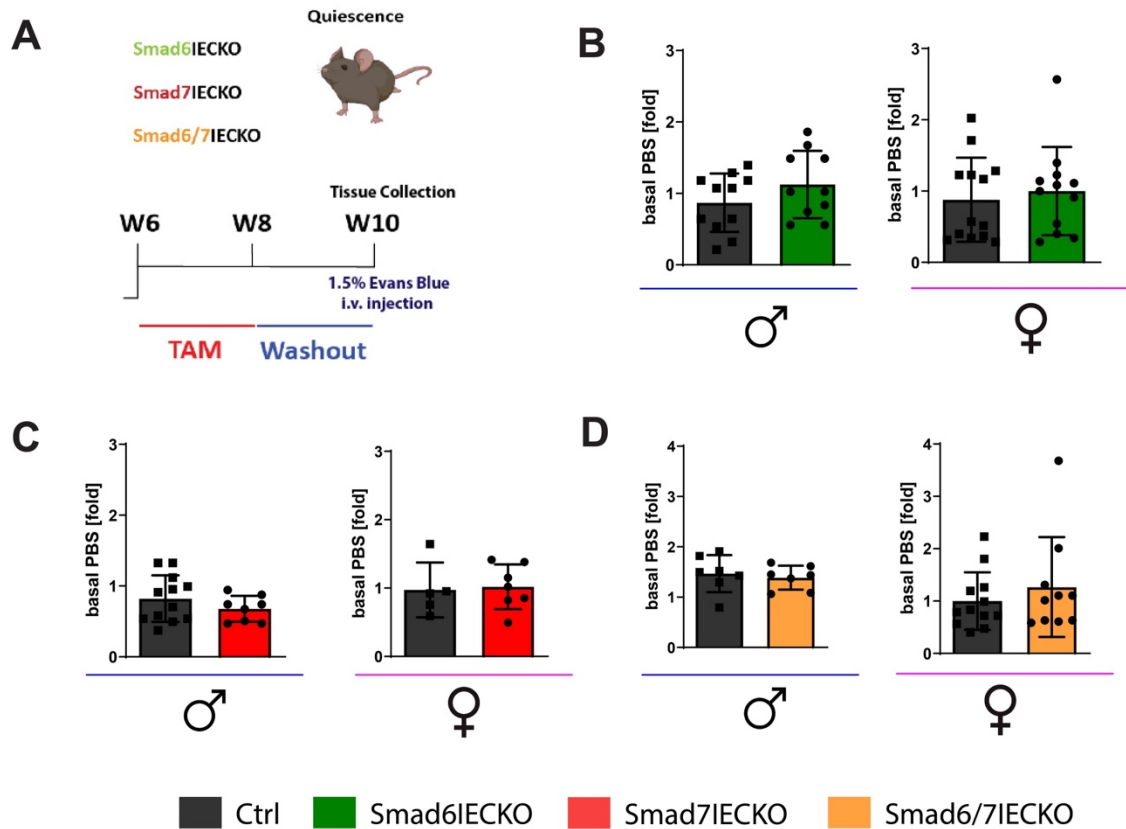
Figure 28: Endothelial iSMAD deletion does not alter baseline vessel permeability.
(A) Schematic overview of the Miles Assay. (B) Quantification of basal permeability by Miles Assay in male (left) and female (right) Smad6WT (black) and Smad6IECKO (green) mice. (C) Quantification of basal permeability by Miles Assay in male (left) and female (right) Smad7WT (black) and Smad7IECKO (red) mice. (D) Quantification of basal permeability by Miles Assay in male (left) and female (right) Smad6/7WT (black) and Smad6/7IECKO (yellow) mice. Data are shown as fold of mean Ctrl with SD. n= 5-13 Data are not significant if not indicated otherwise. Mann-Whitney *U* test.

3.4.2 Endothelial iSMAD in histamine-induced permeability

To observe vascular functionality under pathological conditions, an inflammatory hyperpermeability model using acute histamine-stimulation was performed. During acute inflammation and allergic reaction, histamine induces endothelial barrier disruption that can lead to edema, urticaria and anaphylactic shock. Injecting histamine into the footpad led to a 2-5-fold increase in vessel permeability and extravasation of Evans Blue from the collected tissue. However, deletion of endothelial Smad6 (Figure 29A), Smad7 (Figure 29B) or Smad6 and 7 (Figure 29C) did not affect pathological vessel hyperpermeability. Overall, neither single nor double loss of endothelial iSMAD *in vivo* affected physiological basal permeability or pathological histamine-induced hyperpermeability.
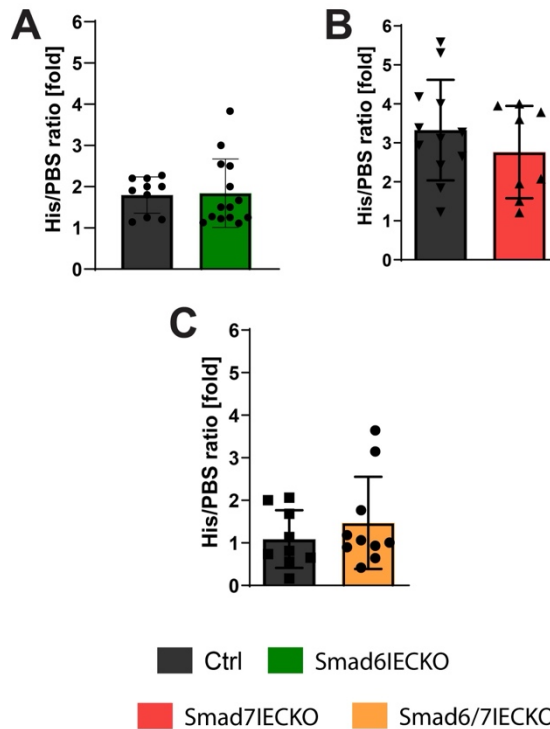
Figure 29: Endothelial iSMAD deletion does not alter histamine-induced vessel permeability.
(B) Quantification of histamine-induced vessel permeability in gender-mixed Smad6WT (black) and Smad6IECKO (green) mice. (C) Quantification of histamine-induced vessel permeability in gender-mixed Smad7WT (black) and Smad7IECKO (red) mice. (D) Quantification of histamine-induced vessel permeability in gender-mixed Smad6/7WT (black) and Smad6/7IECKO (yellow) mice. Data are shown as relative permeability normalized to PBS Ctrl with SD. n=9-11. Data are not significant if not indicated otherwise. Mann-Whitney *U* test.

3.5 Endothelial iSmads in tumor angiogenesis

3.5.1 Differential tumor growth dynamics after endothelial iSMAD deletion in Lewis Lung Carcinoma

TGFβ signaling in the primary tumor has been described to have a highly contextual dual role that can inhibit or drive cancer progression (183, 184). As intracellular inhibitors, iSMAD are potential modulators of the TGFβ signaling outcome. Moreover, pathological angiogenesis is considered a hallmark of primary tumor growth. Considering previous findings showing iSMAD to be regulators of physiological angiogenesis during retinal vascularization, I used a Lewis Lung Carcinoma (LLC) model to assess the role of iSMAD on primary tumor growth and pathological angiogenesis. Following adult deletion of endothelial iSMAD, I injected LLC subcutaneously (s. c.) into the abdominal region and continuously measured tumor volume over 14 days (Figure 30A). Loss of endothelial Smad6 increased tumor growth (Figure 30B) as tumors from Smad6IECKO mice reached on average 296 ± 25 mm2 mm^2 whereas control tumors reached 214 ± 13 mm^2 at 14 days post injection. Loss of endothelial Smad7 delayed tumor growth (Figure 30C) as tumor resected from Smad7IECKO mice

reached 200 ± 27 mm^2 and control tumors reached 284 ± 29 mm^2. Loss of endothelial Smad6 and Smad7 led to similar tumor growth with tumors from Smad6/7IECKO mice reaching 234 ± 24 mm^2 and tumors from WT mice reaching 270 ± 33 mm^2 (Figure 30D). In summary, my experiments revealed distinct, differential functions of iSMAD in tumor angiogenesis.
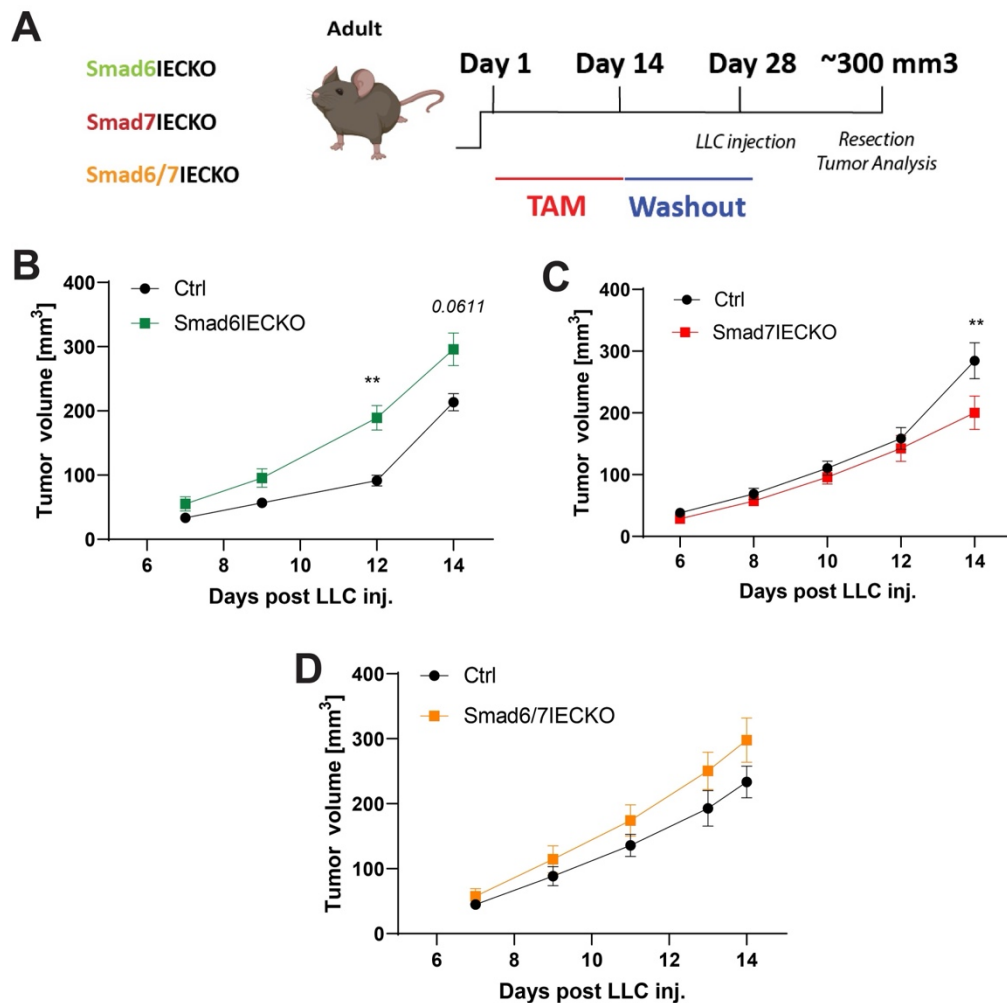
Figure 30: Endothelial iSMAD differentially regulate primary tumor growth.
(B) Growth curves of LLC tumors in WT and Smad6IECKO mice (n = 8 WT; n = 8 Smad6IECKO). (C) Growth curves of LLC tumors in WT and Smad7IECKO mice (n = 8 WT; n = 8 Smad6/7iECKO). (D) Growth curves of LLC tumors in WT and Smad6/7IECKO mice (n = 8 WT; n = 8 Smad6/7iECKO). Data are expressed as mean $\pm$ SEM. **P < 0.01. Data are not significant if not indicated otherwise. Two-way ANOVA.

3.5.2   Normal vascularization of LLC primary tumors after loss of endothelial iSMAD

To evaluate differential tumor growth dynamics in LLC primary tumors implanted into iSMADIECKO mice compared to WT mice, I performed in-depth analysis of the tumor vasculature. I stained primary tumors resected at similar size for CD31, a transmembrane glycoprotein, present at endothelial cell intercellular junctions, and desmin, an intracellular intermediate filament protein, present in pericytes (Figure 31A, 32A, 33A). I measured CD31+ area on total tumor area, vessel density and desmin coverage of vessels (Figure 31B-D, 32B-D, 33B-D). Vascularization of LLC resected from Smad6IECKO, Smad7IECKO and Smad6/7IECKO mice appeared similar to the control groups (Figure 31-33).
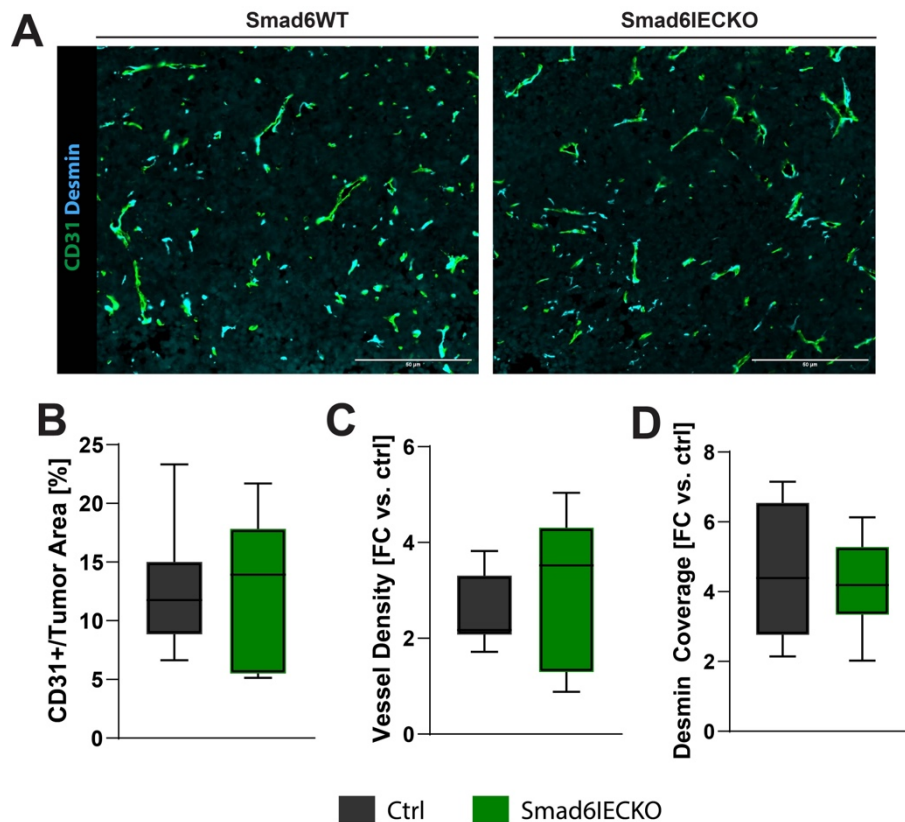
Figure 31: Normal vascularization of LLC primary tumors in Smad6IECKO mice.
(A) Representative images of the vasculature in LLC tumors stained for CD31 (green) and Desmin (cyan) in WT and Smad6IECKO mice. Quantifications of CD31+/tumor area (B), tumor vessel density in LLC (C) and desmin coverage (D). Scale bar: 50µm. n= 7. Data are shown as boxplots with Q1/Q3 quartiles and min to max. Data are not significant if not indicated otherwise. Mann-Whitney *U* test.
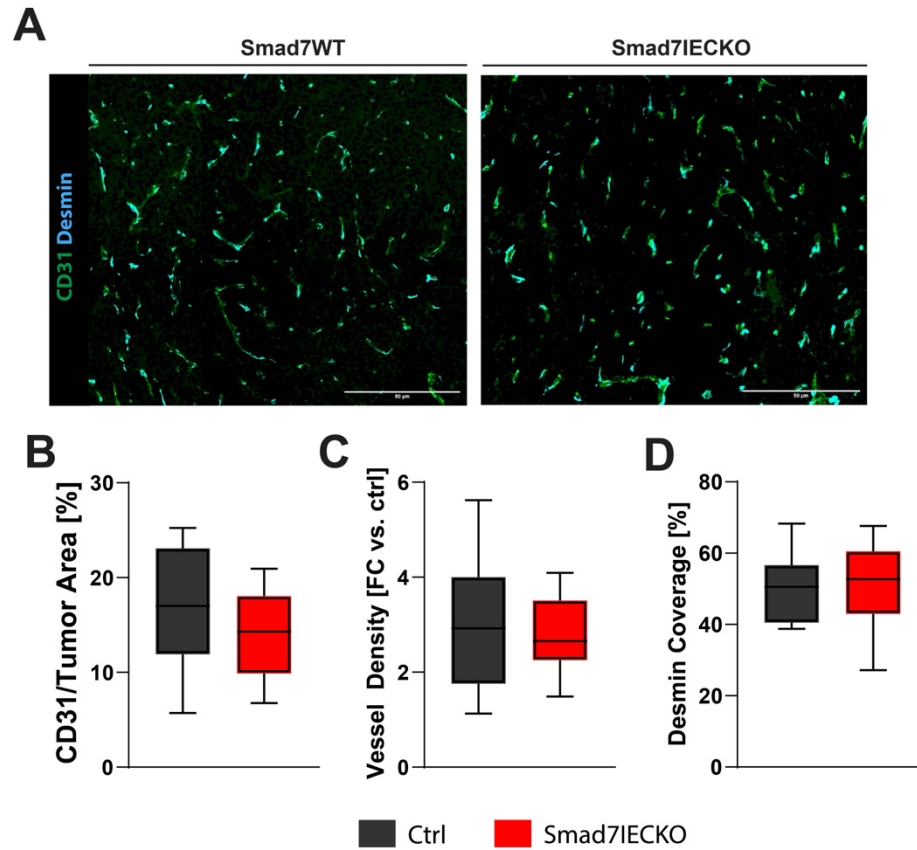
Figure 32: Normal vascularization of LLC in Smad7IECKO mice.
(A) Representative images of the vasculature in LLC tumors stained for CD31 (green) and Desmin
(cyan) in WT and Smad6IECKO mice. Quantifications of CD31+/tumor area (B), tumor vessel density
in LLC (C) and desmin coverage (D). Scale bar: 50μm. Data are shown as boxplots with Q1/Q3
quartiles and min to max. n= 9. Data are not significant if not indicated otherwise. Mann-Whitney *U*
test.
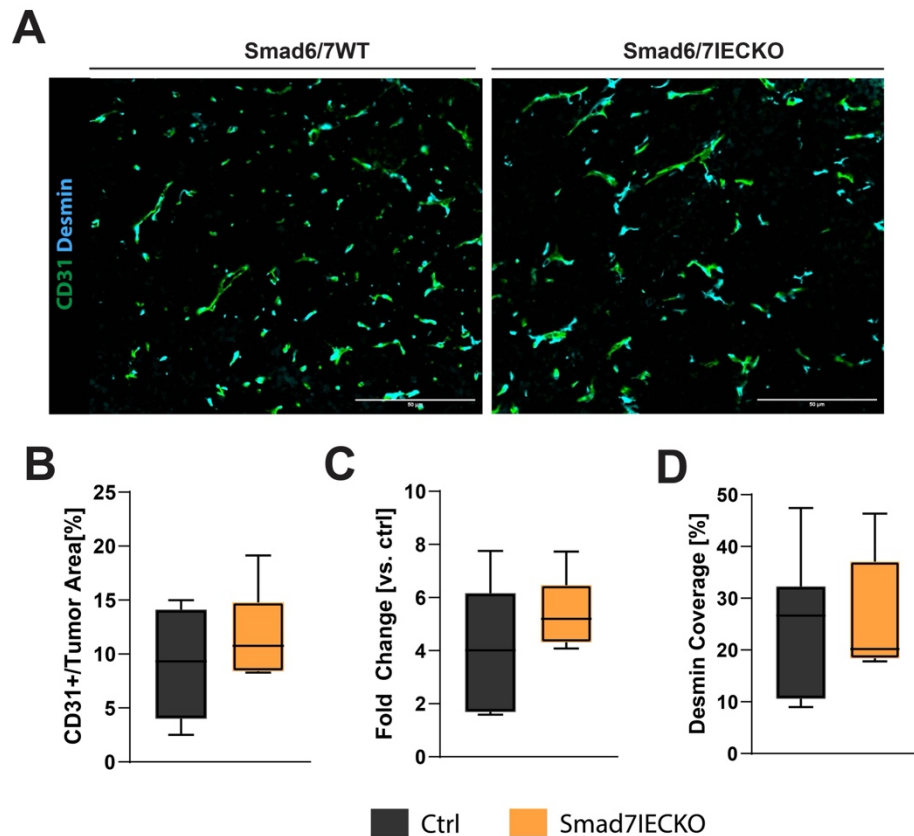
Figure 33: Normal vascularization of LLC in Smad6/7IECKO mice.
(A) Representative images of the vasculature in LLC tumors stained for CD31 (green) and Desmin (cyan) in WT and Smad6IECKO mice. Quantifications of CD31+/tumor area (B), tumor vessel density in LLC (C) and desmin coverage (D). Scale bar: 50µm. Data are shown as boxplots with Q1/Q3 quartiles and min to max. n= 6-7. Data are not significant if not indicated otherwise. Mann-Whitney *U* test.

3.5.3 Endothelial Smad6 affects tumor EC proliferation and endothelial Smad7 affects tumor EC apoptosis

I further stained primary tumors for Ki67, a proliferation marker only present in the active phase of cell cycle, and cCasp3 an apoptosis marker required for formation of apoptotic bodies. I measured CD31+KI67+ cells and CD31-KI67+ cells per tumor area, as well as CD31+cCasp3+ and CD31- cCasp3+ area on total tumor area of tumors resected from WT and Smad6-, Smad7- and Smad6/7IECKO mice (Figure 34A-F, 35A-F, 36A-F). In line with expedited primary tumor growth in Smad6IECKO mice, LLC primary tumors displayed increased apoptosis outside of the vasculature and a trend towards increased EC proliferation (Figure 34). LLC resected from Smad7IECKO mice displayed increased apoptosis inside the vasculature with no changes on EC proliferation (Figure 35). Remarkably, neither EC proliferation and apoptosis nor tumor cell proliferation and apoptosis were affected in the LLC primary tumors resected from Smad6/7IECKO mice (Figure 36). These results indicate differential and

contrasting downstream consequences of endothelial Smad6 and Smad7 functions in primary tumor growth.
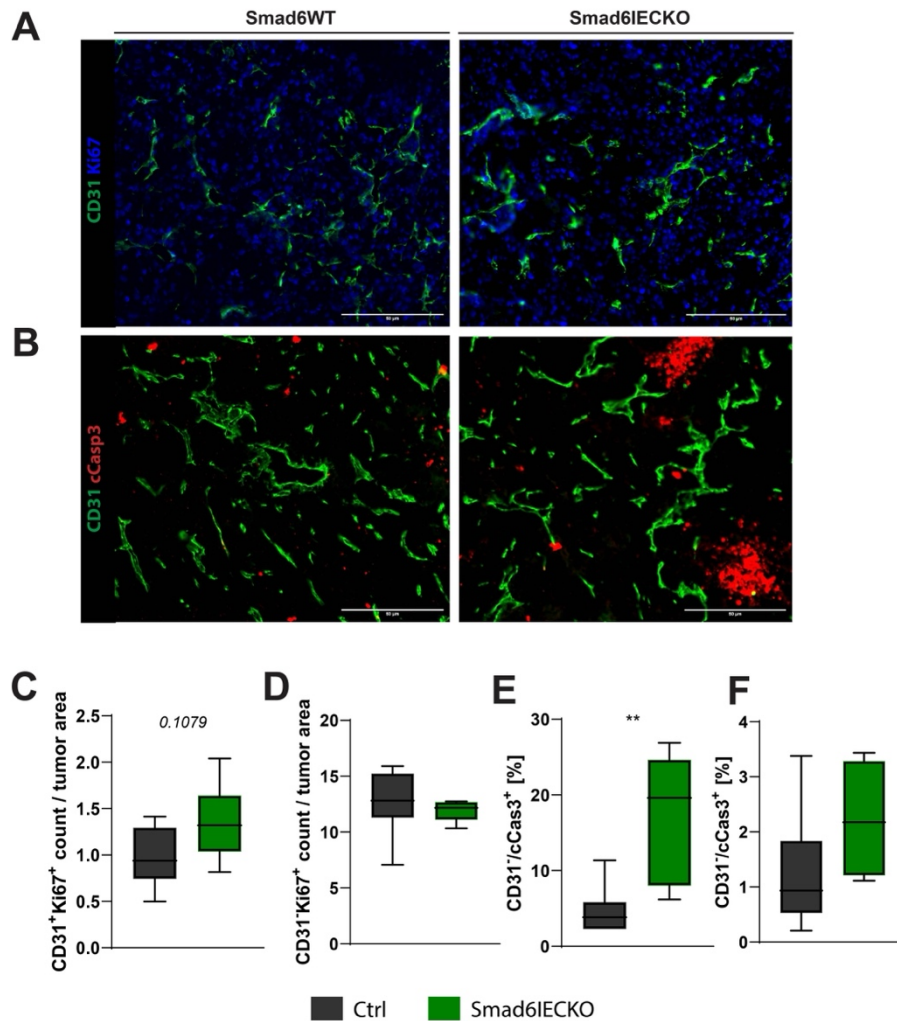
Figure 34: Intratumoral vasculature in Smad6IECKO mice becomes proliferative.
(A) Representative images of the vasculature in LLC tumors stained for CD31 (green) and KI67 (blue) in WT and Smad6IECKO mice. (B) Representative images of the vasculature in LLC tumors stained for CD31 (green) and cCasp3 (red) in WT and Smad6IECKO mice. Quantifications of CD31+/KI67+ count/ tumor area (C), CD31-/KI67+ count/ tumor area (D) [%] of CD31-/cCasp3+ (E) and [%] of CD31-/cCasp3+ area . Scale bar: 50µm. Data are shown as boxplots with Q1/Q3 quartiles and min to max. **$P < 0.01$. n= 7. Data are not significant if not indicated otherwise. Mann-Whitney U test.
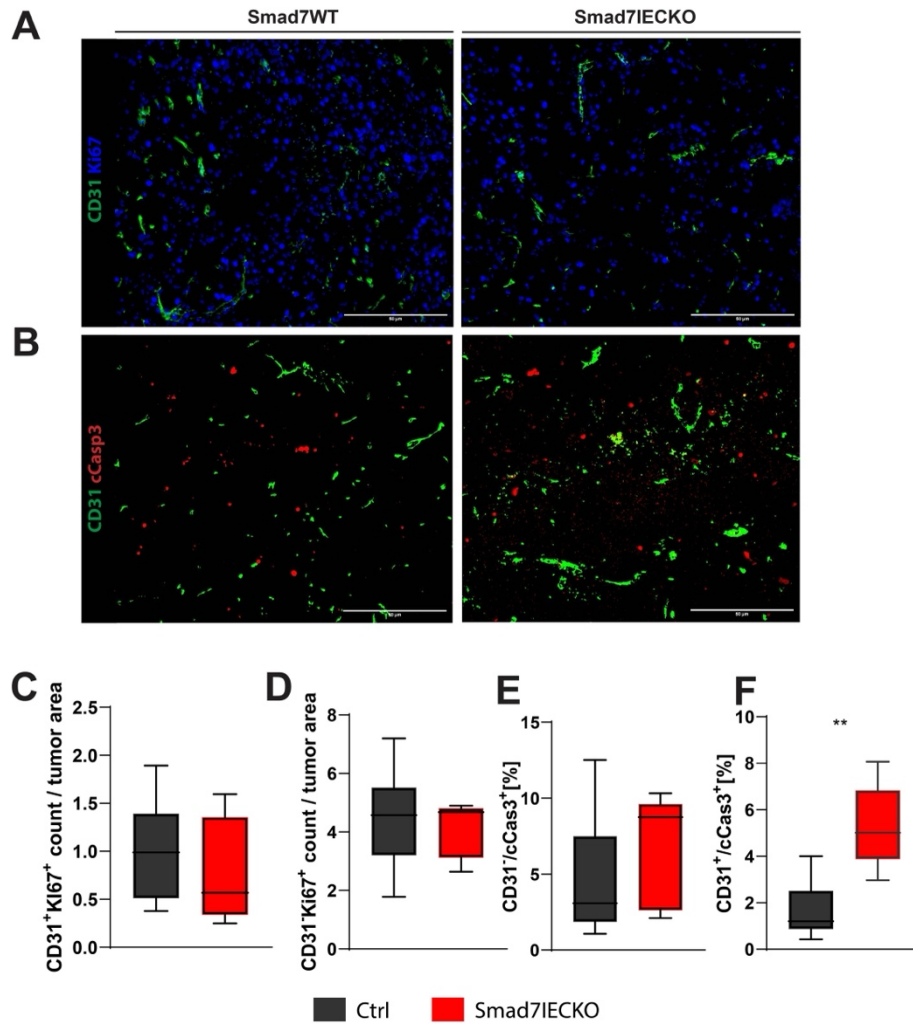
Figure 35: Intratumoral vasculature in Smad6IECKO mice becomes apoptotic.
(A) Representative images of the vasculature in LLC tumors stained for CD31 (green) and KI67 (blue) in WT and Smad7IECKO mice. (B) Representative images of the vasculature in LLC tumors stained for CD31 (green) and cCasp3 (red) in WT and Smad7IECKO mice. Quantifications of CD31+/KI67+ count/ tumor area (C), CD31-/KI67+ count/ tumor area (D) [%] of CD31-/cCasp3+ (E) and [%] of CD31+/cCasp3+ area (F) . Scale bar: 50µm. n= 9. Data are shown as boxplots with Q1/Q3 quartiles and min to max. **P < 0.01. Data are not significant if not indicated otherwise. Mann-Whitney *U* test.
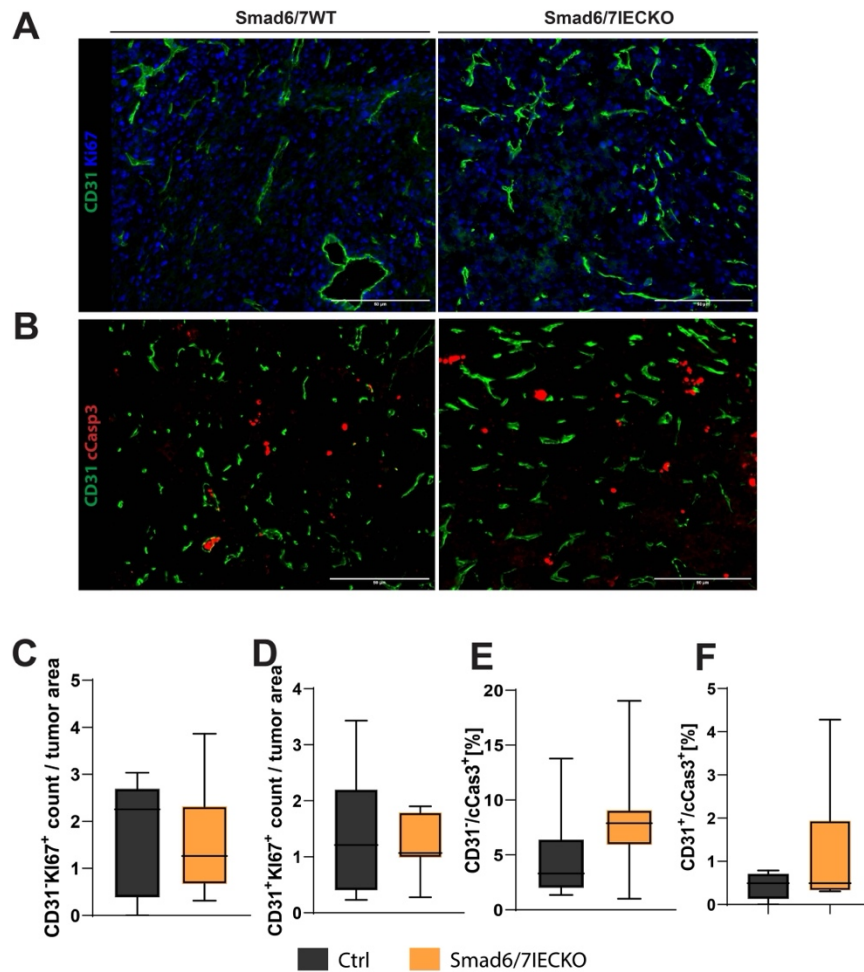
Figure 36: No difference in proliferation or apoptosis of Smad6/7-deficient tumors.
(A) Representative images of the vasculature in LLC tumors stained for CD31 (green) and KI67 (blue) in WT and Smad6/7IECKO mice. (B) Representative images of the vasculature in LLC tumors stained for CD31 (green) and cCasp3 (red) in WT and Smad6/7IECKO mice. Quantifications of CD31+/KI67+ count/ tumor area (C), CD31-/KI67+ count/ tumor area (D) [%] of CD31-/cCasp3+ (E) and [%] of CD31-/cCasp3+ area . Scale bar: 50µm. Data are shown as boxplots with Q1/Q3 quartiles and min to max. n= 6-7. Data are not significant if not indicated otherwise. Mann-Whitney *U* test.

The previous findings have shown an increase in apopototic tumor cells in LLC resected from Smad6IECKO mice and an increase of apoptotic EC in LLC resected from Smad7IECKO mice (Figure 34 and 35). To evaluate whether increased apoptosis correlates with intratumoral necrosis, I performed histological analysis via H&E staining of LLC resected from WT and Smad6IECKO (Figure 37A), Smad7IECKO (Figure 37B) and Smad6/7IECKO (Figure 37C). Necrosis scoring of tumor tissue sections performed by the pathologist, Dr. Carolin Mogler, showed no difference in necrotic area in LLC resected from Smad6IECKO (Figure 37D), Smad7IECKO (Figure 37E) and Smad6/7 (Figure 37F).
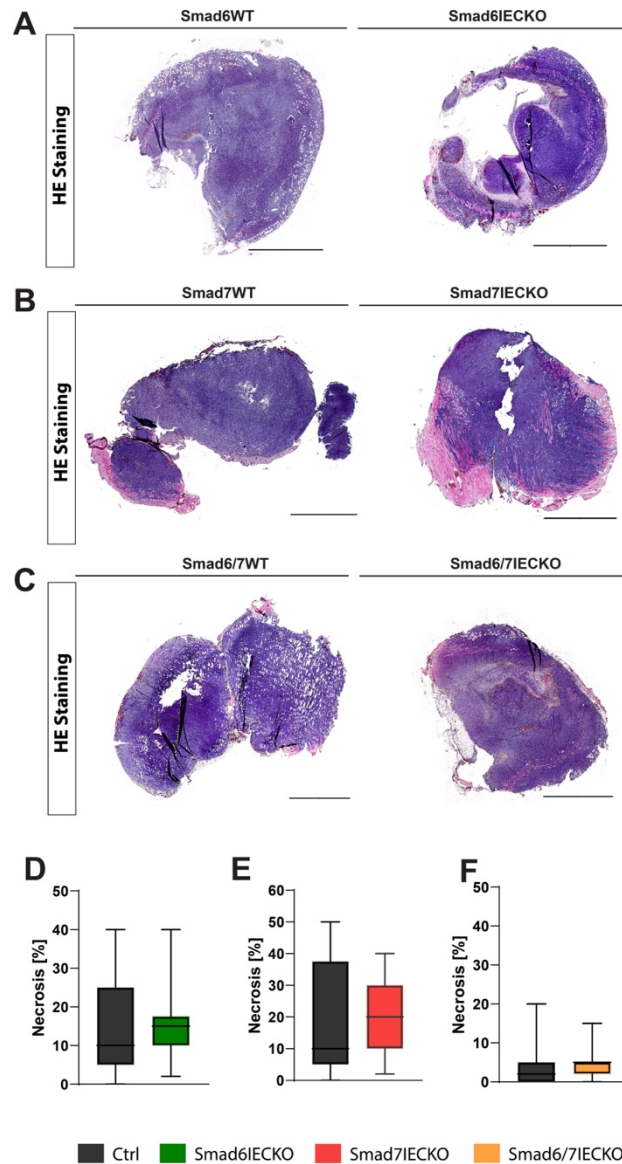
Figure 37: Endothelial iSMAD deletion does not alter necrosis LLC primary tumors.
Representative images of necrotic LLC primary tumors from Smad6WT and Smad6IECKO (A), Smad7WT and Smad7IECKO (B), and Smad6/7WT and Smad6/7IECKO (C) mice. Scale bar: 1 mm. (D-F) Quantification of necrotic areas from WT and Smad6IECKO (D) Smad7iECKO (E) and Smad6/7iECKO (F) tumors (n = 12 mice). Data are shown as boxplots with Q1/Q3 quartiles and min to max. Data are not significant if not indicated otherwise. 2-tailed Mann-Whitney U test. Necrosis scoring performed by Dr. Carolin Mogler.

3.6 Endothelial iSmad during metastasis

3.6.1 Endothelial iSMAD differentially regulate metastasis

Deletion of endothelial Smad6 and Smad7 was shown to exert contrasting effects on LLC primary tumor growth kinetics that were normalized upon combined loss of endothelial Smad6/7 (Figure 30). To further investigate whether endothelial iSMAD might also alter metastatic dissemination and

overall survival, I used a LLC-post surgical model. Here, I surgically resect the primary tumor after approximately 14 days and similar tumor size (approximately 300mm^2, causing spontaneous metastasis to the lungs. I then monitor mice daily for disease burden and sacrifice the experimental mice when termination criteria are reached. Only mice that develop lung metastasis are included in the analysis (Figure 38A). This model allows me to study overall survival after tumor resection based on spontaneous metastasis alone, closely replicating clinical phenomena. Interestingly, post-surgical survival of Smad6IECKO mice increased significantly compared to WT mice (Figure 38B) and survival of Smad7IECKO decreased significantly compared to WT mice (Figure 38C). Moreover, survival of Smad6/7IECKO mice compared to WT mice remained unaltered (Figure 38). Not only do these observations corroborate previous findings indicating differential and contrasting functions of endothelial iSMAD but also suggest a significant functional role of Smad6 and Smad7 in cancer progression and metastasis.
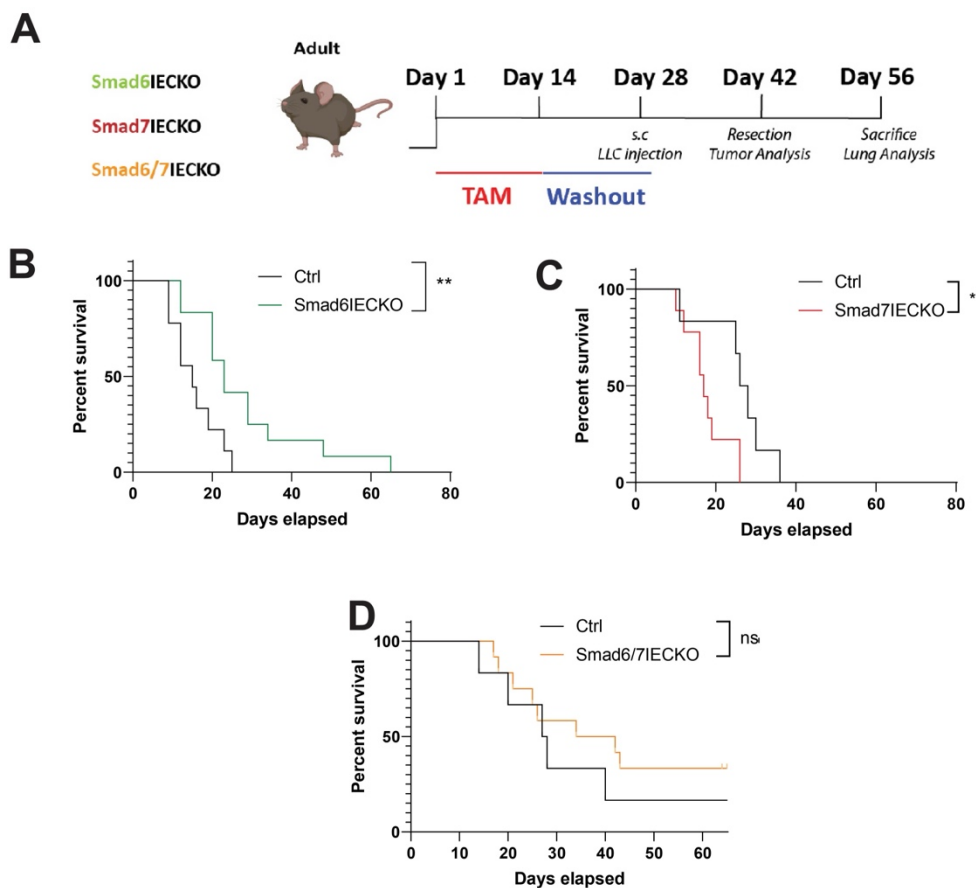
Figure 38: Endothelial Smad6 limits while Smad7 promotes metastasis
(A) Schematic depiction of LLC spontenous metastasis model (B) Kaplan-Meier survival curve of WT and Smad6iECKO mice after primary tumor removal (*n* =9-12, green). (C) Kaplan-Meier survival curve of WT and Smad7iECKO mice after primary tumor removal (*n*=6-9, red). (D) Kaplan-Meier survival curve of WT and Smad6/7iECKO mice after primary tumor removal (*n*=6-12, yellow). *P < 0.05, **P < 0.01. Gehan-Breslow-Wilcoxon test.

Metastatic dissemination is a multi-step process characterized by tumor cell intravasation, and extravasation through the vascular endothelial barrier as well as colonialization at the secondary site. The post-surgical metastasis model mimics tumor cell intravasation and extravasation and colonialization. To identify whether the observed effects on survival stem from early metastatic dissemination (intravasation) or late metastatic dissemination (extravasation and colonialization), I used an experimental metastasis model. I injected tumor cells intravenously into the tail vein of WT and Smad6IECKO, Smad7IECKO and Smad6/7IECKO mice. After 2 weeks, I collected the lungs and imaged and counted metastatic foci on the lung's surface (Figure 39A). Metastatic burden of lungs removed from Smad6IECKO, Smad7IECKO and Smad6/7IECKO mice resembled metastatic burden in lungs of WT mice (Figure 39B-E). My results indicate that the outcomes of endothelial Smad6 and Smad7 deletion in cancer progression are restricted to primary tumor growth kinetics and early metastatic dissemination.
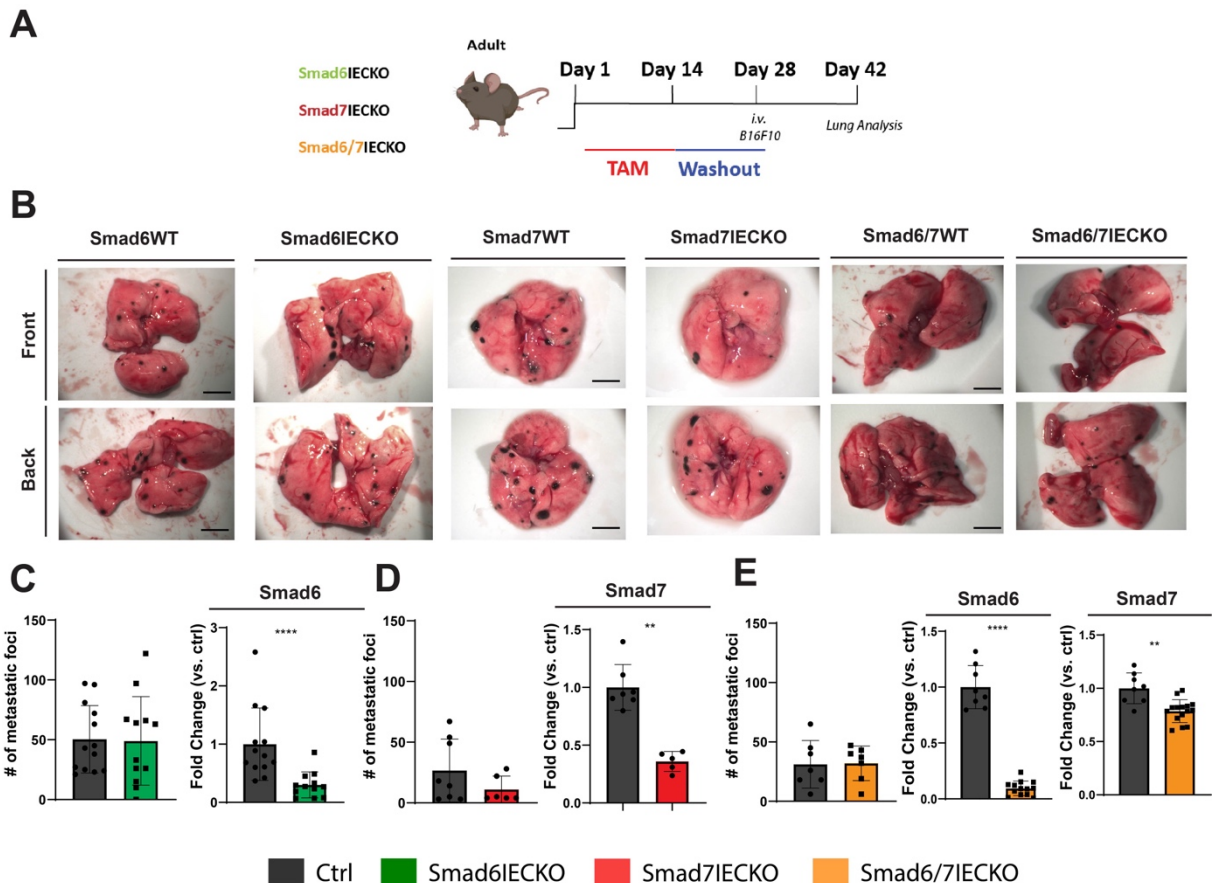
Figure 39: Loss of endothelial iSMAD does not alter metastatic colonization.
(A) Schematic depiction of B16F10 experimental metastasis model. (B) Representative images of front and back of lung metastatic foci in WT vs. Smad6IECKO (n=12), Smad7IECKO (n=6) and Smad6/7IECKO (n=7) mice. Scale bar: 5mm. Quantification of metastatic foci and deletion efficiency in WT vs. Smad6IECKO (C, green), Smad7IECKO (D, red) and Smad6/7IECKO (E, yellow) mice. Data are shown as mean ± SD. ****P < 0.0001, **P < 0.01. Data are not significant if not indicated otherwise. Mann Whitney U test.

4 Discussion

Canonical TGF-β and BMP signaling has been shown to faciliate a variety of processes during blood vessel development including angiogenesis, remodeling, arteriovenous identity and tip-stalk cell specification (22, 34, 185). Mutations in members of the canonical BMP pathway or pathological activation of the TGF-β pathway shift balance of TGF-β and BMP ligand-mediated signaling and are associated with angiogenic ocular conditions and vascular malformations including HHT, PAH and Marfan syndrome (see Figure 3). Emerging evidence points towards the importance of endothelial iSMAD in maintaining physiological TGFβ/BMP signaling balance and vascular quiescence over lifespan (49). Nevertheless, the functional significance of endothelial iSMAD in angiogenesis, quiescence and pathology remains to be studied.

In this doctoral project I generated iSMAD IECKO mice to induce single deletion and double deletion of endothelial Smad6 and Smad7. I employed cellular and functional experiments to study their role throughout vascular development, maturation, quiescence and tumor pathology. Within the scope of my doctoral work, I was able to show that (1) endothelial Smad6 but not Smad7 is indispensable during embryonic development (2) in physiological and pathological angiogenesis Smad6 and Smad7 do not act synergistically but have distinct, opposing functions (3) postnatal loss of endothelial Smad6 and Smad7 can be compensated in vascular quiescence and (4) modulation of Smad6 and Smad7 expression affected primary tumor growth and metastatic dissemination.

4.1 Endothelial Smad6 but not Smad7 is indispensable for embryonic development

The TGFβ superfamily plays diverse but crucial roles in early embryogenesis and postnatal development (131). In embryonic development, BMPs and Nodal/Activins form concentration gradients and provide ventralizing cues in the zygote that define and pattern the embryonic axis and induce the formation of the three germ layers (186). However, in blood vessel development, evidence on the role of TGFβ superfamily signaling is recently emerging and the integration of the often times conflicting TGFβ and BMP signaling outcomes remains unclear (187, 188). Here, iSMAD are potential targets of signaling integration. At E10-12, Smad7 is widely expressed outside the developing central nervous system, with Smad6 and Smad7 being co-expressed in the developing cardiovascular system, the choroid plexus, pituitary gland and otic vesicle (189). At E15, in the epithelium of the cochlea, the metanephric kidney and urogenital sinus (189). In a LacZ reporter mouse, Smad6 expression was also detected in branchial arch arteries vessels in the embryonic head

(180). Mouillesseaux *et al.* further proposed Notch to set responsiveness to BMP2/6-mediated pro-angiogenic cues via the inhibitor Smad6 and Wylie *et al.* observed widespread blood vessel hemorrhages and lethality during late gestation after global Smad6 deletion (21, 180). Moreover, disruption of TGFβ/ALK5 signaling caused severe defects in vascular development during midgestation (190). Although Smad7 misexpression in a chick model caused vascular malformation during embryonic angiogenesis, global Smad7 deletion in mice did not cause blood vessel specific phenotypes (154, 155). Despite indications, evidence of the role of endothelial Smad6 and Smad7 in embryonic vascular development remains sparse and studies are limited to global, single deletion models. In the present study, I traced Smad6 and Smad7 expression in EC and found it to be gradually increased over mouse development and lifespan. Endothelial-specific deletion of Smad6 starting from E8.5 resembled the reported global Smad6 knockout reported by Wylie *et al.* with widespread blood vessel hemorrhages by E13.5 and lethality with moderate penetrance by late gestation (E18.5). Contrary to the loss of global Smad7, loss of endothelial-specific Smad7 did not affect viability of embryos. This finding implies that endothelial Smad7 alone is dispensable for embryonic development and that global KO lethality is solely attributed to impaired heart development unaffected by loss of endothelial Smad7. This study was the first to observe that endothelial Smad6 and Smad7 can act synergistically in regulating TGFβ superfamily signaling as double deletion of endothelial Smad6 and Smad7 lead to lethality with high penetrance due to hemorrhages, edema and intrauterine inflammation causing complete abortion of pregnancy. My findings also support a model in which endothelial Smad6 can compensate for endothelial Smad7 functions but not vice versa during embryonic development. Studies in other cell types describe Smad7 to be a general TGFβ signaling antagonist while Smad6 inhibits the BMP pathway specifically (191, 192). Taken together, my findings show, that during embryogenesis, Smad6 and Smad7 cooperate but that the BMP-mediated pathway and its regulator endothelial Smad6 play a role of greater importance for blood vessel development while Smad7 only has a supportive function.

4.2 Endothelial iSMAD modulate physiological and pathological angiogenesis

Accumulating evidence suggest TGFβ and BMP signaling to be key regulators of postnatal angiogenesis (193, 194). During postnatal development, BMPs act as morphogens and support organogenesis in a variety of organs while TGFβs and BMPs can regulate epithelial-mesenchymal transition (EMT), a process necessary during organ development for the invasion of cells into surrounding tissue (195, 196). Enigmatically, studies suggest both TGFβ-mediated and BMP-mediated signaling to have pro- and anti-angiogenic effects on the endothelium (197). BMP-mediated pro- or

Discussion

anti-angiogenic effect is highly dependent on type I receptor heterogeneity and ligand availability. Pro-angiogenic outcomes were demonstrated for BMP2/4 and 6 (198-201). Anti-angiogenic outcomes for BMP9 and 10 (167, 177, 202). In retinal angiogenesis, disruption of endothelial ALK2 or 3 partially phenocopied vascular defects of endothelial BMPR2 deletion linking pro-angiogenic BMP signaling through BMP2/4/6/ALK3 to the vascular front and BMP2/4/6/ALK2 to the vascular front and plexus (203). In contrast, mutations in ALK1 are linked to HHT, a disease closely associated with AVMs and hemorrhages (204). Indeed, inhibition of ALK1 causes hypervascularization and arteriovenous malformations in retina and liver and its high-affinity ligand BMP9 rescued the phenotype indicating an anti-angiogenic effect of BMP9/ALK1 (203, 205) (Figure 40A). In the present study, postnatal endothelial-specific deletion of Smad6 resulted in normal retinal vascularization neither affecting radial expansion nor vessel branching at P6-8. In addition, I did not observe an effect on sprouting angiogenesis in response to VEGF in an *in vitro* sprouting assay. This stands in contrast to previous reports that a global and constitutive Smad6 KO resulted in hyperbranching without affecting radial expansion (Wylie et al., 2018). Considering the widespread expression of Smad6 in other tissues and lethality with moderate penetrance during embryonic development, effects observed in retinas of global KO mice could be due to secondary developmental delays (189). Still, I found that KD of endothelial Smad6 in an EC/PC spheroid co-culture resulted in increased EC proliferation. I further performed an OIR model to observe pathological neovascularization as I hypothesized that under pathological conditions, a possible effect on EC proliferation might be exacerbated. Indeed, I found that loss of postnatal Smad6 lead to increased extent of pathological neovascularization. Taken together, this indicates that downregulation of Smad6 during vascular development enables EC proliferation and that postnatal but not embryonic expression of endothelial Smad6 is dispensable. Signaling by TGFβs in concert with VEGF/flk-1-activated p38 induce pro-apoptotic signaling and anti-angiogenesis in EC (193, 206). In an OIR model, TGF-β1 suppressed proliferation of EC and neovascularization of the retina further supporting its anti-angiogenic effect (207). The present study indicates that Smad7 suppresses TGFβ-induced anti-angiogenic effect in the retina as evidenced by decreased radial expansion of retinal vessels and reduced sprouting in response to VEGF in an *in vitro* sprouting assay. Deletion of both endothelial Smad6 and Smad7 during retinal angiogenesis and knockdown in the *in vitro* sprouting assay phenocopied Smad7 deletion with less severity. Decreased severity can be attributed to the opposing actions of the upstream pathways. While there are few reports of pro-angiogenic functions of low-dose TGFβ through ALK2, most mouse studies suggest pro-apoptotic and anti-angiogenic function through TGFβ/ALK5. Observed pro-angiogenic outcomes might be caused by shifts in signaling balance towards pro-angiogenic pathways in response to low levels of TGFβ. Moreover, balance of EC

Discussion

proliferation and apoptosis is a hallmark of vascular remodeling indicating that pro-apoptotic TGFβ activation might be of greater importance during vascular maturation and remodeling rather than early stages of developmental angiogenesis. To evaluate this hypothesis, in-depth analysis of EC proliferation, EC apoptosis, ColIV+ BM empty sleeves during vascular remodeling and prunning are necessary (P10 – P18). My findings, together with support from the literature, favor a model of two discrete endothelial BMP and TGFβ signaling branches in developmental and pathological angiogenesis in which ligand availability and signaling inhibition converge. I hypothesize that presence of Smad6 inhibits the dominant pro-angiogenic BMP2/4/5-ALK2/3 signaling while absence favors the dominant pro-angiogenic BMP2/4/5-ALK2/3 signaling over anti-angiogenic BMP9/10-ALK1 signaling. Smad7 inhibits pro-apoptotic TGFβ/ALK5 signaling as Smad7KD in HUVEC lead to production of TGFβ2 protein and decrease in ALK1 (Figure 40A).

I further investigated whether the observed effect of endothelial Smad6 and Smad7 in developmental angiogenesis would affect primary tumor growth. TGFβ superfamily signaling is strongly implicated in both pro-tumorigenic and anti-tumorigenic processes over tumor progression. In early tumorigenesis, TGFβ-mediated signaling causes cytostasis and apoptosis of tumor cells. In late tumorigenesis, immune evasion and epithelial-mesenchymal transition (208). Similarly, BMPs can act both as tumor suppressors and oncogenes during tumor progression (209). By regulating entry or escape of tumor cell dormancy, a reversible cell cycle arrest, TGFβs and BMPs can enable tumor cells to persist cancer therapy (210). For example, TGFβ2 is highly expressed in dormant tumor cells and is suggested to maintain tumor cell dormancy in an autocrine fashion (211-213). In contrast, endothelial-derived TGFβ1 and periostin lead to increased tumor size and escape from dormancy in dormant T4-2 breast cancer cells (214). BMP-2 is also highly expressed in patient-derived lung cancers and was shown to promote angiogenesis in primary tumors (215). The present study was the first to investigate endothelial Smad6 and Smad7 during primary tumor growth and metastatic dissemination. By utilizing a LLC primary tumor model, I found that endothelial Smad6 and Smad7 differentially modulate primary tumor growth. Loss of endothelial Smad6 lead to increased primary tumor growth, increased apoptosis in the tumor, a trend towards more EC proliferation and no changes in overall tumor vascularization possibly due to increased sensitivity to BMP2-mediated activation. Loss of Smad7 lead to decreased primary tumor growth, increased EC apoptosis, no change in EC proliferation and no difference in tumor vascularization. Loss of both Smad6 and Smad7 neither affected tumor apoptosis, proliferation or vascularization. Surprisingly, LLC primary tumors from neither single nor double iSMAD KO mice showed differences in necrotic area. In line with the suggested signaling model during developmental angiogenesis, I hypothesize that loss of endothelial

Smad6 favors activation of the BMP2-mediated pro-angiogenic BMP signaling branch while loss of endothelial Smad7 favors activation of the pro-apoptotic TGFβ signaling branch (Figure 40B).
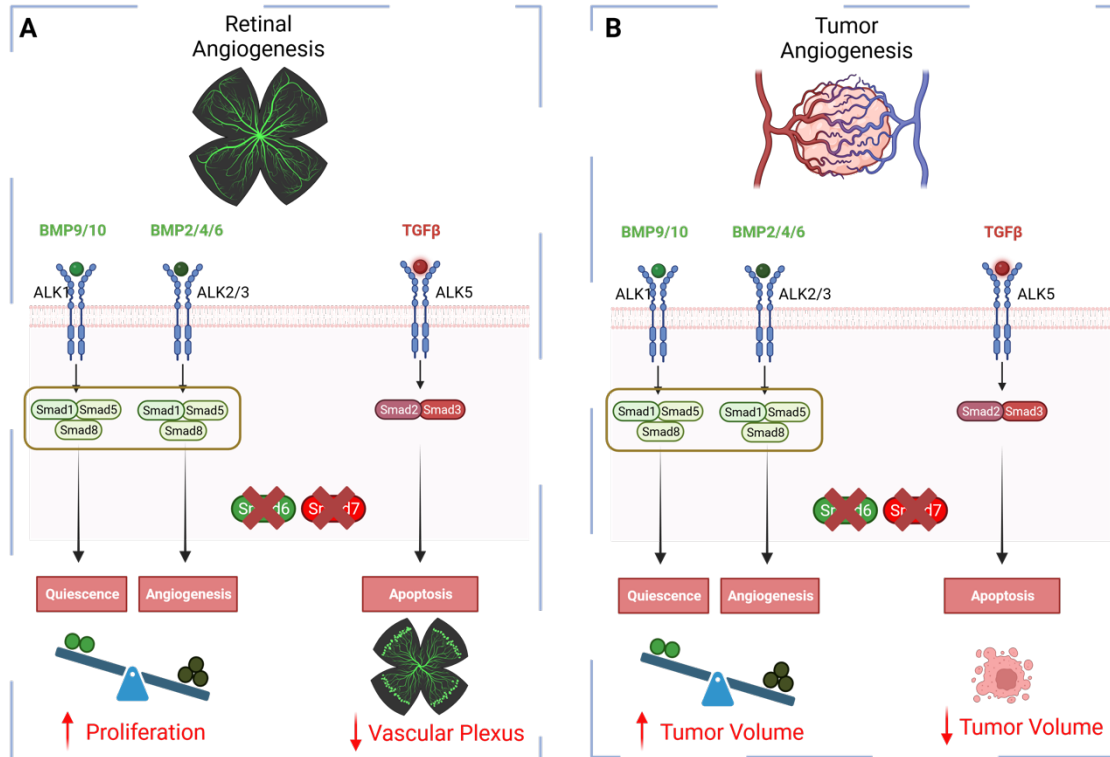
Figure 40: Schematic representation of postnatal loss of endothelial Smad6 and Smad7 in retina and tumor angiogenesis
(A) Loss of endothelial Smad6 during retinal angiogenesis leads to a shift of balance in BMP signaling from endocrine quiescence-promoting BMP9/10/ALK1 signaling to the pro-angiogenic auto- and paracrine BMP2/4/6/ALK2/3 promoting EC proliferation (203). Loss of endothelial Smad7 leads to a delay in retinal angiogenesis possibly due to TGFβ/Smad2/3-mediated apoptosis and vessel remodeling. (B) Similarly, loss of endothelial Smad6 during tumor angiogenesis leads to a shift in balance towards auto- and paracrine pro-angiogenic BMP signaling causing increase in tumor growth whilst loss of endothelial Smad7 leads to increased TGFβ activation causing EC apoptosis and decrease in primary tumor volume.

4.3 Endothelial iSMAD are dispensable for acquisition of vascular quiescence

The window between postnatal life and adult homeostasis is critical for morphogenic events that facilitate vascular remodeling, maturation and homeostasis (216, 217). Following postnatal development, ECs adopt cellular quiescence and repress their proliferative capacity under homeostatic conditions (50, 218). In the present study, I employed one functional and one mechanistic *in vitro* model of endothelial quiescence. I found that Smad6KD but not Smad7KD led to

Discussion

increased proliferation of EC in an *in vitro* 3D co-culture spheroid model. Proteomic profiling of endothelial quiescence in HUVEC indicate regulation of mitochondrial function by SMAD6 and regulation of collagen production and deposition by Smad7. Previously, epigenetic and transcriptomic analyses by Schlereth *et al.* have revealed the TGF-β superfamily to be among the most significantly regulated pathways during acquisition of vascular quiescence in the lung endothelium (49). Likewise, Kalukaukas *et al.* have shown that embryonic expression of endothelial Smad6 regulates hepatic vascular development in early postnatal development (219). To determine the functions of Smad6 and Smad7 within the window between postnatal development and adult homeostasis in the lung and liver endothelium, I performed *in vivo* transcriptomic profiling of adult EC after postnatal iSMAD deletion. Overall, I found that loss of endothelial Smad6 and Smad7 only yielded few commonly regulated genes. In line with previous functional characterization, Smad6-deficiency in the lung endothelium correlated with activation of cellular processes and Smad7-deficiency correlated with negative regulation of cellular processes supporting discreet function of Smad6 and Smad7. In the liver endothelium, Smad6- or Smad7-deficiency correlated with increased collagen deposition, ECM deposition and mesenchymal transition. The ECM controls the EC cytoskeleton and deposition and degradation orchestrate both neovessel stabilization and vascular maturation (220, 221). Moreover, double iSMAD deletion affected the transcriptome of lung and liver endothelium differently. In the lung endothelium, distinct transcriptomic changes of Smad6- and Smad7-deficiency lead to an additive effect while in liver endothelium double deletion caused the opposite effect. While the cell- and context-dependent function of TGFβ and BMP signaling is well known, my results suggest a heterogenous function in the same cell type within different vascular beds. Considering the organotypicity of the continuous and sinusoidal endothelium, this is of potential interest for further study. Surprisingly, the transcriptomic results did not translate into pathophysiology at adult stage. Neither body weight, organ-to-body weight ratio, liver vascularization, pericyte coverage, collagen deposition nor metabolic zonation was affected. In addition, no organ damage or liver fibrosis was observed. When testing for general vessel functionality after acute iSMAD deletion both basal vessel permeability and histamine-induced hyperpermeability was unaffected. A similar incongruence between the transcriptional state of EC and pathophysiology has been reported recently (222). Overall, the lack of development delay or pathogenesis during adult homeostasis call into question the significance of endothelial Smad6 and Smad7 in establishing or maintaining vascular quiescence or the direct correlation of expression level and functions. On-off genetic mouse models might also not properly resemble functions of molecules with bell-shaped signaling responses as evidenced by general low magnitude of transcriptional changes. Based on my previous finding in the postnatal stage, I hypothesize that endothelial Smad6

and Smad7 might play a more nuanced role in rearrangement processes during vessel maturation that might not immediately translate into pathology and necessitate lineage tracing and longitudinal tracking of EC over postnatal development as done in a study by Kam *et al.* (216) (Figure 41)*.*
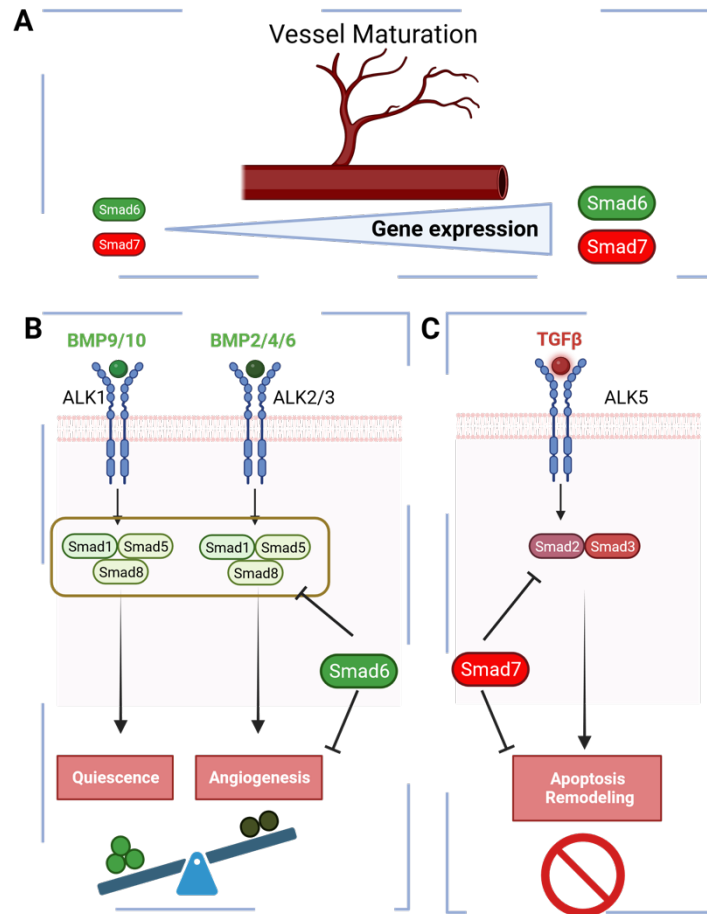
Figure 41: Proposed possible functions of Smad6 and Smad7 in vessel rearrangement.
(A) Endothelial iSMAD are gradually upregulated over acquisition of vascular quiescence. (B) Smad6 balances BMP signaling by inhibiting activation of para- and autocrine activation of EC thus limiting pro-angiogenic cues and favoring endocrine activation of endothelial quiescence. (C) Smad7 halts vascular maturation by inhibiting EC apoptosis and subsequent vessel remodeling preventing excessive vascular remodeling thus establishing vascular quiescence.

4.4 Endothelial iSMAD regulate metastatic dissemination

Cancer mortality is highly dependent on the capacity of the tumor cells to metastasize to distant organs via the lymphatic or hematogenous route (223). I found that Smad6 and Smad7 differentially modulate survival in an LLC resection metastasis model but did not affect metastatic colonialization in an experimental B16F10 model. The resection metastasis model allows to simulate the full metastatic cascade from primary tumor resection, to intravasation, extravasation and colonialization

in the lung resembling the sequence of events observed in the clinic (224). The experimental metastasis model is limited to extravastion and colonialization (225). My results indicate that endothelial Smad7 expression during intravasation of tumor cells is beneficial to survival, while Smad6 expression during early metastatic dissemination is detrimental to survival. I hypothesize that this could be due to the suppression of pro-angiogenic BMP-mediated signaling by endothelial Smad6 and suppression of angiocrine TGFβ signaling by Smad7. A possible mechanism could be the angiocrine induction or escape of tumor cell dormancy (226) (Figure 42). DDL4 expression on EC was shown to induce Notch3-dependent escape of tumor cells from dormancy (227). Several members of the BMP pathway have been implicated in inducing tumor cell dormancy (210, 228, 229)(Figure 42A). In addition to TGFβs role in induction of EMT during metastasis, TGFβ1 in combination with ECM components such as periostin also facilitates a permissive microenvironment for tumor cell activation and metastatic spread (214)(Figure 42B). To further elucidate the role of endothelial TGFβ and BMP regulation in angiocrine tumor cell dormancy, comprehensive *in vitro* and *in vivo* analyses reconstructing the early metastatic cascade are necessary. These include invasion and transmigration assays as well as omics analyses of the angiocrine secretome.
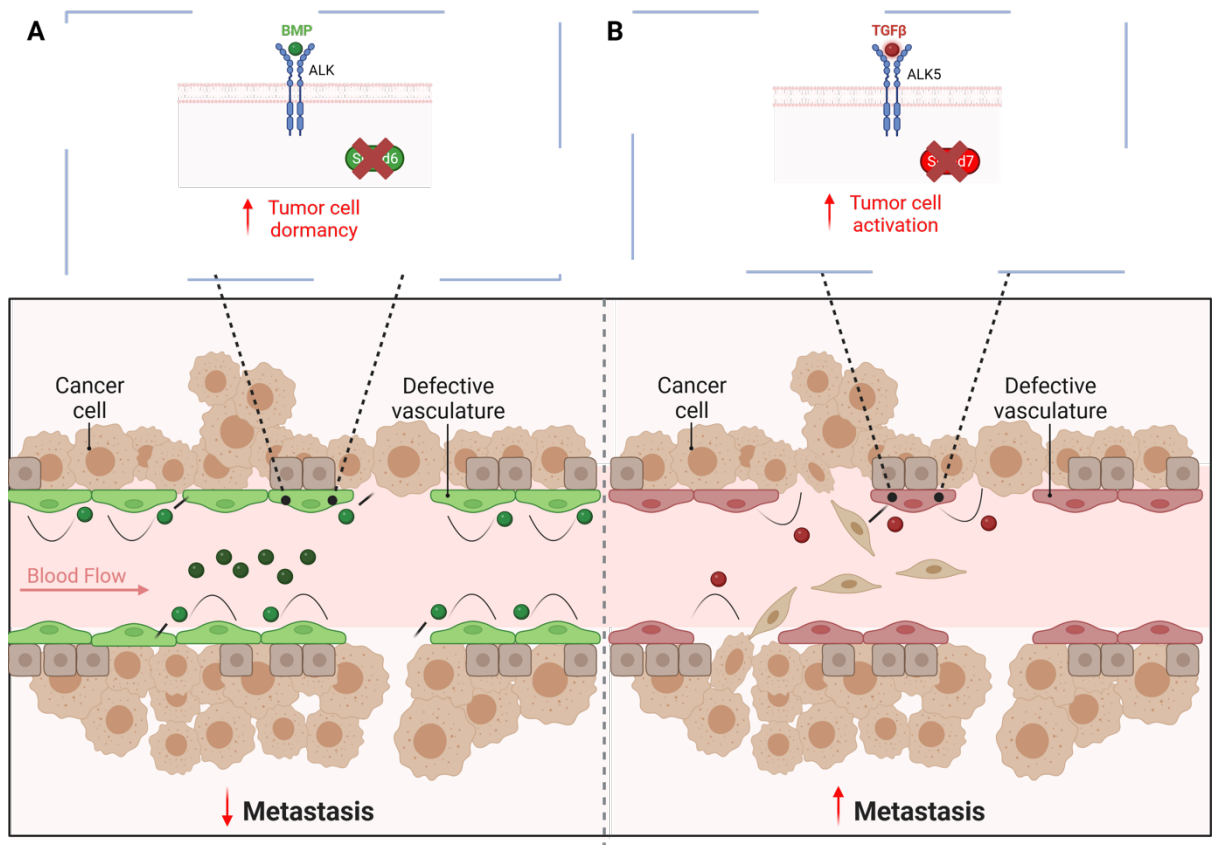
Figure 42: Proposed mechanism of endothelial Smad6 and Smad7 in metastatic dissemination
(A) During metastatic dissemination, loss of endothelial Smad6 promotes angiocrine signaling to causes tumor cells dormancy. (B) Loss of Smad7 promotes angiocrine signaling that causes tumor cell activation and EMT.

4.5 Concluding remarks

By employing genetic mouse models for timed functional experiments at different developmental stages, transcriptomic and proteomic analyses as well as 2D and 3D *in vitro* cell culture models of primary human endothelial cells I am able to demonstrate that postnatal endothelial iSMAD expression modulates physiological and pathological angiogenesis in distinct ways without detrimentally affecting establishment of vascular quiescence. Nevertheless, I found that endothelial Smad6 and Smad7 have a nuanced and discreet role in modulating endothelial cell behavior. Based on the phenotypic and functional characterization, I hypothesize that this occurs by shifting the balance between discrete BMP and TGFβ signaling branches. To further elucidate their role in homeostasis, lineage tracing and longitudinal tracking of EC during vascular remodeling and rearrangement can be performed. My data also demonstrates a discreet role of endothelial Smad6 and Smad7 as modulators of tumor progression and metastasis, opening the possibility of a role as regulators of endothelial angiocrine signaling and tumor cell dormancy.

5 Materials

5.1 Chemicals

Table 1 Chemicals

Company
AppliChem (www.appliedchem.com)
Carl Roth (www.carl-roth.de)
Gerbu (www.gerbu.de)
Merck (www.merk.de)
Roche (www.roche-apllied-science.com)
Sigma-Aldrich (www.sigmaaldrich.com)
Serva (www.servo.de)
Thermo Fisher Scentific (www.thermofisher.com)

5.2 Growth Factors and Enzymes

Table 2 Growth Factors and Enzymes

Reagent	**Company**
DMEM/F12	Thermo Fischer Scientific
Fetal calf serum (FCS), heat inactivated	PAA Laboratories
Liberase	Roche
RNase-free DNAseI	Roche
Human recombinant TGFβ1	R&D Systems
Human recombinant TGFβ2	R&D Systems
Human recombinant VEGF	R&D Systems
Proteinase K	Gerbu

5.3 PCR/RT-qPCR

5.3.1 Reagents

Table 3 PCR/RT-qPCR reagents and buffers

Reagent	Company
Direct PCR lysis Reagent	PeqLab
DNase/RNase free H2O	Gibco
Ethidium Bromide	Roth
TaqMan™ Fast Advanced Master Mix	Thermo Fisher Scientific

5.3.2 Genotyping primers

Table 4 Genotyping primers

GENOTYPE	PRIMER NAME	SEQUENCE
SMAD6$^{FL/FL}$	Smad6 F	CTGGTGATTGGAGGCAGTCCATGCA
	Smad6 ttR	CACCCCAAAGTGCTGGGATTAAAGG
SMAD7$^{FL/FL}$	Smad7 F	GGACTGCCTGGAGAAGTGTG
	Smad7 R	TCAGGTTGGATCACCATGC
CDH5-CRE^{ERT2}	Cre for	CAGGGTGTTATAAGCAATCCC
	Cre rev	CCTGGAAAATGCTTCTGTCCG
	Actin for	CAATGGTAGGCTCACTCTGGGAGATGATA
	Actin rev	AACACACACTGGCAGGACTGGCTAGG

5.3.3 TaqManTM probes for RT-qPCR

All TaqMan^{TM} probes were purchased from Thermo Fisher Scientific

Table 5 TaqMan^{TM} probes for RT-qPCR

Target gene (ms)	Ordering number
Actb	Mm00607939_S1
Smad6	Mm01171378_m1
Smad7	Mm00484742_m1

Target gene (hs)	Ordering number
ACTB	Hs01060665_g1
SMAD6	Hs00178579_m1
SMAD7	Hs00998193_m1

5.4 Vectors

5.4.1 Target constructs

shRNA	Target Gene	Company
control RFP	TurboRFP	Horizon Discovery
control GFP	TurboGFP	Horizon Discovery
nsh	non-targeting	Horizon Discovery
sh118	Smad6	Horizon Discovery
sh115	Smad7	Horizon Discovery
sh137	Smad6	Horizon Discovery
sh699	Smad7	Horizon Discovery

5.4.2   Backbones

Backbone	Inserts	Company
pGIPZ	turboRFP, turboGFP, sh699, sh137	Horizon Discovery
SmartVector	nsh, sh118, sh115	Horizon Discovery

5.4.3 Viral plasmids

Plasmid	Function	Company
pMD2.G	envelope	Addgene
psPAX2	packaging	Addgene

5.5 Kits

Table 6 Kits

Reagent	Company
Annexin V Staining Kit	Biolegend
Arcturus PicoPure RNA Isolation Kit	Thermo Fisher Scientific
GenElute™ Total RNA purification Kit	Merck
Taq PCR Core Kit	Qiagen
Quantitect Reverse Transcription Kit for cDNA Synthesis	Qiagen
Quibit Assay Kit	Invitrogen
Trichrome Stain (Masson) Kit	Sigma Aldrich
Click-iT Edu Cell Proliferation Kit	Thermo Fischer Scientific
Pierce BCA Assay Kit	Thermo Fischer Scientific
Lenti-X Concentrator	Takara Bio CloneTech

5.6 Immunfluorescence and FACS

5.6.1 Primary antibodies

Table 7 Primary antibodies

Antigen	Reactivity	Species	Conjugate	Dilution	Company (No.)
CD45	mouse	rat	FITC	1:400	BD Biosciences (553080)
Ter119	mouse	rat	FITC	1:200	BD Biosciences (557915)
Lyve-1	mouse	rat	AF-488	1:250	eBioscience (53-0443)
Podoplanin	mouse	hamster	AF-488	1:100	eBioscience (53-5381-82)
Pdgfrb	human	mouse	PE	1:100	BD Biosciences (558821)
CD31	mouse	rat	APC	1:100	BD Pharmingen (551262)
CD31	mouse	rat	-	1:100	BD Bioscience (557355)
Desmin	mouse	rabbit	-	1:100	Abcam (ab15200-1)
Ki67	mouse	rabbit	-	1:100	BETHYL Laboratories (IHC-00375)
cCas3	mouse	rabbit	-	1:100	Cell Signaling (9661)
Isolectin B4	-	-	AF-488	1:100	Invitrogen (I21411)

Collagen IV	mouse	goat	-	1:100	Novusbio (NBP1-26549)
GS	mouse	rabbit	-	1:100	Abcam (ab49873)
CD45	mouse	rat	-	1:100	Invitrogen (RM2604)
CD146	Mouse	Rat	PE/Cy7	1:100	Biolegend (134713)

5.6.2 Secondary antibodies

Table 8 Secondary antibodies

Reactivity	Species	Conjugate	Dilution	Company (No.)
Rabbit IgG	Goat	AF-546	1:500	Thermo Fischer (A21208)
Rabbit IgG	Donkey	AF-647	1:500	Thermo Fischer (A31573)
Rat IgG	Goat	AF-488	1:500	Thermo Fischer (A21049)
Mouse IgG	Goat	AF-647	1;500	Thermo Fischer (A21237)

5.6.3 Staining reagents

Table 9 Staining reagents

Staining	Company
CD31 MicroBeads, mouse	Thermo Fisher Scientific
Click-IT^{TM} EdU Alexa 647 Flow Cytometry Assay Kit	Thermo Fisher Scientific
Eosin	Sigma Aldrich
Fluorescence mounting medium	DAKO
Hemalaun	Sigma Aldrich
Histomount	Invitrogen
Hoechst Dye 33258, 1mg/ml	Merck
Normal goat serum ready-to-use (10%)	Zymed
FxCycle Violet	Thermo Fischer Scientific
Proteinase K	Gerbu
Roti-Histofix 4% (pH 7)	Carl Roth
Sucrose	Merck
Tissue-Tek O.C.T.^{TM} Compound	Scigen
Triton X-100	Thermo Fisher Scientific

5.7   Animal experimentation

Table 10 Reagents for animal experimentation

Reagent	Company
A115-T7040 Tamoxifen Food	Ssniff Spezialdiäten GmbH
Bepanthen® eye cream	Roche
Betaisodona	Mundipharma
CreActive T-400 Tamoxifen Food	Genobios
Ethicon Suture Silk 4-0	Johnson & Johnson
Ethicon Suture Silk 5-0	Johnson & Johnson
Ketavet	Pfizer
NaCl solution	Braun
Rompun	Bayer
Sevofluran	Baxter
Surgical Equipment	Fine Science Tools
Tamoxifen	Sigma Aldrich
(Z)-4-Hydroxytamoxifen	Sigma Aldrich

5.8   Solutions and buffers

Table 11 Solutions and buffers

Buffer	Composition	
Ammonium chloride potassium buffer (ACK)	150 mM	NH4Cl
	10 M	KHCO3
	100 mM	Na2EDTA
		pH 7.2-7.4
Phosphate buffered saline (PBS)	1.34 M	NaCl
	27 mM	KCl
	200 mM	Na2HPO4
	4.7 mM	KH2HPO4
		pH 7.4
Tris-Buffered Saline Tween-20 (TBS-T)	10 mM	Tris/HCl, pH 7.5
	100 mM	NaCl
	0.1%	Tween-20
		pH7.4

Materials

Modified Protein Lysis Buffer	25 mM	Tris-HCl (pH 7.5)
	1 %	Sodium deoxycholate
	150 mM	NaCL
	0.1 %	sodium dodecyl sulfate
	1 %	NP-40
	1 µg/ml	aprotinin
	0.1 mg/ml	4-(1-aminoehtyl) Benzenesulfonyfluoride
	10 mM	sodium fluoride
	1 mM	sodium orthovanadate
	250 U/ml	benzonase
	10U/ml	DNase
MS loading buffer	2% (v/v)	acetonitrile
	0.1% (v/v)	formic acid
FACS Buffer	5% (v/v)	Fetal calf serum in PBS
TE-Buffer	10 mM	Tris
	1 mM	Na2EDTA
		pH 8.0
Trypsin Gold (Mass Spectrometry Grade)		Promega

5.9   Consumables

Table 12 Consumables

<u>Consumables</u>	<u>Company</u>
96 well plates	Steinbrenner Laborsysteme
96-well flat-bottom plates	Greiner
384 well plates	4titute
Acclaim™ PepMap™ 100 C18 Trap Column	Thermo Fischer Scientific
Cannula (18G, 19G, 27G, 29G, 30G)	BD Biosciences
Cell Scraper	Corning
Cell culture dishes (6cm, 10cm, 15cm)	TPP
Countess™ cell counting chamber slides	Thermo Fisher Scientific
Cryotubes	Carl-Roth
FACS tubes	BD Biosciences

Materials

Filter containing pipette tips	Biozym
Freezing box	Thermo Scientific
Insulin syringe	BD
LS Columns MACS®	Miltenyi Biotec
Microscope cover glasses	VWR international
Microscope glass slides	Menzel-Gläser
Peel-A-Way™ Embedding Molds	Merck
Pipette tips	Nerbe
qPCR plates (96-well)	Biozyme
qPCR plates (384-well)	Roche
Reaction tubes (0.5ml, 1.5ml, 2ml)	Eppendorf
Reaction tubes (15ml, 50 ml)	Greiner
ReproSil-Pur 120 C18 analytical column	Dr. Maisch
Sealing foil	Applied Biosystems
Sera-Mag Speed Beads	GE Healthcare
Sterile pipettes	Corning
1ml Syringes	Braun
Tissue cultures 6-well/24-well/96-well plates	Sarstedt
Biopsy Punches	Stiefel
EasyStrainer™ 100µm	Greiner
Combitips® advances 0.2ml/0.4ml	Eppendorf
Eppendorf Tubes (0.5ml, 1.5ml, 2ml, 5ml)	Eppendorf

5.10 Equipment

Table 13 Equipment

Equipment	**Company**
Axio ScanZ1 slide scanner	Zeiss
Axio Scan 7 slide scanner	Zeiss
Zeiss Cell Observer	Zeiss
Zeiss LSM 780 SD	Zeiss
Bravo Automated Liquid Handling Platform	Agilent
Cell culture hood	Thermo Fisher Scientific
Cell culture incubator	Thermo Fisher Scientific

Materials

Centrifuge	Thermo Fisher Scientific
Countess™ automated cell counter	Thermo Fisher Scientific
Digital Electronic Caliper	Fine Science Tools
Freezing box	Thermo Fisher Scientific
FACS Aria/Canto/Fusion	BD Biosciences
Heating block	Eppendorf
HM3551 microtome	Thermo Fisher Scientific
Light cycler 480	Roche
iMark™ Microplate Reader	BioRad
Magnetic stand	Thermo Fisher Scientific
Microtome Hyrax C50	Zeiss
MACS Magnetic separators	Miltenyi
Multistep pipette	Eppendorf
Mr. Frosty Freezing Container	Thermo Fisher Scientific
NanophotometerR N60	INTAS
Novaseq 6000	Illumina
Olympus IX 71	Olympus
Orbitrap Eclipse Mass Spectrometer	Thermo Fischer Scientific
Pipettes	ErgoOne
QIAxcel Advanced System Qiagen	Qiagen
Scale	Ohaus
Special accuracy weighing scale	Mettler Toledo
StepOnePlus Real-Time PCR System	Thermo Fisher Scientific
Shaver	Moser
Table centrifuge (5417R)	Eppendorf
Thermocycler	Applied Biosystems
Ultimate 3000 HPLC	Thermo Fischer Scientific
Vevo 3100	Visualsonics
Vortex	Neolab
Water bath	Julabo
Quibit Fluorometer	Thermo Fischer Scientific
Incubation Chamber/Shaker	Edmund Bühler
Microm STP 120 Tissue Processor	Thermo Fischer Scientific

5.11 Cell culture reagents

Table 14 Cell culture reagents

Reagent	**Company**
Dimethylsulfoxide (DMSO)	AppliChem
Dulbecco's Modified Eagle medium – Glutamax	Thermo Fisher Scientific
Dulbecco´s phosphate buffered saline (PBS)	Sigma Aldrich
Endopan + Growth Factor Kit	Pan-Biotech
Fetal Calf Serum (FCS, heat inactivated)	PAA
Penicillin/streptomycin (100x 104U/10mg/ml)	PAA
Puromycin	Sigma Aldrich
Trypan blue	Gibco
Trypsin-EDTA (10x)	Sigma Aldrich

5.12 Software

Table 15 Software

Software	**Company**
BenchSci	www.benchsci.com
Biorender	www.biorender.com
Fiji	ImageJ
FlowJo	Miltenyi Biotec
FACSDiva™	BD Biosciences
Gene Set Enrichment Analysis	Broad Institute
Ingenuity Pathway Analysis	Qiagen
Light Cycler 480 software	Roche
Microsoft Office	Microsoft
Molecular Signature Database (MSigDB)	Broad Institute
Prism	Graph Pad
Illustrator 2023	Adobe
Ilastik	EMBL
Image Lab Software	Bio-Rad
Qiaxcel ScreenGel	Qiagen
R Version 4.3.1	R-Project
R Studio	RStudio

Materials

ZEN Black	Zeiss
ZEN Blue	Zeiss

6 Methods

6.1 Mouse experimentation

6.1.1 Generation of transgenic mice

Transgenic mice were generated with the help of the DKFZ Transgene Service according to the guidelines of the local Animal Use and Care Committees and were approved by the local regulatory committee Bezirksregierung Karlsruhe, Germany (G16/19). ES cell clones targeted for Smad6 locus were injected into B6D2F1 x C57BL/6 blastocysts. Chimeric male offspring were bred with C57BL/6 mice and ear punches were collected from the F1 genereration. Germline transmission of the targeted Smad6 allele was confirmed by regulate PCR analysis of the genomic DNA in the ear punches. The NeoR-PGK promoter cassette was removed by mating the germline transmittion positive mice of the F1 generation to FLP-deleter mice. The following primer were used for genotyping: CSD-lacF, GCTACCATTACCAGTTGGTCTGGTGTC; CSD-neoF, GGGATCTCATGCTGGAGTTCTTCG; CSD-loxF, GAGATGGCGCAACGCAATTAATG; CSD-Smad6-R, CCAAAGTGCGTCTTTCTTGTTTCTCC; CSD-Smad6-ttR, GCATCTTTACCATCTCATTCCGCCC; CSD-Smad6-F, CACCCCAAAGTGCTGGGATTAAAGG

Table 16 Primers for Genotyping

GENOTYPE	FORWARD PRIMER	REVERSE PRIMER	AMPLICON SIZE (BP)
FLOXED	CSD-loxF	CSD-Smad6-R	309
PRECRE	CSD-neoF	CSD-Smad6-ttR	609
POSTCRE	CSD-lacF	CSD-Smad6-R	607
WILDTYPE	CSD-Smad6-F	CSD-Smad6-ttR	678
POSTFLP	CSD-Smad6-F	CSD-Smad6-ttR	822
POSTFLP&CRE	CSD-Smad6-F	CSD-Smad6-R	815

6.1.2 Animal welfare

Smad7$^{fl/fl}$ mice with a C57BL/6J background were obtained from the Jackson Laboratory (Strain#:017008). Floxed mice contain two transgenic loxP cassetes flanking the GOI that can be used to induce a conditional deletion of exon 1 (Smad7) or exon 4 (Smad6) after crossing with an approptiate cre-driver line. Smad6$^{fl/fl}$ and Smad7$^{fl/fl}$ mice were crossed with each other to generate

double floxed mice (Smad6/7$^{fl/fl}$). Smad6$^{fl/fl}$, Smad7$^{fl/fl}$, Smad6/7$^{fl/fl}$ mice were crossed with *Tg(Cdh5-cre/ERT2)1Rha* (Cdh5^{CreERT2}) mice to generate inducible endothelial-specific KOs of *Smad6, Smad7 and Smad6/7* genes (Table 16). Induction of Cre recombination was carried out by administration of tamoxifen according to the protocol indicated in each experiment.

Animals were housed in sterile cages maintained in temperature-controlled rooms and had access *ab libitum* autoclaved food and water. All animals were monitored daily for signs of illness. Postnatal mice were euthanized by rapid decapitation and adult mice were euthanized via rapid cervical dislocation of spinal cord. Part of the tail was taken for re-genotyping.

6.1.3   Mouse study approval

Mice were maintained in the German Cancer Research Center (DKFZ) specific pathogen–free facility. All studies were performed in accordance with DKFZ regulations with approval by the German regional council at the Regierungspräsidium Karlsruhe (G239/19) and (G229/20). The Smad6$^{fl/fl}$ mice were created at DKFZ (G16/19).

6.1.4   Breeding

Table 17 In-house mouse lines

GOI	SHORT NAME	FULL NAME	INDUCTION	PURPOSE
SMAD6	Smad6$^{fl/fl}$	B6.Smad6tm1a(KOMP)Wtsi / Aug	no expression	Floxed
SMAD7	Smad7$^{fl/fl}$	B6.Cg-Smad7tm1.1Ink/J	no expression	Floxed
SMAD6 *SMAD7*	Smad6 x Smad7$^{fl/fl}$	B6.Smad6tm1a(KOMP)Wtsi/Aug B6.Cg-Smad7tm1.1Ink/J	no expression	Floxed
FLP	Fip recombinase	B6-Tg(ACTFLPe)9205Dym	constitutive	removal of frt sites in tm1a constructs
CDH5	Cdh5^{CreERT2}	*Tg(Cdh5-cre/ERT2)1Rha*	Constitutive	Endothelial-specific driver line
SMAD6	Smad6IECKO	B6-Smad6tm1a(KOMP)Wtsi Tg(Cdh5-cre/ERT2)1Rha / Aug	Pups: TAM-OH (50µg) Adult *(ad*	Endothelial cell-specific *Smad6* deletion

			libitum): CreActive. T400 (10 mm, Rad), Genobios, Laval)	
SMAD7	Smad7IECKO	B6-Smad7tm1.1Ink Tg(Cdh5-cre/ERT2)1Rha	Pups: TAM-OH (50µg) Adult *(ad libitum)*: CreActive. T400 (10 mm, Rad), Genobios, Laval)	Endothelial cell-specific *Smad7* deletion
SMAD6 X SMAD7	Smad6/7 IECKO	B6-Smad7tm1.1Ink Tg(Cdh5-cre/ERT2)1Rha Smad6tm1a(KOMP)Wtsi / Aug	Pups: TAM-OH (50µg) Adult *(ad libitum)*: CreActive. T400 (10 mm, Rad), Genobios, Laval)	Endothelial cell-specific *Smad6 and Smad7* deletion

6.1.4.1   Induction of cre recombination

Deletion in embryonic development:

Genetic deletion in the Smad6, Smad7 and Smad6/7IECKO control and mutant embryos was performed by intragastric (i. g.) application of tamoxifen in pregnant cre- mothers after breeding with cre+ males at E8.5, E9.5 and E10.5.

Deletion in postnatal development:

To induce postnatal genetic deletion in Smad6, Smad7 and Smad6/7IECKO mice, littermates of control and mutant animals were injected intraperitoneally (i.p.) with TAM-OH at P2, P3 and P5.

Deletion in adult:

To induce adult genetic deletion in Smad6, Smad7 and Smad6/7IECKO mice, littermates of control and mutant animals were fed Tamoxifen-containing Food over a period of 2 weeks with a 2 weeks washout period before experimental procedure.

6.1.5 Cell Culture

6.1.5.1 HUVEC culture

HUVEC were obtained from Promocell and cultured in Endopan-3 medium supplemented with the growth factor kit from PAN Biotech GmbH (Aidenbach, Germany). HUVEC were used up until passage six and passaged at 80-90% confluency by washing with PBS and detachment by Trypsin-EDTA incubation at 37°C for 2 min. Culture medium was added to neutralize Trypsin-EDTA and the cells were centrifuged for 5 min at 200 g. For experiments, HUVEC were used between passage one and three. For lentiviral transfection $1.5x10^5$ cells were plated into each well of a 6-well plate and further processed according to 5.1.5.5.

6.1.5.2 B-PC culture

Primary human brain pericytes (B-PCs) were obtained from ScienCell Research Laboratories (San Diego, US) and cultured in Pericyte medium supplemented with 2% FCS, 1% Pericyte Growth Supplement and 1% Penicillin-Streptomycin. Pericytes were used up until passage five and passaged at 80-90% confluency by washing with PBS and detachment by Trypsin-EDTA incubation at 37°C for 2 min. Culture medium was added to neutralize Trypsin-EDTA and the cells were centrifuged for 5 min at 200 g.

6.1.5.3 3D Spheroid Culture

B-PCs and transfected HUVEC were detached by Trypsin-EDTA incubation at 37°C for 2 min and counted with a Countess Cell Counter (Thermo Fischer, Waltham, US). Drops containing 1.500 cells per cell line (3.000 total) in 20% methocel were placed on a square cell culture dish lid using a multi-channel pipette and cultured as hanging drops. Aggregates were incubated for 24h at 37°C and 5% CO2. For imaging, spheroids were fixed for 10 min in 4% PFA, incubated in permeabilization/blocking buffer for 1 h and stained with PDGFRb-PE and Hoechst. For EdU analysis, EdU was added to a final concentration of 0.01mM to the medium prior to spheroid assembly. After resuspension in accutase, single cell suspension was processed according to the Click-IT™ EdU Alexa 647 Flow Cytometry Assay

Kit (Thermo Fischer, Waltham, US) Protocol. For flow cytometry, cells were additionally stained for CD31-Alexa 488 and PDGFRb-PE.

6.1.5.4   LLC cell culture

LLC were obtained from ATCC. The cells were cultured in DMEM high glucose (Gibco) supplemented with 10% FCS, 1% penicillin/streptomycin (Sigma Aldrich, US) and 1% non-essential amino acid (Gibco). Cells were passaged at 60-70% confluency and were washed with PBS and detached by Trypsin-EDTA incubation at 37°C for 2 min. Next, culture medium was added to neutralize Trypsin-EDTA and the cells were centrifuged for 5 min at 200 g. The supernatant was discarded, the pellet was resuspended in culture medium and the desired cell dilutions (1: 10) were prepared. For in vivo injection, cells were used at 60-70% confluency to ensure proliferative activity.

6.1.5.5   B16F10 cell culture

B16F10 were obtained from Caliper life sciences. Cells were cultured in DMEM high glucose (Gibco) supplemented with 10% FCS, 1% penicillin/streptomycin (Sigma Aldrich, US) and 1% non-essential amino acid (Gibco). Cell were passaged at 60-70% confluency and were washed with PBS and detached by Trypsin-EDTA incubation at 37°C for 2 min. Next, culture medium was added to neutralize Trypsin-EDTA and the cells were centrifuged for 5 min at 200 g. The supernatant was discarded, the pellet was resuspended in culture medium and the desired cell dilutions (1: 10) were prepared. For in vivo injection, cell were used at 60-70% confluency to ensure proliferative activity.

6.1.5.6   Lentiviral production

HEK239T obtained from ATCC were used for lentiviral production. HEK239T were transfected with 21ug of gene construct (GIPZ_nsh, sh115, sh118, sh699, sh137, TurboRFP, TurboGFP) (Horizon Discovery, UK), 14ug envelope plasmid pMD2.G, 21ug packaging plasmid psPAX2 and PEI solution (Addgene). Transfected cells were kept for 48h and 72h. Supernatant was collected at each time point, filtered through a 0.45um filter and stored at 4°C. After 72h supernatant was either centrifuged in an ultracentrifuge at 800.000g for 2h at 4°C or virus was precipitated using PEG-it Lentiviral concentrator according to the manufacturer's protocol and pellet was dissolved in PBS. 10ul or 50ul aliquots were stored under S2 condition at -80°C until use.

6.1.5.7   Lentiviral transduction

HUVEC were transfected with lentiviral particles expressing shRNA constructs to generate knockdown of *SMAD6*, *SMAD7* or *SMAD6/7*. To select stably transfected cells, puromycin (1µg/ml) or

neomycin (200µg/ml) (Thermo Fischer Scientific) depending on the selection cassette was used. GFP or RFP expression was used to confirm successful selection.

6.2 Mouse experimentation

6.2.1 Tumor implantation

Experimental metastasis: $3x10^5$ LLC or $3x10^5$ B16F10 melanoma cells were injected intravenously (i.v.) into 8-10 weeks old male Smad6, Smad7 *and* Smad6/7IECKO mice. Two weeks post tumor cell injection, mice were sacrificed, and lung samples were collected for further analysis. All mice were regularly monitored for endpoint criteria (2-3 times per week, daily when >10% weight loss).

Primary tumor and resection metastasis:

$1x10^6$ LLC or $1x10^6$ B16F10 melanoma cells were inoculated subcutaneously (s. c.) into 8–10-week-old male Smad6, Smad7 and Smad6/7IECKO mice. Two weeks post tumor implantation, mice were either sacrificed, and primary tumors samples were collected, or kept until spontaneous metastasis formation up to 65 days and analyzed for survival. All mice were regularly monitored for humane endpoint criteria (2-3 times per week, daily when >10% weight loss). Tumor volumes were measured with a digital caliper and tumor volumes were calculated using the following formula: volume = (length x width x height) / 2.

6.2.2 Embryo Preparation

Mothers (cre-) were set up with fathers (cre+) in timed matings and daily plug check was performed. Upon plug detection, breeders were separated and time until E10.5, E13.5 and E.18.5 was calculated. Mothers were sacrificed at defined timepoints, and the two uterine horns were collected. Embryos were carefully removed from the uterus and the amniotic sac, imaged, and placed into PFA for further processing.

6.2.3 Retina Preparation

Retina was isolated according to the published protocol (230) (see Figure 9B). Isolated retina was placed into 100% Methanol until further processing.

6.3 Molecular biology methods

6.3.1 Genotyping PCR

Genotyping from mouse tissue was performed by PCR of genomic DNA. Tail tips were incubated in 90μL Direct PCR Reagent + 10μg Proteinase K at 55°C overnight followed by 30 min at 95°C for enzyme inactivation. Tail tip lysates were used directly or were stored at -20°C until genotyped. Genotyping was performed using the Taq polymerase kit (Qiagen). The PCR reaction was run with an Applied Biosystems thermocycler and analyzed with the QIAxcel Advanced system according to the manufacturer's instructions.

Table 18 Smad6$^{fl/fl}$ genotyping PCR mix and program

Smad6$^{fl/fl}$ genotyping PCR mix		*Genotyping PCR Program*		
	1x (μL)	**Step**	**Temperature**	**Time**
dd H2O	11,50	1	94ºC	5'
5x Q-Solution	3,00	2	94ºC	15''
10X Buffer	2,25	3	65°C	30'' decrease 1°C/cycle
MgCl2	0,75	4	72ºC	40''
dNTP	0,75		**Go to step 2 for 10 cycles**	
CSD-Smad6-F (10pmol/μL)	0,75	5	94ºC	15''
CSD-Smad6-R (10pmol/μL)	0,4	6	55ºC	30''
CSD-Smad6-ttR	0.4	7	72ºC	40'
Taq (5 U/μl)	0,2		**Go to step 2 for 30 cycles**	
DNA	1	8	72ºC	5'
		9	10ºC	hold

Table 19 Smad7$^{fl/fl}$ genotyping PCR mix and program

Smad7$^{fl/fl}$ genotyping PCR mix		*Genotyping PCR Program*		
	1x (μL)	Step	Temperature	Time
dd H2O	10,1	1	94ºC	2'

		Step	Temperature	Time	
5x Q-Solution	4,00	2	94ºC	20''	
10X Buffer	2,0	3	65°C	15'' decrease 0.5°C/cycle	
MgCl2	1,0	4	72ºC	10''	
dNTP	1,6		**Go to step 2 for 10 cycles**		
Smad7 F (10pmol/µL)	0,4	5	94ºC	15''	
Smad6 R (10pmol/µL)	0,4	6	60ºC	15''	
		7	72ºC	10'	
Taq (5 U/µl)	0,1		**Go to step 6 for 28 cycles**		
DNA	1	8	72ºC	2'	
		9	10ºC	hold	

Table 20 Cdh5-CreERT2 genotyping PCR mix and program

Cdh5-CreERT2 genotyping PCR mix		**Genotyping PCR Program**			
	1x	Step	Temperature	Time	
dd H2O	15.1 µL	1	94°C	2'	
10x Buffer	2 µL	2	94°C	30''	x35
MgCl2	0.8 µL	3	58°C	45''	
dNTP's	0.4 µL	4	72°C	2'	
MB182R Actin (10µM)	0.4 µL	5	72°C	2'	
MB182R Actin (10µM)	0.4 µL	6	4°C	hold	
MB183R Cre (10µM)	0.4 µL				
MB183F Cre (10µM)	0.4 µL				
Taq	0.1 µL				
DNA	1 µL				

6.3.2 RNA Isolation

RNA isolation on sorted EC was performed with the Arcturus™ PicoPure™ RNA isolation Kit (Thermo Fisher Scientific, KIT0204). Sorted cells were centrifuged at 500 g and 4°C for 8 min to form a pellet which was then lysed by 100 µL Arcturus PicoPure extraction buffer. The protocol was performed

according to manufacturer's instructions. RNA was eluted in 12µL RNase free H2O and concentration was measured via NanoPhotometer® N60. The RNA was stored at -80°C.

6.3.2.1   cDNA synthesis

cDNA generation was carried out using the Quantitect® Reverse Transcription Kit (Qiagen) according to manufacturer's instructions. Template RNA was thawed on ice and 1 µg RNA was incubated with 2 µL x DNA Wipeout buffer for 2min at 42°C and the total volume was adjusted to 14 µL adding RNase-free H2O. The mixture was further incubated with 1 µL reverse transcriptase, 4 µL 5xRT-buffer and 1 µL RT Primer mix at 42°C for 30min for reverse transcription and 95°C for 3min for inactivation of the enzyme. The cDNA was diluted 1:10 in H2O for qPCR reaction. cDNA was kept in -20°C for short term storage.

6.3.2.2   Quantitative Real Time-PCR (RT-qPCR)

Relative gene expression was quantified by RT-qPCR based on synthesized cDNA. RT-qPCR was performed by using the synthesized cDNA with TaqMan Fast Advanced Mastermix (Life Technologies) and TaqMan probes (Applied Biosciences) on a StepOnePlus Real-Time PCR System (Thermo Fisher Scientific). Each reaction was performed in triplicates.

Table 21 TaqMan^{TM} RT-qPCR reaction mix

TaqMan^{TM} RT-qPCR reaction mix	
cDNA (1:10 dilution)	2 µL
Taqman^{TM} Fast Advanced Master Mix	5 µL
TaqMan^{TM} probe	0.2 µL
ddH$_2$O	2.8 µL

Table 22 TaqMan^{TM} RT-qPCR program

TaqMan^{TM} RT-qPCR program		
Step	Temperature (°C)	Time (sec)
Pre-denaturation	95	30
Denaturation	95	2
Amplification	60	20

For analysis, the ΔΔCt method was applied as described in literature[231]. This is done by normalizing CT values of the genes of interest to the CT values of the housekeeping gene for each sample (ΔCT).

$$\Delta CT = CT_{\text{gene of interest}} - CT_{\text{housekeeping gene}}$$

The normalized CT valued were then further normalized to CT values of control samples (ΔΔCT).

$$\Delta\Delta CT = \Delta CT_{sample\ of\ interest} - \Delta CT_{control\ sample}$$

Respective fold changes were calculated from the ΔΔCT values.

$$Fold\ change = 2^{-\Delta\Delta CT}$$

6.3.3 Mass Spectrometry

Sample preparation for mass spectrometric analysis and LC-MS/MS measurements were performed by the Department of Systems Biology and Signal Transduction of the DKFZ. Proteomics data processing was conducted by Genevia Technologies, and data analysis was conducted with support of Genevia Technologies. Heatmaps and Dotplots (GSEA and ORA) were generated by Genevia Technologies.

Ctrl, Smad6-, Smad7- and Smad6/7KD HUVEC monocultures were washed with ice-cold PBS and harvested using a scraper. Proteins were extracted from cell pellets with modified protein lysis buffer and prepared for mass spectrometric analysis, following an adapted version of the automated single-pot, solid-phase-enhanced sample preparation (SP3-protocol) (232) on the Bravo Liquid Handling Platform (Agilent). In total, 5 µg of total protein per sample of KD-HUVEC were used. After reduction of disulfide bridges using 40mM Tris(2-carboxyethyl)phosphine (TCEP) and carbamidomethylation with 10mM chloroacetamide (CAA) at 95°C for 5 min, the proteins were digested with trypsin (Trypsin Gold, Promega) with an enzyme to protein ratio of 1:25 in 100 mM tetraethylammonium bromide (TEAB) overnight at 37°C. The resulting peptides were recovered with the help of magnetic beads (Sera-Mag Speed Beads, GE Healthcare), then dried down by vacuum centrifugation. Before LC-MS/MS measurement, the dried samples were resuspended in 15µL of MS loading buffer.

6.3.4 LC-MS/MS measurements

Nano-flow LC-MS/MS was performed by coupling an Ultimate 3000 HPLC (Thermo Fisher Scientific) to an Orbitrap Eclipse mass spectrometer (Thermo Fisher Scientific). 2µL were injected first to a Acclaim™ PepMap™ 100 C18 5µm 0.3mmx5mm trapping column (precolumn) (Thermo Fischer Scientific), then eluted from the 75 µm × 30 cm analytical column packed in-house with Reprosil-Pur 120 C18-AQ, 1.9 µm resin (Dr. Maisch) with a flow rate of 0.3µL/min, using a linear gradient of 1.6% to 30.4% acetonitrile over 120min and a finale elution step of 5min with 80% acetonitrile. The mass spectrometer was operated in data-dependent acquisition mode. MS1 spectra were acquired at a

Methods

resolution of 120,000 with a mass range of 380–1400 m/z. For MS2 scans, the top 20 precursors were isolated and fragmented using higher-energy c-trap dissociation (HCD) with a resolution of 15,000.

Samples from HUVEC cells (human). Sample table:

FP sample_name	cell_line	cell_type	condition	replicate
Gipz S6 sh118 + S7 115-1_FP_rep1	HUVEC	Endothelial cell	Smad6KD + Smad7KD	1
Gipz S6 sh118 + S7 115-2_FP_rep2	HUVEC	Endothelial cell	Smad6KD + Smad7KD	2
Gipz S6 sh118 + S7 115-3_FP_rep3	HUVEC	Endothelial cell	Smad6KD + Smad7KD	3
Gipz S6 sh118-1_FP_rep1	HUVEC	Endothelial cell	Smad6KD	1
Gipz S6 sh118-2_FP_rep2	HUVEC	Endothelial cell	Smad6KD	2
Gipz S6 sh118-3_FP_rep3	HUVEC	Endothelial cell	Smad6KD	3
Gipz S7 sh115-1_FP_rep1	HUVEC	Endothelial cell	Smad7KD	1
Gipz S7 sh115-2_FP_rep2	HUVEC	Endothelial cell	Smad7KD	2
Gipz S7 sh115-3_FP_rep3	HUVEC	Endothelial cell	Smad7KD	3
nsh1_FP_rep1	HUVEC	Endothelial cell	WT	1
nsh2_FP_rep2	HUVEC	Endothelial cell	WT	2
nsh3_FP_rep3	HUVEC	Endothelial cell	WT	3

6.3.4.1   Pre-processing and exploratory analysis

Raw MaxQuant output data (LFQ intensity values) was first processed with Proteus v0.2.16 (233). The dataset across all samples contained 4598 proteins in total. Next, median normalisation was performed using the *normalizeData* function. *plotSampleDistributions* function was used for assessing data distribution before and after the normalisation. Exploratory analysis was carried out to inspect replicate concordance using Pairwise Pearson's correlation visualised with the package pheatmap v.1.0.12 and Principal Component Analysis (PCA) using the function *plotPCA* with default parameters. One sample, HUVEC wild type replicate 1 (nsh1_FP_rep1), was flagged as an outlier.

As the next step, missing value rates in the data were investigated. Overall missing value rates were visualised using a custom R script (Genevia Technologies) based on the *plot_missval* function of R package DEP v.1.20.0. This further confirmed the higher dropout rates in the above flagged sample. Therefore, HUVEC wild type replicate 1 (nsh1_FP_rep1), was removed from downstream analysis.

The data was further filtered based on quantification rate using *selectGroups* function keeping proteins with at least 70% quantification rate in two or more conditions. This threshold retained 4203 proteins for further analysis. Importantly, the data loss was <10% of all proteins initially detected. The non-imputed data matrix was further inspected using PCA and the data retained sufficiently good sample similarity within conditions. Random imputation was therefore not performed.

6.3.4.2   Differential expression analysis

Differential expression (DE) analysis was performed using the *limmaDE* wrapper function of the Proteus package. It calls the limma R package (234) and is designed for performing stable and robust differential expression of data with gaps, thus avoiding the need for random imputation. The following 3 contrasts were designed:

Contrast	Reference sample
Smad6KD	WT
Smad7KD	WT
Smad6KD + Smad7KD	WT

Proteins were called significantly DE if adjusted p-value was < 0.05 and absolute log2FC > 0.585 (corresponding to at least 1.5-fold up- or down-regulation). P-value distributions for each contrast

were inspected using the *plotPdist* function. DE proteins were visualised with heatmaps using the ggplot2 R package.

6.3.5   Bulk RNA sequencing

Lung and liver EC from Smad6-, Smad7 and Smad6/7iECKO mice were FACS-sorted and total RNA was isolated using Arcturus PicoPure RNA isolation kit (Thermo Fisher Scientific) according to the manufacturer's protocol. RNA concentration was measured using the Qubit high-sensitivity RNA Quantification Assay (Thermo Fischer Scientific) on a Qubit Flurorometer (Thermo Fischer Scientific). Samples were prepared and brought to the Genomics & Proteomics Core Facility of the DKFZ for RNA sequencing. Sequencing and library preparation was performed by the Genomics & Proteomics Core Facility of the DKFZ. Libraries were prepared using SMARTer Ultra Low RNA v4 Kit (Clontech) with 10 ng of base material and sequenced on Novaseq 6000 S1 (single-end, 50bp read length). RNA-seq data processing was conducted by Genevia Technologies and data analysis was conducted with support of Genevia Technologies. Heatmaps and Dotplots (GSEA and ORA) were generated by Genevia Technologies.

6.3.5.1   RNA-seq data pre-processing and alignment

The raw FASTQ files were first subjected to quality control and pre-processing using fastp v0.23.1 and MultiQC v2.3 (237). Quality trimming was performed with default criteria (Phred >Q15, min read length 15 bp). Trimmed RNA-seq reads were aligned to the mouse reference genome mm10 using STAR v2.7.10a (238). Duplicate-marked and sorted alignment files were used for gene counting. Gene-level read counts were obtained using htseq-count v2.0.1 (239) with the transcriptome annotation GTF file version GRCm38.96.

6.3.5.2   RNA-seq data differential expression analysis

Replicate concordance and technical variation levels were assessed by principal component analysis (PCA). The count matrix was transformed using the VST method in the DESeq2 R package (240) and PCA was computed using top 1000 most variable genes. In order to identify outliers, the distance of each sample from the median on each principal component, using the R package bigutilsr was determined. Samples with a distance larger than 6 units to the median absolute distance (MED) were flagged as outliers and excluded from downstream analysis.

Differential expression analysis (DEA) was performed using the DESeq2 R package. Prior to the analysis, the full data matrix was filtered to include genes with a minimum of total 5 raw counts

across samples. DE contrasts were defined as IECKO vs WT, and the default Wald test used for hypothesis testing to compare the two groups. Significant DE genes were defined post-hoc using the following thresholds: BH-adjusted p-value < 0.05 and absolute log2FC > 0.58.

For visualizations, heatmaps were generated clustering both samples (columns) and DE genes (rows) using Euclidean distance with the 'Ward.D' clustering method with pheatmap.

6.3.5.3 RNA-seq data pathway enrichment analysis

In order to identify whether the differences in overall gene expression represent a functionally coherent set of genes corresponding to an annotated pathway or ontology gene set enrichment analysis (GSEA) using the R package clusterProfiler was performed (241). Pathways from the Hallmark collection from MSigDB were tested, calculating the normalized enrichment score (NES) and subsequently estimating the false discovery rate (FDR) given as adjusted p-valus (p-adj). Visualizations for GSEA include a barplot with the top enriched (NES > 0 and p-adj < 0.05) or depleted terms (NES < 0 and p-adj < 0.05) as well as GSEA plots.

To query the differentially expressed genes across different pathway databases, over-representation analysis (ORA) was used. In this analysis the GO database and specifically the Biological Processes (BP), Molecular Function (MF), and Cellular Component (CC) ontologies is considered. ORA results were visualised using cnetplots and dotplots.

6.4 Tissue staining

6.4.1 Preparation of cryoblocks and cryosections

Tissues and tumors were harvested and embedded in TissueTek O.C.T. compound (Sakura) on dry ice. Samples were stored at -80°C. The cryomicrotome Hyrax C50 (Zeiss) was used to cut 5-7 µm cryosections. Sections were dried for 10 min at RT and stored at -80°C.

6.4.2 Preparation of paraffin blocks and paraffin sections

Tissues and tumors were fixed in PFA over night at 4 °C. Next day, samples were washed with VE-water and further processed with the spin tissue processor STP120. Automated steps included incubations in a graded ethanol series (70-85-96 %), isopropanol, xylol and paraffin. Following

dehydration, samples were manually embedded in paraffin blocks. 7-10µm sections were cut using the rotary microtome HM355S.

6.4.3 Immunofluorescence

Cryosections were fixed in ice-cold 100% methanol (-20°C) for 10 min. Paraffin sections were dewaxed and rehydrated by consecutive incubations in a graded ethanol series, washed two times in VE-water and incubated in 20ng/µL of Proteinase K (Gerbu) in TE-buffer pH 8.0 for 5 min at 37°C. Afterwards, sections were washed and blocked in 10% ready-to-use normal goat serum (Life Technologies) for 1h. The primary antibody was incubated overnight at 4°C. After primary antibody incubations, the sections were washed three times in TBS-T for 5 min each and incubated with the secondary antibodies for 1h at RT. Next, sections were washed three times with TBS-T for 5 min. Afterwards, Hoechst staining (1:5000, Merck) was performed and sections were mounted with DAKO mounting medium (Agilent).

6.4.4 Histochemistry

6.4.4.1 Hematoxylin and eosin staining

Paraffin sections were dewaxed and rehydrated by consecutive incubations in a graded ethanol series. Afterwards, slides were washed two times in VE-water and incubated in freshly filtered hemalaun for 4 min, washed with running tap water for 10 min, washed in VE-water and stained with 1% ethanoic eosin for 2 min. Following three times of washing with VE-water, sections were dehydrated by dipping them into graded ethanol series (70%-80%-99%), isopropanol and xylol. Slides were mounted with Histomount and whole area bright field images were acquired with the Zeiss Axio ScanZ.1.

6.4.5 Tissue pathology

H&E stainings of tumor tissue were sent to a board-certified pathologist for analysis (C. Mogler, Institute of General and Surgical Pathology, TUM, Munich, Germany). For Masson's Trichrome staining, paraffin-blocks were sent to C. Mogler. Processing and scoring was performed by M. Tulessin (Institute of General and Surgical Pathology, TUM, Munich, Germany) using Masson Trichrome Staining Kit (Sigma-Aldrich, HT15) according to the manufacter's protocol.

6.4.6 Image acquisition and analysis

Fluorescent images were acquired via Zeiss Axio Scan or LSM 780 SD at the imaging core facility of the DFKZ. Image analysis was performed with Ilastik (Version 1.0, EMBL, Heidelberg)(242) and Fiji (Version 2.14, ImageJ2)(243).

6.5 Biochemistry methods

6.5.1 Fluorescence activated cell sorting (FACS)

To isolate EC, tissue and tumors were enzymatically digested according to the table 21 in DMEM/F12 media at 37°C for 30min. Tissue lysates were passed through an 18G cannula syringes and incubated another 15 min at 37°C. Tissue lysates were passed through a 19G cannula syringes and further filtered through 100µM filters. To lyse erythrocytes, the tissue lysates were incubated with ammonium chloride potassium (ACK) lysis buffer for 5 min and the cell suspension was subsequently washed with PBS/5% FCS. Next, positive selection using CD31 microbeads (Miltenyi Biotec) was performed to enrich the EC according to the manufacturer's protocol. Endothelial cells were further FACS sorted for the surface marker profile CD45-/LYVE1-/PDPN-/TER-119-/CD31+ using the antibodies listed in table 7. To exclude dead cells, the cells were stained with FxCycle. Cell populations were sorted using FACS Aria or Fusion cell sorter in the Flow Cytometry Core Facility of the DKFZ. Single stained and unstained controls were used for compensation and gating strategy. Cells were pre-gated to distinguish debris and doublets using FSC and SSC.

Table 21 Digestion mix for FACS

	Lung	Liver	Tumor
	1x	1x	1x
2% DNAseI	2.5 µL	2.5 µL	2.5 µL
DMEM/F12	4.5 ml	4.5 ml	4.5 ml
Liberase (2mg/ml)	0.5 mL	0.5 mL	0.5 mL

6.6 Statistical analysis

GraphPad Prism 8 (GraphPad Software Inc.) was used for statistical analysis. Data are shown as mean ±SD or mean±SEM. Statistical significance was determined by two-tailed Student's t-test, Mann-

Whitney U test or Two-way ANOVA as indicated in figure legends. P-values ≤0.05 were considered statistically significant. *P<0.05, ** P<0.01 and ***P<0.001

7 Abbreviations

2-SHG	2-hydroxyglutarate
aCAP	aerocytes
ACK	ammonium-chloride-potassium
ACVR	activin A receptor
AKT	proteinkinase B
ALK	activin receptor-like kinase
AMD	age-related Macular Degeneration
AMIS	apical membrane initiation site
ANG	angiopoetin
AVM	arteriovenous malformations
bAVM	brain arteriovenous malformations
BBB	blood brain barrier
BMP	bone morphogenetic protein
BP	biological processes
B-PC	brain pericytes
BW	body weight
CAA	chloroacetamide
CC	cellular components
cCasp3	cleaved-caspase 3
CD31	cluster of diffentiation 31
CHX	cyclohexamide
COVID-19	coronavirus disease 2019
CT	cycle threshold
Ctrl	control
CXCL	cxc motif chemokine ligand 1
DEA	differential expression analysis
DEG	differentially expressed genes
DKFZ	german cancer research center
DLL	delta like canonical notch ligand
DMSO	dimehtyl sulfoxide
DNA	deoxyribonucleic acid
DR	diabetic retinopathy
DSS	disturbed shear stress
E	embryonic day
EC	endothelial cell
ECM	extracellular matrix
EDTA	ethylenediaminetetraacetic acid
EdU	5-ethynyl-2'-deoxyuridine
EMT	epithelial-mesenchymal transition
EndoMT	endothelial-mesenchymal transition
ENG	endoglin
EPHB	ephrin B
ERG	erythroblast transformation- specific

Abbreviations

ERK	extracellular- signal regulated kinases
ES-cells	embryonic stem cells
ET-1	endothelin 1
ETS	erythroblast transformation specific
ETV2	ETS variant transcription factor 1
F	forward
FACS	fluorescent activated cell sorting
FC	fold change
FCS	fetal calf serum
FDR	false discovery rate
FGF	fibroblast growth factor
FLT	fms-related tyrosine kinase
FOXO	forkhead box protein O3
FP	full proteome
FSC	forward scatter
gCAP	general capillary
GO	gene ontology
GSEA	gene set enrichment analysis
HCC	hepatocellular carcinoma
HCD	higher-energy c-trap dissociation
HHT	hereditary hemorrhagic telangiectasia
HIF	hypoxia-inducible factor
HUVEC	human umbilical vein endothelial cells
i.p.	intraperitoneal
i.v.	intravenous
IB4	isolectin B4
ICAM	intercellular cell adhesion molecule
ICI	immune checkpoint inhibitor
IECKO	inducible-endothelial specific knock out
IgG	immunoglobulin G
IPA	ingenuity pathway analysis
iSMAD	inhibitory mothers against decapentaplegic homolog
JAG	jagged
JPHT	juveline polyposis-HHT
KD	knock down
KLF	krüppel-like factors
KO	knock out
L2FC	log 2 fold change
LAMB	laminin beta 1
LEC	lung endothelial cell
LLC	lews lung cancer
Lox	locus of X(cross)-over
LRG	leucine-rich alpha-2 glycoprotein
LSEC	liver sinusoidal endothelial cell
LSS	laminar shear stress
Lyve	lympathic vessel endothelial hyaluronan receptor

Abbreviations

MAP	mitogen-activating protein
MMP	matrix metalloproteinase
MF	molecular function
NES	normalized enrichment score
NfkB	nuclear factor kappa B subunit
NO	nitric oxide
NOTCH	neurogenic locus notch homolog protein
NR2F2 (COUP-TFII)	nuclear receptor subfamily 2
NRP	neuropilin
NV	neovascularization
ORA	over-representation analysis
ORR	overall response rate
OS	overall survival
P	postnatal day
Padj	adjusted p value
PAH	pulmonary arterial hypertension
PBS	phosphate buffered saline
PC	pericyte
PCA	principal component analysis
PCR	polymerase chain reaction
PD	programmed death
PDGF	platelet-derived growth factors
PDGFR	platelet-derived growth fator receptor
PDL	programmed death—ligand
PDPN	podoplanin
PECAM	endothelial cell adhesion molecule
PFKFB	6-phosphofructo-2-kinase/fructose-2,6-biphosphatase 3
PFS	progression-free survival
PI3K	phosphoinositide 3-kinases
Piezo1	piezo type mechanosensitive ion channel component 1
PKC	proteinkinase C
PLXND	plexin
POSTN	periostatin
PTGS	prostaglandin-endoperoxide synthase
R	reverse
RNA	ribonucleic acid
ROCK	rho-associated protein kinase
ROP	retinopathy of Prematurity
RT-qPCR	quantitative reverse transcription polymerase chain
s.c.	sub-cutaneous
S1pr2	sphingosine-1-phosphate receptor 2
SEMA	semaphoring
shRNA	small hairpin RNA
SIRT	sirtuin
SMAD	mothers against depapentaplegic homolog
SMC	smooth muscle cell

Abbreviations

SMURF	human SMAD specific E3 ubiquitin ligase
SSC	side scatter
STAT	signal transducers and activators of transcription
TAGLN	transgelin
TAM-OH	hydroxytamoxifen
TBS-T	Tris-buffered saline with Tween 20
TCA	trichloroacetic acid
TCEP	Tris(2-carboxyethyl)phosphine
TE	Tris-EDTA
TEAB	tetraethylammonium bromide
TGF	transforming growth factor
TIE	tyrosine kinases with immunoglobulin and epidermal growth factor homology domain
TKI	tyrosine kinase inhibitor
TME	tumor microenvironment
TNF	tumor necrosis factor
VCAM	vascular cell adhesion molecule
VEGF	vascular endothelial growth factor
VEGFR	vascular endothelial growth factor receptor
WT	wildtype
ZEB	zinc finger E-Box binding homeobox 1

8 Bibliography

1.   Kubo H, Alitalo K. The bloody fate of endothelial stem cells. Genes Dev. 2003;17(3):322-9.
2.   Herbert SP, Stainier DY. Molecular control of endothelial cell behaviour during blood vessel morphogenesis. Nat. Rev. Mol. Cell Biol. 2011;12(9):551-64.
3.   Risau W. Mechanisms of angiogenesis. Nature. 1997;386(6626):671-4.
4.   Craig MP, Sumanas S. ETS transcription factors in embryonic vascular development. Angiogenesis. 2016;19(3):275-85.
5.   Ferguson JE, Kelley RW, Patterson C. Mechanisms of endothelial differentiation in embryonic Vasculogenesis. Arterioscler. Thromb. Vasc. Biol. 2005;25(11):2246-54.
6.   Marziano C, Genet G, Hirschi KK. Vascular endothelial cell specification in health and disease. Angiogenesis. 2021;24(2):213-36.
7.   Hong CC, Peterson QP, Hong JY, Peterson RT. Artery/vein specification is governed by opposing phosphatidylinositol-3 kinase and MAP kinase/ERK signaling. Curr. Biol. 2006;16(13):1366-72.
8.   Limaye N, Kangas J, Mendola A, Godfraind C, Schlögel MJ, Helaers R, et al. Somatic Activating PIK3CA mutations cause venous malformation. Am. J. Hum. Gen. 2015;97(6):914-21.
9.   Fang JS, Coon BG, Gillis N, Chen Z, Qiu J, Chittenden TW, et al. Shear-induced Notch-Cx37-p27 axis arrests endothelial cell cycle to enable arterial specification. Nat Commun. 2017;8(1):2149.
10. You LR, Lin FJ, Lee CT, DeMayo FJ, Tsai MJ, Tsai SY. Suppression of Notch signalling by the COUP-TFII transcription factor regulates vein identity. Nature. 2005;435(7038):98-104.
11. Neal A, Nornes S, Payne S, Wallace MD, Fritzsche M, Louphrasitthiphol P, et al. Venous identity requires BMP signalling through ALK3. Nat Commun. 2019;10(1):453.
12. Peacock HM, Tabibian A, Criem N, Caolo V, Hamard L, Deryckere A, et al. Impaired SMAD1/5 Mechanotransduction and Cx37 (Connexin37) expression enable pathological vessel enlargement and shunting. Arterioscler. Thromb. Vasc. Biol. 2020;40(4):e87-e104.
13. Urness LD, Sorensen LK, Li DY. Arteriovenous malformations in mice lacking activin receptor-like kinase-1. Nat. Genet. 2000;26(3):328-31.
14. Banerjee K, Lin Y, Gahn J, Cordero J, Gupta P, Mohamed I, et al. SMAD4 maintains the fluid shear stress set point to protect against arterial-venous malformations. J Clin. Invest. 2023;133(18).
15. Luo W, Garcia-Gonzalez I, Fernández-Chacón M, Casquero-Garcia V, Sanchez-Muñoz MS, Mühleder S, et al. Arterialization requires the timely suppression of cell growth. Nature. 2021;589(7842):437-41.
16. Park H, Furtado J, Poulet M, Chung M, Yun S, Lee S, et al. Defective Flow-Migration Coupling causes arteriovenous malformations in hereditary hemorrhagic telangiectasia. Circulation. 2021;144(10):805-22.
17. Trimm E, Red-Horse K. Vascular endothelial cell development and diversity. Nat. Rev. Cardiol. 2023;20(3):197-210.
18. Ruter DL, Liu Z, Ngo KM, X S, Marvin A, Buglak DB, et al. SMAD6 transduces endothelial cell flow responses required for blood vessel homeostasis. Angiogenesis. 2021;24(2):387-98.
19. Fraisl P, Mazzone M, Schmidt T, Carmeliet P. Regulation of angiogenesis by oxygen and metabolism. Dev. Cell. 2009;16(2):167-79.
20. Blanco R, Gerhardt H. VEGF and Notch in tip and stalk cell selection. Cold Spring Harb. perspect. Med. 2013;3(1):a006569.
21. Mouillesseaux KP, Wiley DS, Saunders LM, Wylie LA, Kushner EJ, Chong DC, et al. Notch regulates BMP responsiveness and lateral branching in vessel networks via SMAD6. Nature Communications. 2016;7(1):13247.

22. Benn A, Hiepen C, Osterland M, Schütte C, Zwijsen A, Knaus P. Role of bone morphogenetic proteins in sprouting angiogenesis: differential BMP receptor-dependent signaling pathways balance stalk vs. tip cell competence. FASEB. 2017;31(11):4720-33.

23. Aspalter IM, Gordon E, Dubrac A, Ragab A, Narloch J, Vizán P, et al. Alk1 and Alk5 inhibition by Nrp1 controls vascular sprouting downstream of Notch. Nat. Commun. 2015;6(1):7264.

24. Ranade SS, Qiu Z, Woo S-H, Hur SS, Murthy SE, Cahalan SM, et al. Piezo1, a mechanically activated ion channel, is required for vascular development in mice. 2014;111(28):10347-52.

25. Korn C, Augustin HG. Mechanisms of vessel pruning and regression. Dev. Cell. 2015;34(1):5-17.

26. Meeson A, Palmer M, Calfon M, Lang R. A relationship between apoptosis and flow during programmed capillary regression is revealed by vital analysis. Development. 1996;122(12):3929-38.

27. Kurz H, Burri PH, Djonov VG. Angiogenesis and Vascular Remodeling by intussusception: from form to function. News Physiol. Sci. 2003;18(2):65-70.

28. Makanya AN, Hlushchuk R, Djonov VG. Intussusceptive angiogenesis and its role in vascular morphogenesis, patterning, and remodeling. Angiogenesis. 2009;12(2):113-23.

29. Lobov IB, Rao S, Carroll TJ, Vallance JE, Ito M, Ondr JK, et al. WNT7b mediates macrophage-induced programmed cell death in patterning of the vasculature. Nature. 2005;437(7057):417-21.

30. Schwartz MA, Vestweber D, Simons M. A unifying concept in vascular health and disease. Science. 2018;360(6386):270-1.

31. Vion AC, Alt S, Klaus-Bergmann A, Szymborska A, Zheng T, Perovic T, et al. Primary cilia sensitize endothelial cells to BMP and prevent excessive vascular regression. J. Cell Biol. 2018;217(5):1651-65.

32. Rochon ER, Menon PG, Roman BL. Alk1 controls arterial endothelial cell migration in lumenized vessels. Development. 2016;143(14):2593-602.

33. Sugden WW, Meissner R, Aegerter-Wilmsen T, Tsaryk R, Leonard EV, Bussmann J, et al. Endoglin controls blood vessel diameter through endothelial cell shape changes in response to haemodynamic cues. Nat. Cell Biol. 2017;19(6):653-65.

34. Kulikauskas MR, X S, Bautch VL. The versatility and paradox of BMP signaling in endothelial cell behaviors and blood vessel function. Cell Mol Life Sci.; 79(2)

35. Humphrey JD, Schwartz MA. Vascular mechanobiology: homeostasis, adaptation, and disease. Annu. Rev. Biomed. Eng. 2021;23:1-27.

36. Liu S, Premont RT, Kontos CD, Huang J, Rockey DC. Endothelin-1 activates endothelial cell nitric-oxide synthase via heterotrimeric G-protein betagamma subunit signaling to protein jinase B/Akt. J. Biol. Chem. 2003;278(50):49929-35.

37. Cardillo C, Kilcoyne CM, Cannon RO, Panza JA. Interactions between nitric oxide and endothelin in the regulation of vascular tone of human resistance vessels. In Vivo. 2000;35(6):1237-41.

38. Ricard N, Bailly S, Guignabert C, Simons M. The quiescent endothelium: signalling pathways regulating organ-specific endothelial normalcy. Nat. Rev. Cardiol. 2021;18(8):565-80.

39. Szymborska A, Gerhardt H. Hold me, but not too tight-endothelial cell-cell junctions in angiogenesis. Cold Spring Harb. Perspect. Biol. 2018;10(8).

40. Baeyens N, Bandyopadhyay C, Coon BG, Yun S, Schwartz MA. Endothelial fluid shear stress sensing in vascular health and disease. J Clin. Invest. 2016;126(3):821-8.

41. Aitken C, Mehta V, Schwartz MA, Tzima E. Mechanisms of endothelial flow sensing. Nat. Cardiovasc. Res. 2023;2(6):517-29.

42. Wang C, Baker BM, Chen CS, Schwartz MA. Endothelial cell sensing of flow direction. Arterioscler. Thromb. Vasc. Biol. 2013;33(9):2130-6.

43. Hahn C, Schwartz MA. Mechanotransduction in vascular physiology and atherogenesis. Nat. Rev. Mol. Cell Biol. 2009;10(1):53-62.

44. Sieve I, Münster-Kühnel AK, Hilfiker-Kleiner D. Regulation and function of endothelial glycocalyx layer in vascular diseases. Vascul. Pharmacol. 2018;100:26-33.

45. Yu J, Bergaya S, Murata T, Alp IF, Bauer MP, Lin MI, et al. Direct evidence for the role of caveolin-1 and caveolae in mechanotransduction and remodeling of blood vessels. J Clin. Invest. 2006;116(5):1284-91.

46. Laux DW, Young S, Donovan JP, Mansfield CJ, Upton PD, Roman BL. Circulating Bmp10 acts through endothelial Alk1 to mediate flow-dependent arterial quiescence. Development. 2013;140(16):3403-12.

47. Huang J, Pu Y, Zhang H, Xie L, He L, Zhang C-L, et al. KLF2 mediates the suppressive effect of laminar flow on vascular calcification by Inhibiting endothelial BMP/SMAD1/5 Signaling. Circ. Res. 2021;129(4):e87-e100.

48. Deng H, Min E, Baeyens N, Coon BG, Hu R, Zhuang ZW, et al. Activation of Smad2/3 signaling by low fluid shear stress mediates artery inward remodeling. Proc. Natl. Acad. Sci. 2021;118(37):e2105339118.

49. Schlereth K, Weichenhan D, Bauer T, Heumann T, Giannakouri E, Lipka D, et al. The transcriptomic and epigenetic map of vascular quiescence in the continuous lung endothelium. eLife. 2018;7.

50. Wilhelm K, Happel K, Eelen G, Schoors S, Oellerich MF, Lim R, et al. FOXO1 couples metabolic activity and growth state in the vascular endothelium. Nature. 2016;529(7585):216-20.

51. Andrade J, Shi C, Costa ASH, Choi J, Kim J, Doddaballapur A, et al. Control of endothelial quiescence by FOXO-regulated metabolites. Nat. Cell Biol. 2021;23(4):413-23.

52. Gomez-Salinero JM, Itkin T, Houghton S, Badwe C, Lin Y, Kalna V, et al. Cooperative ETS transcription factors enforce adult endothelial cell fate and cardiovascular homeostasis. Nat. Cardiovasc. Res. 2022;1(10):882-99.

53. Ricard N, Scott RP, Booth CJ, Velazquez H, Cilfone NA, Baylon JL, et al. Endothelial ERK1/2 signaling maintains integrity of the quiescent endothelium. J. Exp. Med. 2019;216(8):1874-90.

54. Das A, Huang GX, Bonkowski MS, Longchamp A, Li C, Schultz MB, et al. Impairment of an endothelial NAD Signaling Network Is a reversible cause of vascular aging. Cell. 2018;173(1):74-89.e20.

55. Grunewald M, Kumar S, Sharife H, Volinsky E, Gileles-Hillel A, Licht T, et al. Counteracting age-related VEGF signaling insufficiency promotes healthy aging and extends life span. Science. 2021;373.

56. Teichert M, Milde L, Holm A, Stanicek L, Gengenbacher N, Savant S, et al. Pericyte-expressed Tie2 controls angiogenesis and vessel maturation. Nat. Commun. 2017;8:16106.

57. Daneman R, Agalliu D, Zhou L, Kuhnert F, Kuo CJ, Barres BA. Wnt/β-catenin signaling is required for CNS, but not non-CNS, angiogenesis. Proc. Natl. Acad. Sci. 2009;106(2):641-6.

58. Stenman JM, Rajagopal J, Carroll TJ, Ishibashi M, McMahon J, McMahon AP. Canonical Wnt signaling regulates organ-specific assembly and differentiation of CNS vasculature. Science. 2008;322(5905):1247-50.

59. Gastfriend BD, Nishihara H, Canfield SG, Foreman KL, Engelhardt B, Palecek SP, et al. Wnt signaling mediates acquisition of blood–brain barrier properties in naïve endothelium derived from human pluripotent stem cells. eLife. 2021;10:e70992.

60. Liebner S, Corada M, Bangsow T, Babbage J, Taddei A, Czupalla CJ, et al. Wnt/β-catenin signaling controls development of the blood–brain barrier. J. Cell Biol. 2008;183(3):409-17.

61. Gordon L, Blechman J, Shimoni E, Gur D, Anand-Apte B, Levkowitz G. The fenestrae-associated protein Plvap regulates the rate of blood-borne protein passage into the hypophysis. Development. 2019;146(23).

62. Yu QC, Geng A, Preusch CB, Chen Y, Peng G, Xu Y, et al. Activation of Wnt/β-catenin signaling by Zeb1 in endothelial progenitors induces vascular quiescence entry. Cell Rep. 2022;41(8):111694.

63.   Carmeliet P. Angiogenesis in health and disease. Nat. Med. 2003;9(6):653-60.

64.   Ackermann M, Mentzer SJ, Kolb M, Jonigk D. Inflammation and intussusceptive angiogenesis in COVID-19: everything in and out of flow. The European respiratory journal. 2020;56(5).

65.   Cao Y. Adipose tissue angiogenesis as a therapeutic target for obesity and metabolic diseases. Nat. Rev. Drug Discov. 2010;9(2):107-15.

66.   Kim JW, Kong J-S, Lee S, Yoo S-A, Koh JH, Jin J, et al. Angiogenic cytokines can reflect the synovitis severity and treatment response to biologics in rheumatoid arthritis. Exp. Mol. Med. 2020;52(5):843-53.

67.   Folkman J, Merler E, Abernathy C, Williams G. Isolation of a tumor factor responsible for angiogenesis. J. Exp. Med. 1971;133(2):275-88.

68.   Folkman J. Tumor angiogenesis: therapeutic implications. N Engl. J. Med. 1971;285(21):1182-6.

69.   Folkman J, Watson K, Ingber D, Hanahan D. Induction of angiogenesis during the transition from hyperplasia to neoplasia. Nature. 1989;339(6219):58-61.

70.   Hendrix MJC, Seftor EA, Hess AR, Seftor REB. Vasculogenic mimicry and tumour-cell plasticity: lessons from melanoma. Nat. Rev. Cancer. 2003;3(6):411-21.

71.   Liu Z-L, Chen H-H, Zheng L-L, Sun L-P, Shi L. Angiogenic signaling pathways and anti-angiogenic therapy for cancer. Signal Transduct. Target. Ther. 2023;8(1):198.

72.   Yi H, Ye J, Yang XM, Zhang LW, Zhang ZG, Chen YP. High-grade ovarian cancer secreting effective exosomes in tumor angiogenesis. Int. J. Clin. Exp. Pathol. 2015;8(5):5062-70.

73.   Chen S, Chen X, Luo Q, Liu X, Wang X, Cui Z, et al. Retinoblastoma cell-derived exosomes promote angiogenesis of human vesicle endothelial cells through microRNA-92a-3p. Cell Death Dis. 2021;12(7):695.

74.   Tang MKS, Yue PYK, Ip PP, Huang RL, Lai HC, Cheung ANY, et al. Soluble E-cadherin promotes tumor angiogenesis and localizes to exosome surface. Nat. Commun. 2018;9(1):2270.

75.   Lin XJ, Fang JH, Yang XJ, Zhang C, Yuan Y, Zheng L, et al. Hepatocellular carcinoma cell-secreted exosomal microRNA-210 promotes angiogenesis in vitro and in vivo. Mol. Ther. Nucleic acids. 2018;11:243-52.

76.   Garcia J, Hurwitz HI, Sandler AB, Miles D, Coleman RL, Deurloo R, et al. Bevacizumab (Avastin) in cancer treatment: A review of 15 years of clinical experience and future outlook. Cancer Treat. Rev. 2020;86.

77.   Jain RK. Antiangiogenesis strategies revisited: from starving tumors to alleviating hypoxia. Cancer Cell. 2014;26(5):605-22.

78.   Jain RK. Normalization of tumor vasculature: an emerging concept in antiangiogenic therapy. Science. 2005;307(5706):58-62.

79.   Park JS, Kim IK, Han S, Park I, Kim C, Bae J, et al. Normalization of tumor vessels by Tie2 activation and Ang2 inhibition enhances drug delivery and produces a favorable tumor microenvironment. Cancer Cell. 2016;30(6):953-67.

80.   Dasari A, Lonardi S, Garcia-Carbonero R, Elez E, Yoshino T, Sobrero A, et al. Fruquintinib versus placebo in patients with refractory metastatic colorectal cancer (FRESCO-2): an international, multicentre, randomised, double-blind, phase 3 study. The Lancet. 2023;402(10395):41-53.

81.   Lee WS, Yang H, Chon HJ, Kim C. Combination of anti-angiogenic therapy and immune checkpoint blockade normalizes vascular-immune crosstalk to potentiate cancer immunity. Exp. Mol. Med. 2020;52(9):1475-85.

82.   Zheng X, Fang Z, Liu X, Deng S, Zhou P, Wang X, et al. Increased vessel perfusion predicts the efficacy of immune checkpoint blockade. J Clin. Invest. 2018;128(5):2104-15.

83.   Wang-Bishop L, Kimmel BR, Ngwa VM, Madden MZ, Baljon JJ, Florian DC, et al. STING-activating nanoparticles normalize the vascular-immune interface to potentiate cancer immunotherapy. Sci. Immunol. 2023;8(83):eadd1153.

Bibliography

84. Yang H, Lee WS, Kong SJ, Kim CG, Kim JH, Chang SK, et al. STING activation reprograms tumor vasculatures and synergizes with VEGFR2 blockade. J Clin. Invest. 2019;129(10):4350-64.

85. Cheng A-L, Qin S, Ikeda M, Galle PR, Ducreux M, Kim T-Y, et al. Updated efficacy and safety data from IMbrave150: Atezolizumab plus bevacizumab vs. sorafenib for unresectable hepatocellular carcinoma. J. Hepatol. 2022;76(4):862-73.

86. Ren Z, Xu J, Bai Y, Xu A, Cang S, Du C, et al. Sintilimab plus a bevacizumab biosimilar (IBI305) versus sorafenib in unresectable hepatocellular carcinoma (ORIENT-32): a randomised, open-label, phase 2-3 study. The Lancet Oncol. 2021;22(7):977-90.

87. Kalna V, Yang Y, Peghaire CR, Frudd K, Hannah R, Shah AV, et al. The transcription factor ERG regulates super-enhancers associated with an endothelial-specific gene expression program. Circ. Res. 2019;124(9):1337-49.

88. Wagner JUG, Tombor LS, Malacarne PF, Kettenhausen LM, Panthel J, Kujundzic H, et al. Aging impairs the neurovascular interface in the heart. Science. 2023;381(6660):897-906.

89. Bassat E, Mutlak YE, Genzelinakh A, Shadrin IY, Baruch Umansky K, Yifa O, et al. The extracellular matrix protein agrin promotes heart regeneration in mice. Nature. 2017;547(7662):179-84.

90. Baehr A, Umansky KB, Bassat E, Jurisch V, Klett K, Bozoglu T, et al. Agrin promotes coordinated therapeutic processes leading to improved cardiac repair in pigs. Circulation. 2020;142(9):868-81.

91. Ali SR, Elhelaly W, Nguyen NUN, Li S, Menendez-Montes I, Wang Z, et al. Angiocrine IGFBP3 spatially coordinates IGF signaling during neonatal cardiac regeneration. bioRxiv. 2021:2021.09.16.460522.

92. Wei K, Serpooshan V, Hurtado C, Diez-Cuñado M, Zhao M, Maruyama S, et al. Epicardial FSTL1 reconstitution regenerates the adult mammalian heart. Nature. 2015;525(7570):479-85.

93. Jiang H, Zhang L, Liu X, Sun W, Kato K, Chen C, et al. Angiocrine FSTL1 (Follistatin-Like Protein 1) insufficiency leads to atrial and venous wall fibrosis via SMAD3 activation. Arterioscler. Thromb. Vasc. Biol. 2020;40(4):958-72.

94. Kühn B, del Monte F, Hajjar RJ, Chang YS, Lebeche D, Arab S, et al. Periostin induces proliferation of differentiated cardiomyocytes and promotes cardiac repair. Nat. Med. 2007;13(8):962-9.

95. Taniyama Y, Katsuragi N, Sanada F, Azuma J, Iekushi K, Koibuchi N, et al. Selective blockade of periostin exon 17 preserves cardiac performance in acute myocardial infarction. Hypertension. 2016;67(2):356-61.

96. Hu J, Srivastava K, Wieland M, Runge A, Mogler C, Besemfelder E, et al. Endothelial cell-derived angiopoietin-2 controls liver regeneration as a spatiotemporal rheostat. Science. 2014;343(6169):416-9.

97. Ben-Moshe S, Shapira Y, Moor AE, Manco R, Veg T, Bahar Halpern K, et al. Spatial sorting enables comprehensive characterization of liver zonation. Nat. Metabol. 2019;1(9):899-911.

98. Halpern KB, Shenhav R, Massalha H, Toth B, Egozi A, Massasa EE, et al. Paired-cell sequencing enables spatial gene expression mapping of liver endothelial cells. Nat. Biotechnol. 2018;36(10):962-70.

99. Koch PS, Olsavszky V, Ulbrich F, Sticht C, Demory A, Leibing T, et al. Angiocrine Bmp2 signaling in murine liver controls normal iron homeostasis. Blood. 2017;129(4):415-9.

100. Rocha Ana S, Vidal V, Mertz M, Kendall Timothy J, Charlet A, Okamoto H, et al. The Angiocrine Factor Rspondin3 Is a Key Determinant of Liver Zonation. Cell Rep. 2015;13(9):1757-64.

101. Leibing T, Géraud C, Augustin I, Boutros M, Augustin HG, Okun JG, et al. Angiocrine Wnt signaling controls liver growth and metabolic maturation in mice. Hepatology. 2018;68(2):707-22.

102. Lorenz L, Axnick J, Buschmann T, Henning C, Urner S, Fang S, et al. Mechanosensing by β1 integrin induces angiocrine signals for liver growth and survival. Nature. 2018;562(7725):128-32.

103. Ding B-S, Nolan DJ, Butler JM, James D, Babazadeh AO, Rosenwaks Z, et al. Inductive angiocrine signals from sinusoidal endothelium are required for liver regeneration. Nature. 2010;468(7321):310-5.

104. Gomez-Salinero JM, Itkin T, Rafii S. Developmental angiocrine diversification of endothelial cells for organotypic regeneration. Dev. Cell. 2021;56(22):3042-51.

105. Inverso D, Shi J, Lee KH, Jakab M, Ben-Moshe S, Kulkarni SR, et al. A spatial vascular transcriptomic, proteomic, and phosphoproteomic atlas unveils an angiocrine Tie-Wnt signaling axis in the liver. Dev. Cell. 2021;56(11):1677-93.e10.

106. Ben-Moshe S, Veg T, Manco R, Dan S, Papinutti D, Lifshitz A, et al. The spatiotemporal program of zonal liver regeneration following acute injury. Cell Stem Cell. 2022;29(6):973-89.e10.

107. Géraud C, Koch PS, Zierow J, Klapproth K, Busch K, Olsavszky V, et al. GATA4-dependent organ-specific endothelial differentiation controls liver development and embryonic hematopoiesis. J Clin. Invest. 2017;127(3):1099-114.

108. Winkler M, Staniczek T, Kürschner SW, Schmid CD, Schönhaber H, Cordero J, et al. Endothelial GATA4 controls liver fibrosis and regeneration by preventing a pathogenic switch in angiocrine signaling. J. Hepatol. 2021;74(2):380-93.

109. Duan J-L, Liu J-J, Ruan B, Ding J, Fang Z-Q, Xu H, et al. Age-related liver endothelial zonation triggers steatohepatitis by inactivating pericentral endothelium-derived C-kit. Nat. Aging. 2023;3(3):258-74.

110. Gillich A, Zhang F, Farmer CG, Travaglini KJ, Tan SY, Gu M, et al. Capillary cell-type specialization in the alveolus. Nature. 2020;586(7831):785-9.

111. Niethamer TK, Stabler CT, Leach JP, Zepp JA, Morley MP, Babu A, et al. Defining the role of pulmonary endothelial cell heterogeneity in the response to acute lung injury. eLife. 2020;9:e53072.

112. Zhou B, Magana L, Hong Z, Huang LS, Chakraborty S, Tsukasaki Y, et al. The angiocrine Rspondin3 instructs interstitial macrophage transition via metabolic–epigenetic reprogramming and resolves inflammatory injury. Nat. Immunol. 2020;21(11):1430-43.

113. Ding B-S, Nolan Daniel J, Guo P, Babazadeh Alexander O, Cao Z, Rosenwaks Z, et al. Endothelial-derived angiocrine signals induce and sustain regenerative lung alveolarization. Cell. 2011;147(3):539-53.

114. Cao Z, Lis R, Ginsberg M, Chavez D, Shido K, Rabbany SY, et al. Targeting of the pulmonary capillary vascular niche promotes lung alveolar repair and ameliorates fibrosis. Nat. Med. 2016;22(2):154-62.

115. Rafii S, Cao Z, Lis R, Siempos II, Chavez D, Shido K, et al. Platelet-derived SDF-1 primes the pulmonary capillary vascular niche to drive lung alveolar regeneration. Nat. Cell Biol. 2015;17(2):123-36.

116. Volpe MC, Ciucci G, Zandomenego G, Vuerich R, Ring NAR, Vodret S, et al. Flt1 produced by lung endothelial cells impairs ATII cell transdifferentiation and repair in pulmonary fibrosis. Cell Death & Dis. 2023;14(7):437.

117. Alsina-Sanchis E, Mülfarth R, Fischer A. Control of Tumor Progression by Angiocrine Factors. Cancers. 2021;13(11).

118. Preuss SF, Grieshober D, Augustin HG. Systemic reprogramming of endothelial cell signaling in metastasis and cachexia. Physiology. 2023;38(4):189-202.

119. Butler JM, Kobayashi H, Rafii S. Instructive role of the vascular niche in promoting tumour growth and tissue repair by angiocrine factors. Nat. Rev. Cancer. 2010;10(2):138-46.

120. Singh A, Veeriah V, Xi P, Labella R, Chen J, Romeo SG, et al. Angiocrine signals regulate quiescence and therapy resistance in bone metastasis. JCI insight. 2019;4(13).

121. Singhal M, Gengenbacher N, Abdul Pari AA, Kamiyama M, Hai L, Kuhn BJ, et al. Temporal multi-omics identifies LRG1 as a vascular niche instructor of metastasis. Sci. Transl. Med. 2021;13(609):eabe6805.

122. Hübers C, Abdul Pari AA, Grieshober D, Petkov M, Schmidt A, Messmer T, et al. Primary tumor–derived systemic nANGPTL4 inhibits metastasis. J Exp. Med. 2022;220(1).

123. Todaro GJ, Huebner RJ. The viral oncogene hypothesis: new evidence. 1972;69(4):1009-15.

124. Holley RW. A unifying hypothesis concerning the nature of malignant growth. PNAS. 1972;69(10):2840-1.

125. Todaro GJ, De Larco JE, Cohen S. Transformation by murine and feline sarcoma viruses specifically blocks binding of epidermal growth factor to cells. Nature. 1976;264(5581):26-31.

126. Sporn MB, Todaro GJ. Autocrine secretion and malignant transformation of cells. N. Engl. J. Med. 1980;303(15):878-80.

127. Holley RW. Control of growth of mammalian cells in cell culture. Nature. 1975;258(5535):487-90.

128. de Larco JE, Todaro GJ. Growth factors from murine sarcoma virus-transformed cells. Proc. Natl. Acad. Sci. 1978;75(8):4001-5.

129. Todaro GJ, Fryling C, De Larco JE. Transforming growth factors produced by certain human tumor cells: polypeptides that interact with epidermal growth factor receptors. Proc. Natl. Acad. Sci. 1980;77(9):5258-62.

130. Roberts AB, Anzano MA, Lamb LC, Smith JM, Sporn MB. New class of transforming growth factors potentiated by epidermal growth factor: isolation from non-neoplastic tissues. PNAS. 1981;78(9):5339-43.

131. Wu MY, Hill CS. TGF-β superfamily signaling in embryonic development and homeostasis. Dev. Cell. 2009;16(3):329-43.

132. Chen P-Y, Qin L, Simons M. TGFβ signaling pathways in human health and disease. Front. Mol. Biosci. 2023;10.

133. Heldin CH, Moustakas A. Signaling receptors for TGF-β family members. Cold Spring Harb. Perspect. Biol. 2016;8(8).

134. ten Dijke P, Goumans MJ, Pardali E. Endoglin in angiogenesis and vascular diseases. Angiogenesis. 2008;11(1):79-89.

135. Bilandzic M, Stenvers KL. Betaglycan: a multifunctional accessory. Mol. Cell. Endocrinol. 2011;339(1-2):180-9.

136. Moses HL, Roberts AB, Derynck R. The discovery and early days of TGF-β: A historical perspective. Cold Spring Harb. Perspect. Biol. 2016;8(7).

137. Massagué J. TGFβ signalling in context. Nat Rev. Mol. Cell Biol. 2012;13(10):616-30.

138. Senn on the healing of aseptic bone cavities by implantation of antiseptic decalcified bone. Ann. Surg. 1889;10(5):352-68.

139. Urist MR. Bone: formation by autoinduction. Science. 1965;150(3698):893-9.

140. Katagiri T, Watabe T. Bone morphogenetic proteins. Cold Spring Harb. Perspect. Biol. 2016;8(6).

141. Goumans MJ, Zwijsen A, Ten Dijke P, Bailly S. Bone morphogenetic proteins in vascular homeostasis and disease. Cold Spring Harb. Perspect. Biol. 2018;10(2).

142. Lowery JW, Rosen V. Bone morphogenetic protein-based therapeutic approaches. Cold Spring Harb. Perspect. Biol. 2018;10(4).

143. Aykul S, Martinez-Hackert E. Transforming growth factor-β family ligands can function as antagonists by competing for type II receptor binding. J. Biol. Chem. 2016;291(20):10792-804.

144. Klumpe HE, Langley MA, Linton JM, Su CJ, Antebi YE, Elowitz MB. The context-dependent, combinatorial logic of BMP signaling. Cell Syst. 2022;13(5):388-407.e10.

145. Ross S, Hill CS. How the Smads regulate transcription. Int. J. Biochem. Cell Biol. 2008;40(3):383-408.

146. Massagué J, Seoane J, Wotton D. Smad transcription factors. Genes Dev. 2005;19(23):2783-810.

147. Lucarelli P, Schilling M, Kreutz C, Vlasov A, Boehm ME, Iwamoto N, et al. Resolving the combinatorial complexity of smad protein complex formation and its link to gene expression. Cell Syst. 2018;6(1):75-89.e11.

148. Hanyu A, Ishidou Y, Ebisawa T, Shimanuki T, Imamura T, Miyazono K. The N domain of Smad7 is essential for specific inhibition of transforming growth factor-beta signaling. J Cell Biol. 2001;155(6):1017-27.

149. Mochizuki T, Miyazaki H, Hara T, Furuya T, Imamura T, Watabe T, et al. Roles for the MH2 domain of Smad7 in the specific inhibition of transforming growth factor-beta superfamily signaling. J. Biol. Chem. 2004;279(30):31568-74.

150. Yan X, Liao H, Cheng M, Shi X, Lin X, Feng XH, et al. Smad7 protein interacts with receptor-regulated Smads (R-Smads) to inhibit transforming growth factor-β (TGF-β)/Smad signaling. J. Biol. Chem. 2016;291(1):382-92.

151. Miyazawa K, Miyazono K. Regulation of TGF-β family signaling by inhibitory Smads. Cold Spring Harb. Perspect. Biol. 2017;9(3).

152. Topper JN, Cai J, Qiu Y, Anderson KR, Xu YY, Deeds JD, et al. Vascular MADs: two novel MAD-related genes selectively inducible by flow in human vascular endothelium. Proc. Natl. Acad. Sci. 1997;94(17):9314-9.

153. Fu W, Huo R, Yan Z, Xu H, Li H, Jiao Y, et al. Mesenchymal behavior of the endothelium promoted by SMAD6 downregulation is associated with brain arteriovenous malformation microhemorrhage. Stroke. 2020;51(7):2197-207.

154. Chen Q, Chen H, Zheng D, Kuang C, Fang H, Zou B, et al. Smad7 is required for the development and function of the heart. J. Biol. Chem. 2009;284(1):292-300.

155. Vargesson N, Laufer E. Smad7 misexpression during embryonic angiogenesis causes vascular dilation and malformations independently of vascular smooth muscle cell function. Dev. Biol. 2001;240(2):499-516.

156. Chen PY, Qin L, Li G, Wang Z, Dahlman JE, Malagon-Lopez J, et al. Endothelial TGF-β signalling drives vascular inflammation and atherosclerosis. Nat. Metab. 2019;1(9):912-26.

157. De Rossi G, Da Vitoria Lobo ME, Greenwood J, Moss SE. LRG1 as a novel therapeutic target in eye disease. Eye. 2022;36(2):328-40.

158. Kim LA, D'Amore PA. A brief history of anti-VEGF for the treatment of ocular angiogenesis. Am. J. Pathol. 2012;181(2):376-9.

159. Mukwaya A, Jensen L, Lagali N. Relapse of pathological angiogenesis: functional role of the basement membrane and potential treatment strategies. Exp. Mol. Med. 2021;53(2):189-201.

160. Holderfield MT, Hughes CCW. Crosstalk between vascular endothelial growth factor, notch, and transforming growth factor-β in vascular morphogenesis. Circ. Res. 2008;102(6):637-52.

161. Hultgren NW, Fang JS, Ziegler ME, Ramirez RN, Phan DTT, Hatch MMS, et al. Slug regulates the Dll4-Notch-VEGFR2 axis to control endothelial cell activation and angiogenesis. Nat. Commun. 2020;11(1):5400.

162. Pulkkinen HH, Kiema M, Lappalainen JP, Toropainen A, Beter M, Tirronen A, et al. BMP6/TAZ-Hippo signaling modulates angiogenesis and endothelial cell response to VEGF. Angiogenesis. 2021;24(1):129-44.

163. Kallenberg D, Tripathi V, Javaid F, Pilotti C, George J, Davis S, et al. A Humanized Antibody against LRG1 that inhibits angiogenesis and reduces retinal vascular leakage. bioarxiv. 2021:2020.07.25.218149.

164. Evans JD, Girerd B, Montani D, Wang XJ, Galiè N, Austin ED, et al. BMPR2 mutations and survival in pulmonary arterial hypertension: an individual participant data meta-analysis. Lancet Respir. Med. 2016;4(2):129-37.

Bibliography

165. Gräf S, Haimel M, Bleda M, Hadinnapola C, Southgate L, Li W, et al. Identification of rare sequence variation underlying heritable pulmonary arterial hypertension. Nat. Commun. 2018;9(1):1416.

166. Sharmin N, Nganwuchu CC, Nasim MT. Targeting the TGF-β signaling pathway for resolution of pulmonary arterial hypertension. Trends in Pharmacological Sciences. 2021;42(7):510-3.

167. Desroches-Castan A, Tillet E, Bouvard C, Bailly S. BMP9 and BMP10: Two close vascular quiescence partners that stand out. Dev. Dyn. 2022;251(1):158-77.

168. Long L, Ormiston ML, Yang X, Southwood M, Gräf S, Machado RD, et al. Selective enhancement of endothelial BMPR-II with BMP9 reverses pulmonary arterial hypertension. Nat. Med. 2015;21(7):777-85.

169. Wits M, Becher C, de Man F, Sanchez-Duffhues G, Goumans M-J. Sex-biased TGFβ signaling in pulmonary arterial hypertension. Cardiovasc. Res. 2023.

170. Rendu MJBMSMHP. Epistaxis repetes chez unsujet porteur de petits angiomies cutaneset muqueux. Bull. Soc. Med. Hosp. 1886;13:731-3.

171. Babington BJL. Hereditary hemorrhagic telangiectasia. Lancet. 1865;2:362-3.

172. Shovlin CL, Guttmacher AE, Buscarini E, Faughnan ME, Hyland RH, Westermann CJ, et al. Diagnostic criteria for hereditary hemorrhagic telangiectasia (Rendu-Osler-Weber syndrome). Am. J. Med. Genet. 2000;91(1):66-7.

173. Cole SG, Begbie ME, Wallace GM, Shovlin CL. A new locus for hereditary haemorrhagic telangiectasia (HHT3) maps to chromosome 5. J. Med. Genet. 2005;42(7):577-82.

174. Bayrak-Toydemir P, McDonald J, Akarsu N, Toydemir RM, Calderon F, Tuncali T, et al. A fourth locus for hereditary hemorrhagic telangiectasia maps to chromosome 7. Am. J. Med. Genet. 2006;140(20):2155-62.

175. Cerdà P, Castillo SD, Aguilera C, Iriarte A, Rocamora JL, Larrinaga AM, et al. New genetic drivers in hemorrhagic hereditary telangiectasia. Eur. J. Intern. Med. 2023.

176. McDonald J, Bayrak-Toydemir P, DeMille D, Wooderchak-Donahue W, Whitehead K. Curaçao diagnostic criteria for hereditary hemorrhagic telangiectasia is highly predictive of a pathogenic variant in ENG or ACVRL1 (HHT1 and HHT2). Genet. Med. 2020;22(7):1201-5.

177. Choi H, Kim B-G, Kim YH, Lee S-J, Lee YJ, Oh SP. BMP10 functions independently from BMP9 for the development of a proper arteriovenous network. Angiogenesis. 2023;26(1):167-86.

178. Kleiter I, Song J, Lukas D, Hasan M, Neumann B, Croxford AL, et al. Smad7 in T cells drives T helper 1 responses in multiple sclerosis and experimental autoimmune encephalomyelitis. Brain. 2010;133(Pt 4):1067-81.

179. Sörensen I, Adams RH, Gossler A. DLL1-mediated Notch activation regulates endothelial identity in mouse fetal arteries. Blood. 2009;113(22):5680-8.

180. Wylie LA, Mouillesseaux KP, Chong DC, Bautch VL. Developmental SMAD6 loss leads to blood vessel hemorrhage and disrupted endothelial cell junctions. Dev. Biol. 2018;442(2):199-209.

181. Goumans MJ, Ten Dijke P. TGF-β Signaling in Control of Cardiovascular Function. Cold Spring Harb. Perspect. Biol. 2018;10(2).

182. Brash JT, Ruhrberg C, Fantin A. Evaluating vascular hyperpermeability-inducing agents in the skin with the miles assay. Journal of visualized experiments : JoVE. 2018(136).

183. Padua D, Massagué J. Roles of TGFβ in metastasis. Cell Research. 2009;19(1):89-102.

184. Massagué J. TGFbeta in Cancer. Cell. 2008;134(2):215-30.

185. Cunha SI, Magnusson PU, Dejana E, Lampugnani MG. Deregulated TGF-β/BMP signaling in vascular malformations. Circ. Res. 2017;121(8):981-99.

186. Suzuki A, Kaneko E, Maeda J, Ueno N. Mesoderm induction by BMP-4 and -7 heterodimers. Biochem. Biophys. Res. Commun. 1997;232(1):153-6.

187. Goumans M-J, Liu Z, ten Dijke P. TGF-β signaling in vascular biology and dysfunction. Cell Res. 2009;19(1):116-27.

188. ten Dijke P, Arthur HM. Extracellular control of TGFβ signalling in vascular development and disease. Nat. Rev. Mol. Cell Biol. 2007;8(11):857-69.

Bibliography

189. Luukko K, Ylikorkala A, Mäkelä TP. Developmentally regulated expression of Smad3, Smad4, Smad6, and Smad7 involved in TGF-beta signaling. Mech. Dev. 2001;101(1):209-12.

190. Larsson J, Goumans MJ, Sjöstrand LJ, van Rooijen MA, Ward D, Levéen P, et al. Abnormal angiogenesis but intact hematopoietic potential in TGF-beta type I receptor-deficient mice. EMBO J. 2001;20(7):1663-73.

191. Hayashi H, Abdollah S, Qiu Y, Cai J, Xu YY, Grinnell BW, et al. The MAD-related protein Smad7 associates with the TGFbeta receptor and functions as an antagonist of TGFbeta signaling. Cell. 1997;89(7):1165-73.

192. Hata A, Lagna G, Massagué J, Hemmati-Brivanlou A. Smad6 inhibits BMP/Smad1 signaling by specifically competing with the Smad4 tumor suppressor. Gene Dev. 1998;12(2):186-97.

193. Ferrari G, Cook BD, Terushkin V, Pintucci G, Mignatti P. Transforming growth factor-beta 1 (TGF-beta1) induces angiogenesis through vascular endothelial growth factor (VEGF)-mediated apoptosis. J Cell Physiol. 2009;219(2):449-58.

194. Lowery JW, de Caestecker MP. BMP signaling in vascular development and disease. Cytokine Growth Factor Rev. 2010;21(4):287-98.

195. Danesh SM, Villasenor A, Chong D, Soukup C, Cleaver O. BMP and BMP receptor expression during murine organogenesis. Gene Expr. Patterns. 2009;9(5):255-65.

196. Xu J, Lamouille S, Derynck R. TGF-beta-induced epithelial to mesenchymal transition. Cell. Res. 2009;19(2):156-72.

197. Paola AG, Joseph HM. TGF-β Activation and signaling in angiogenesis. Physiologic and Pathologic Angiogenesis. IntechOpen; 2017.

198. Langenfeld EM, Langenfeld J. Bone morphogenetic protein-2 stimulates angiogenesis in developing tumors. Mol. Cancer Res. 2004;2(3):141-9.

199. Pi X, Ren R, Kelley R, Zhang C, Moser M, Bohil AB, et al. Sequential roles for myosin-X in BMP6-dependent filopodial extension, migration, and activation of BMP receptors. J Cell Biol. 2007;179(7):1569-82.

200. Wakayama Y, Fukuhara S, Ando K, Matsuda M, Mochizuki N. Cdc42 mediates bmp-induced sprouting angiogenesis through Fmnl3-driven assembly of endothelial filopodia in zebrafish. Dev. Cell. 2015;32(1):109-22.

201. Wiley DM, Kim J-D, Hao J, Hong CC, Bautch VL, Jin S-W. Distinct signalling pathways regulate sprouting angiogenesis from the dorsal aorta and the axial vein. Nat. Cell Biol. 2011;13(6):686-92.

202. Ntumba K, Akla N, Oh SP, Eichmann A, Larrivée B. BMP9/ALK1 inhibits neovascularization in mouse models of age-related macular degeneration. Oncotarget. 2016;7(35):55957-69.

203. Lee HW, Chong DC, Ola R, Dunworth WP, Meadows S, Ka J, et al. Alk2/ACVR1 and Alk3/BMPR1A provide essential function for bone morphogenetic protein-induced retinal angiogenesis. Arterioscler. Thromb. Vasc. Biol. 2017;37(4):657-63.

204. Johnson DW, Berg JN, Baldwin MA, Gallione CJ, Marondel I, Yoon SJ, et al. Mutations in the activin receptor-like kinase 1 gene in hereditary haemorrhagic telangiectasia type 2. Nat Genet. 1996;13(2):189-95.

205. Schmid CD, Olsavszky V, Reinhart M, Weyer V, Trogisch FA, Sticht C, et al. ALK1 controls hepatic vessel formation, angiodiversity, and angiocrine functions in hereditary hemorrhagic telangiectasia of the liver. Hepatology. 2023;77(4):1211-27.

206. Ferrari G, Pintucci G, Seghezzi G, Hyman K, Galloway AC, Mignatti P. VEGF, a prosurvival f actor, acts in concert with TGF-beta1 to induce endothelial cell apoptosis. Proc. Natl. Acad. Sci. 2006;103(46):17260-5.

207. Kim KS, Park JM, Kong T, Kim C, Bae SH, Kim HW, et al. Retinal angiogenesis effects of TGF-β1 and paracrine factors secreted from human placental stem cells in response to a pathological environment. Cell Transplant. 2016;25(6):1145-57.

208. Seoane J, Gomis RR. TGF-β family signaling in tumor suppression and cancer progression. Cold Spring Harb. Perspect. Biol. 2017;9(12).

Bibliography

209. Bach D-H, Park HJ, Lee SKJMT-O. The dual role of bone morphogenetic proteins in cancer. Mol. Ther. Oncolytics 2018;8:1-13.

210. Prunier C, Baker D, ten Dijke P, Ritsma L. TGF-β family signaling pathways in cellular dormancy. Trends Cancer. 2019;5(1):66-78.

211. Bragado P, Estrada Y, Parikh F, Krause S, Capobianco C, Farina HG, et al. TGF-β2 dictates disseminated tumour cell fate in target organs through TGF-β-RIII and p38α/β signalling. Nat. Cell Biol. 2013;15(11):1351-61.

212. Yumoto K, Eber MR, Wang J, Cackowski FC, Decker AM, Lee E, et al. Axl is required for TGF-β2-induced dormancy of prostate cancer cells in the bone marrow. Sci. Rep. 2016;6(1):36520.

213. Yu-Lee L-Y, Yu G, Lee Y-C, Lin S-C, Pan J, Pan T, et al. Osteoblast-secreted factors mediate dormancy of metastatic prostate cancer in the bone via activation of the TGFβRIII–p38MAPK–pS249/T252RB pathway. Cancer Res. 2018;78(11):2911-24.

214. Ghajar CM, Peinado H, Mori H, Matei IR, Evason KJ, Brazier H, et al. The perivascular niche regulates breast tumour dormancy. Nat. Cell Biol. 2013;15(7):807-17.

215. Langenfeld EM, Langenfeld J. Bone morphogenetic protein-2 stimulates angiogenesis in developing tumors. Mol. Cancer Res. : MCR. 2004;2(3):141-9.

216. Kam CY, Singh ID, Gonzalez DG, Matte-Martone C, Solá P, Solanas G, et al. Mechanisms of skin vascular maturation and maintenance captured by longitudinal imaging of live mice. Cell. 2023;186(11):2345-60.e16.

217. Coelho-Santos V, Berthiaume A-A, Ornelas S, Stuhlmann H, Shih AY. Imaging the construction of capillary networks in the neonatal mouse brain. Proc. Natl. Acad. Sci. 2021;118(26):e2100866118.

218. Ehling M, Adams S, Benedito R, Adams RH. Notch controls retinal blood vessel maturation and quiescence. Development. 2013;140(14):3051-61.

219. Kulikauskas MR, Oatley M, Yu T, Liu Z, Matsumura L, Kidder E, et al. Endothelial cell SMAD6 balances ACVRL1/Alk1 function to regulate adherens junctions and hepatic vascular development. Development. 2023.

220. Ma Z, Mao C, Jia Y, Fu Y, Kong W. Extracellular matrix dynamics in vascular remodeling. Am. J. Physiol. Cell Physiol. 2020;319(3):C481-C99.

221. Davis GE, Senger DR. Endothelial Extracellular Matrix. Circ. Res. 2005;97(11):1093-107.

222. Fernández-Chacón M, Mühleder S, Regano A, Garcia-Ortega L, Rocha SF, Torroja C, et al. Incongruence between transcriptional and vascular pathophysiological cell states. Nat. Cardiovasc. Res. 2023;2(6):530-49.

223. Gengenbacher N, Singhal M, Mogler C, Hai L, Milde L, Pari AAA, et al. Timed Ang2-targeted therapy identifies the angiopoietin-tie pathway as key regulator of fatal lymphogenous metastasis. Cancer Discov. 2021;11(2):424-45.

224. Gengenbacher N, Singhal M, Augustin HG. Preclinical mouse solid tumour models: status quo, challenges and perspectives. Nat. Rev. Cancer. 2017;17(12):751-65.

225. Mohanty S, Xu L. Experimental metastasis assay. JoVE. 2010(42).

226. Park S-Y, Nam J-S. The force awakens: metastatic dormant cancer cells. Exp. Mol. Med. 2020;52(4):569-81.

227. Indraccolo S, Minuzzo S, Masiero M, Pusceddu I, Persano L, Moserle L, et al. Cross-talk between tumor and endothelial cells involving the Notch3-Dll4 interaction marks escape from tumor dormancy. Cancer Res. 2009;69(4):1314-23.

228. Gao H, Chakraborty G, Lee-Lim Ai P, Mo Q, Decker M, Vonica A, et al. The BMP inhibitor Coco reactivates breast cancer cells at lung metastatic sites. Cell. 2012;150(4):764-79.

229. Kobayashi A, Okuda H, Xing F, Pandey PR, Watabe M, Hirota S, et al. Bone morphogenetic protein 7 in dormancy and metastasis of prostate cancer stem-like cells in bone. J. Exp. Med. 2011;208(13):2641-55.

230. Pitulescu ME, Schmidt I, Benedito R, Adams RH. Inducible gene targeting in the neonatal vasculature and analysis of retinal angiogenesis in mice. Nat. Protoc. 2010;5(9):1518-34.

231. Livak KJ, Schmittgen TD. Analysis of relative gene expression data using real-time quantitative PCR and the 2(-Delta Delta C(T)) Method. Methods. 2001;25(4):402-8.

232. Hughes CS, Moggridge S, Müller T, Sorensen PH, Morin GB, Krijgsveld J. Single-pot, solid-phase-enhanced sample preparation for proteomics experiments. Nat. Protoc. 2019;14(1):68-85.

233. Gierlinski M, Gastaldello F, Cole C, Cole C, Barton G. Proteus : an R package for downstream analysis of MaxQuant output. bioRxiv; 2018.

234. Ritchie ME, Phipson B, Wu D, Hu Y, Law CW, Shi W, et al. limma powers differential expression analyses for RNA-sequencing and microarray studies. Nucleic Acids Res. 2015;43(7):e47.

235. Kim HJ, Kim T, Xiao D, Yang P. Protocol for the processing and downstream analysis of phosphoproteomic data with PhosR. STAR protocols. 2021;2(2):100585.

236. Tyanova S, Temu T, Sinitcyn P, Carlson A, Hein MY, Geiger T, et al. The Perseus computational platform for comprehensive analysis of (prote)omics data. Nat. Methods. 2016;13(9):731-40.

237. Ewels P, Magnusson M, Lundin S, Käller M. MultiQC: summarize analysis results for multiple tools and samples in a single report. Bioinformatics. 2016;32(19):3047-8.

238. Dobin A, Davis CA, Schlesinger F, Drenkow J, Zaleski C, Jha S, et al. STAR: ultrafast universal RNA-seq aligner. Bioinformatics. 2012;29(1):15-21.

239. Putri GH, Anders S, Pyl PT, Pimanda JE, Zanini F. Analysing high-throughput sequencing data in Python with HTSeq 2.0. Bioinformatics. 2022;38(10):2943-5.

240. Love MI, Huber W, Anders S. Moderated estimation of fold change and dispersion for RNA-seq data with DESeq2. Genome Biol. 2014;15(12):550.

241. Wu T, Hu E, Xu S, Chen M, Guo P, Dai Z, et al. clusterProfiler 4.0: A universal enrichment tool for interpreting omics data. Innovation 2021;2(3):100141.

242. Berg S, Kutra D, Kroeger T, Straehle CN, Kausler BX, Haubold C, et al. ilastik: interactive machine learning for (bio)image analysis. Nat. Methods. 2019;16(12):1226-32.

243. Rueden CT, Schindelin J, Hiner MC, DeZonia BE, Walter AE, Arena ET, et al. ImageJ2: ImageJ for the next generation of scientific image data. BMC Bioinformatics. 2017;18(1):529.